Universidad de Málaga

Escuela Técnica Superior de Ingeniería de Telecomunicación

TESIS DOCTORAL

Photonic Chip Interconnects and Integrated Polarization Management for Coherent Communication

Autor:

Carlos A. Alonso Ramos

Directores:

Alejandro Ortega Moñux
Íñigo Molina Fernández

AUTOR: Carlos Alberto Alonso Ramos

EDITA: Publicaciones y Divulgación Científica. Universidad de Málaga

ingeniería de
comunicaciones

Dr.D. Alejandro Ortega Moñux y **Dr.D. Íñigo Molina Fernández**, profesores doctores del Departamento de Ingeniería de Comunicaciones de la Universidad de Málaga

CERTIFICAN:

Que D. Carlos A. Alonso Ramos, Ingeniero de Telecomunicación, ha realizado en el Departamento de Ingeniería de Comunicaciones de la Universidad de Málaga bajo su dirección, el trabajo de investigación correspondiente a su TESIS DOCTORAL titulada:

Photonic Chip Interconnects and Integrated Polarization Management for Coherent Communication

En dicho trabajo se han expuesto diversas aportaciones originales, entre las que cabe destacar el desarrollo de redes de difracción eficientes para el acoplo chip-fibra, el diseño de rotadores de polarización integrados de grandes tolarancias a errores de fabricación o el diseño de un receptor para comuniaciones coherentes basadas en multiplexación por polarización que no requiere de rotadores ni de separadores de polarizacion.

Por todo ello, consideran que esta Tesis es apta para su presentación al tribunal que ha de juzgarla. Y para que conste a efectos de lo establecido en el Real Decreto 1393/2007, regulador de los Estudios de Tercer Ciclo-Doctorado, AUTORIZAN la presentación de esta Tesis en la Universidad de Málaga

Málaga, a 5 de Mayo de 2014

Iñigo Molina

Fdo.: Dr.D. Alejandro Ortega Moñux

Fdo.: Íñigo Molina Fernández

UNIVERSIDAD DE MÁLAGA
ESCUELA TÉCNICA SUPERIOR DE INGENIERÍA DE TELECOMUNICACIÓN

Reunido el tribunal examinador en el día de la fecha, constituido por:

Presidente: Dr. D. ______________________________

Secretario: Dr. D. ______________________________

Vocales: Dr. D. ______________________________

Dr. D. ______________________________

Dr. D. ______________________________

para juzgar la Tesis Doctoral titulada **Photonic Chip Interconnects and Integrated Polarization Management for Coherent Communication** realizada por D. Carlos A. Alonso Ramos y dirigida por el Dr. D. Alejandro Ortega Moñux y el Dr. D. Íñigo Molina Fernández, acordó por

____

otorgar la calificación de

____

y para que conste, se extiende firmada por los componentes del tribunal la presente diligencia.

Málaga, a ______ de __________ de ______

El Presidente: El Secretario:

Fdo.: ____________________ Fdo.: ____________________

El Vocal: El Vocal: El Vocal:

Fdo.: ______________ Fdo.: ______________ Fdo.: ______________

Photonic Chip Interconnects and Integrated Polarization Management for Coherent Communication

Carlos A. Alonso Ramos

Contents

1

Introduction

A wide variety of devices are presented in this thesis, including grating couplers, polarization rotators and dual-polarization coherent receivers, that are the result of the collaboration between the Photonics & RF group at the Universidad de Málaga [1] and different research groups, such as National Research Council of Canada, Fraunhofer Heinrich-Hertz-Institut or Universtié Paris Sud. The aim of this chapter is giving an overview of these contributions before discussing them in detail in the following sections. A general view of the context where this work can be framed is presented in section 1.1. In 1.2, main contributions presented in this thesis are briefly reviewed. Organization of this manuscript is described in section 1.3. Finally some relevant characteristics of the technology platforms used to develop proposed designs are qualitatively discussed in section 1.4.

State of the art in the field related to the proposed designs can be found in the corresponding chapters. A special attention has been devoted to analyze the art of grating couplers, as they are the main focus of this thesis in terms of time and number of contributions.

1.1. General Framework

It was in 1969 when Stewart E. Miller first proposed the implementation of an integrated photonic chip. In his seminal paper, published in the Bell System Technical Journal [2], Miller discussed the use of planar dielectric strip waveguides, waveguide phase modulators, ring resonators, and Bragg reflectors as optical filters or cavity lasers, setting the basis for current photonics. The laser had been invented nine years before [3], and in 1962 several groups had already demonstrated lasing on semiconductors [4–7]. A bright future was envisioned at the time for the photonic integrated circuit, and an exponential growth similar to that of microelectronics was foreseen. In Miller own words *"If realized, this new art would facilitate isolating the laser circuit assembly from thermal, mechanical, and accustic ambient changes through small overall size; economy should ultimately result"* [2], but economy did not result, at least not as expected. The possible reasons for the slow development of photonics (compared to microelectronics) are reviewed by Ivan P. Kaminow, Miller's college in Bell Labs at the time, and include among others the fact that *"few applications that require both large-scale integration and high volume, with attendant low cost, have been identified"* [8].

Nowadays, bandwidth-hungry applications such as video streaming (youtube), social networking (facebook), or web search (google) relay on a large network of internet data centers, interconnected through optical links, to share huge amounts of information [9]. The ever-growing data rates and power consumption inside these data centers are pushing copper links close to their fundamental limits. Optical interconnects are expected to overcome these limitations, replacing electrical interconnects and becoming the preferred solution in the 1 meter to 10 km range [10]. For instance, active optoelectronic cables are successfully commercialized by the company Luxtera since 2006 [11], and in 2013 the Optical Internetworking Forum (OIF) released its new recommendation for next generation interconnect framework [12]. Besides, the increasing gap between the computational capacity and electrical bandwidth in high-performance computing systems is driving the development of rack-to-rack and even chip-to-chip optical links [13]. Silicon photonics [14–16], due to its compatibility with the CMOS platform, has been chosen by companies such as IBM [17], Intel [18] and Oracle [19] for the development of future generation photonic interconnects. Mid-infrared [20], biosensing [21] and microwave photonics [22, 23] applications are also demanding for high-performance and cost-effective integrated photonic devices. This huge potential market, with millions of parts per year, opens a second call for photonic exponential growth, but again *"economy should ultimately result"*.

In this envisioned mass production photonic platform, devices are processed using wafer-scale technology. Hence, in order to achieve desired cost-effectiveness, they need to be tested also at a wafer-scale, avoiding the need of the time consuming process of dicing and polishing every single device before testing it [11]. On the other hand, the insertion loss of the fiber-to-chip interface determines the reach and sensitivity of the link and thus its potential performance [24]. Moreover, next generation optical links need to provide connectivity for cables composed by tens or even hundreds of fibers [12]. Therefore grating couplers are considered a key building block of next generation integrated photonic library, as they enable wafer-scale testing with reduced insertion loss, and relaxed alignment tolerances [11, 24, 25]. However, due to the interferometric nature of grating couplers, they exhibit a limited operation bandwidth, and a strong polarization dependence, specially when compared with edge coupled solutions. Furthermore, efficiency of grating couplers is intrinsically limited by several factors, including reflections at refractive index discontinuities, mismatch between the radiated field and the optical fiber mode distribution, and power leakage to the substrate.

A particular attention has been dedicated to alleviate these limitations in the silicon-on-insulator (SOI) platform with sub-micrometer Si thickness (typically $220\,\mathrm{nm}$ - $300\,\mathrm{nm}$). Several alternatives have been proposed to minimize large back-reflections produced in SOI grating couplers that include, the use of a shallow etch step in the grating region [26–28], or sub-wavelength transition regions [29, 30]. A different approach consists on redirecting back-reflections out of the waveguide to avoid unwanted interference effects [31]. Mismatch between the optical fiber mode and the field radiated by the grating can be reduced by means of apodization. This can be done varying the duty cycle [28, 32, 33], the etch depth [34] or adding a sub-wavelength structure in the grating trenches [29, 30]. The most widely used solution to minimize loss due to substrate radiation is placing a mirror under the grating to re-direct up the power that has been radiated down by the coupler. This mirror can be implemented, for example, with a multilayer Bragg reflector [26, 35], or a thin metal layer [28, 36]. The use of the partial reflection produced in the BOX-to-substrate boundary has also been proposed to reduce substrate radiation loss [37, 38]. Intrinsic grating directionality in the upwards direction can be improved using customized etch depths in the grating region [39, 40] or high index thin overlays [31]. The use of sub-wavelength structures has also been proposed to provide polarization independent coupling [37]. Grating couplers with optimized etch depth combined with a bottom reflecting mirror have been demonstrated, that perform high efficiency coupling and polarization splitting functionalities [36]. A very interesting approach to handle polarization, is the 2-D grating grid used to couple both polarizations on chip, also providing polarization splitting and rotation [25, 41]. Sub-wavelength engineered gratings have been proposed that substantially increase coupling bandwidth [42].

The recent demonstration of Euler bends on micrometric silicon waveguides, that provide low loss with bending radii as small as $10\,\mu\mathrm{m}$ [43], paves a new path for unprecedented integration levels for this platform. This way, devices with similar footprint as those based on nano-wires can be developed that benefit from reduced polarization dependence and propagation loss of micrometric waveguides [44]. The main focus of this thesis has been developing high efficiency grating couplers for the micrometric silicon-on-insulator (SOI) platform.

Photonic integrated circuits have found wide acceptance in the long-haul fiber optic communication market. In this field, indium phosphide (InP) large-scale integrated photonic circuits, that provide data rates exceeding 100 Gb/s using several wavelength division multiplexed channels, are successfully commercialized by companies such as Infinera [45] or $\mathrm{U^2t}$ [46]. Next generation coherent polarization-multiplexed systems are expected to further increase bandwidth capacity, reaching rates of 100-400Gb/s per channel [47]. Integrated polarization rotators are a key element of these dual-polarization transceivers. Proposed integrated rotators can be divided between mode evolution based [48], cross-polarization coupling based [49, 50] and rotator waveguide based [51–58]. Some of these devices, require extra processing steps, that increase production cost, and increase the number of tolerances to control. Furthermore, all of these devices rely on very precise transversal geometries, and thus are very sensitive to slight deviations produced by fabrication errors. An important part of this thesis has been dedicated to propose solutions to alleviate these limitations.

As the component count raises, monolithic integration becomes increasingly appealing, as it offers a wide variety of advantages that include reduced weight, size, and power consumption, or improved reliability and potential performance [59]. Even so, commercial polarization-multiplexed receivers implement polarization management (composed by one or two polarization splitters) off-chip [60]. The main reason for that is the limited yield of integrated polarization splitters due to their stringent fabrication tolerances. The last part of this thesis is dedicated to develop an innovative solution to facilitate polarization handling in next generation monolithic dual-polarization coherent transceivers.

1.2. Overview of this Work

In this section, the main goals and contributions presented in this thesis (summarized in Fig. 1.1) are briefly outlined. Three are the main topics discussed in the following chapters: grating couplers, integrated polarization rotators, and integrated receivers for dual-polarization coherent receivers.

Grating Couplers

This part of the thesis has been developed in the frame of a collaboration between the Photonics & RF group at the Universidad de Málaga [1] and the National Research Council (NRC) Canada in Ottawa. The main goal was the implementation of efficient grating couplers for the micrometric SOI platform. Due to the larger waveguide thickness and minimum feature sizes of standard fabrication processes of the micron-scale platform, implementing grating couplers that have only one radiation beam is a challenging task. Multiple beams radiated by a grating coupler propagate with different angles, and can not be properly collected with a single-mode optical fiber, leading to low coupling efficiency devices. To overcome these limitations the use of an inverse taper as excitation stage and a higher order harmonic radiation have been proposed [61, 62], showing and remarkably large experimental coupling efficiency of $-2.2\,\mathrm{dB}$ for a uniform grating without bottom reflectors [63–66]. This design approach has been later used by companies such as Intel [67] and Oracle [68]. Proposed design has been further extended to provide polarization insensitive behavior [69, 70]. A grating-array-based input interface for an integrated spectrometer for spacial applications has been developed in collaboration with the NRC, the Canadian Space Agency and the company Comdev. The array, composed by several micrometric gratings, implements a $90\,\mu\mathrm{m}$ x $90\,\mu\mathrm{m}$ light collecting area, with a measured coupling efficiency of $-4.5\,\mathrm{dB}$ at $1354\,\mathrm{nm}$ wavelength (peak water absorption), that substantially improves system throughput, and thus potential spectrometer performance [71–73].

Integrated Polarization Rotators

The contributions in the field of integrated polarization rotators presented in this thesis can be divided in two branches: the collaboration with the Fraunhofer Heinrich-Hertz-Institut (HHI), developed in the frame of the european projects Celtic-Plus 100GET [74] and Mirthe [47], and the collaboration with the NRC and the Université Paris Sud.

In collaboration with the HHI a two steps waveguide geometry has been proposed to implement a rotator fully compatible with a previously developed InP monolithic 100GE downconverter. The two-steps geometry avoids the need of the wet etching step required for the fabrication of the widely used slanted rotators. Optimized device exhibits a calculated extinction ratio of $40\,\mathrm{dB}$ [75].

In collaboration with the NRC and Université Paris Sud, a novel integrated rotator scheme has been proposed that substantially increases device tolerance to fabrication errors resulting in a patent [76]. Three sections of rotator waveguide are connected through two tunable polarization phase-shifters. These tunable phase-shifters, that can be implemented for example with waveguide heaters, allow to compensate fabrication errors produced in the rotator sections [77, 78]. Furthermore, the proposed scheme, that

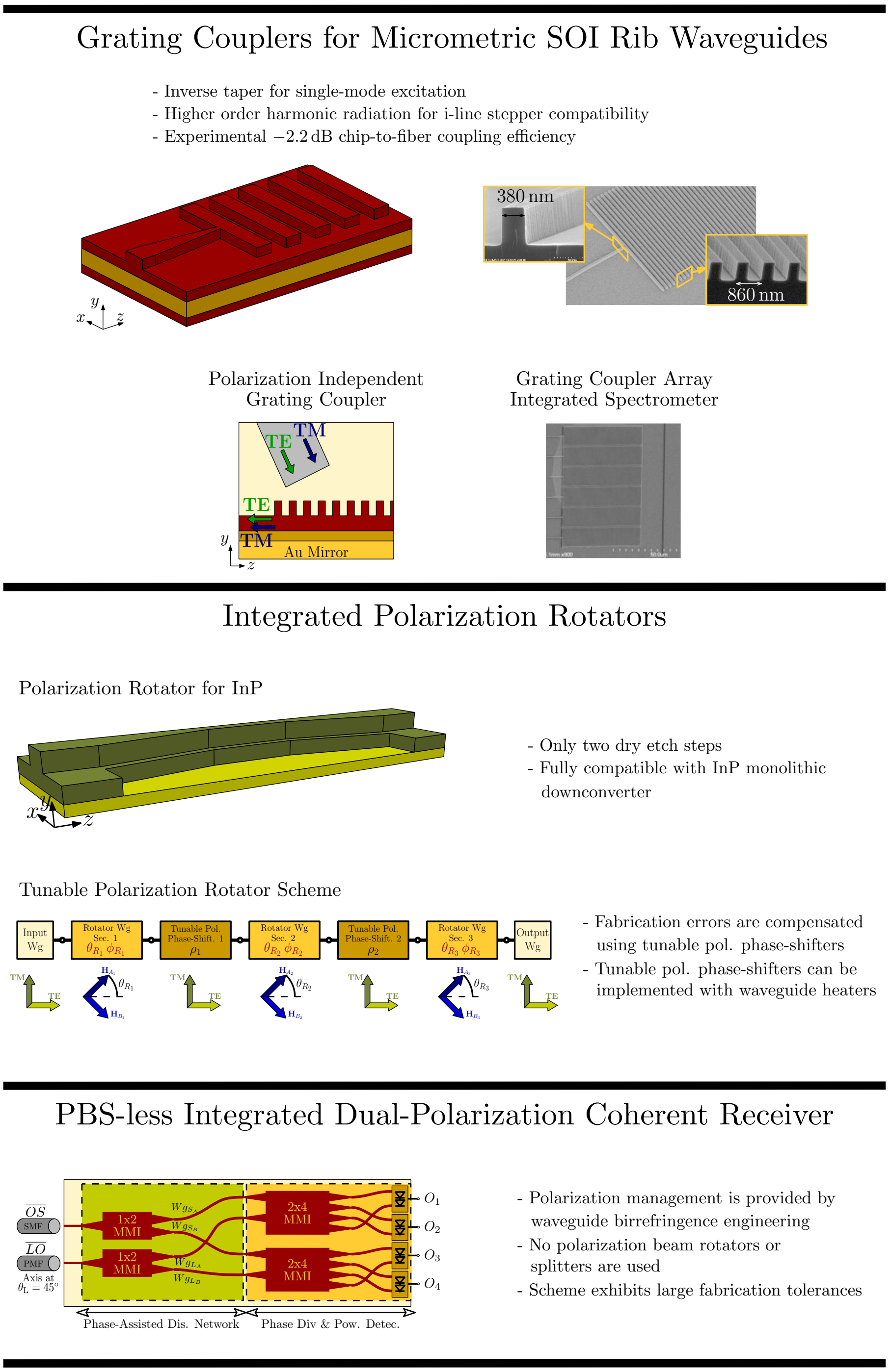

Grating Couplers for Micrometric SOI Rib Waveguides

- Inverse taper for single-mode excitation
- Higher order harmonic radiation for i-line stepper compatibility
- Experimental −2.2 dB chip-to-fiber coupling efficiency

Integrated Polarization Rotators

- Only two dry etch steps
- Fully compatible with InP monolithic downconverter

- Fabrication errors are compensated using tunable pol. phase-shifters
- Tunable pol. phase-shifters can be implemented with waveguide heaters

PBS-less Integrated Dual-Polarization Coherent Receiver

- Polarization management is provided by waveguide birrefringence engineering
- No polarization beam rotators or splitters are used
- Scheme exhibits large fabrication tolerances

Figure 1.1.: Overview of the main contributions presented in this thesis.

can be applied to any technology platform, allows to dynamically select central device wavelength.

Dual-Polarization Coherent Receivers

The Photonics & RF group at the Universidad de Málaga has been working on the development of integrated coherent receivers for single and dual-polarization communication systems inside several national, regional and european projects [1]. In this context, a novel architecture for integrated dual-polarization coherent receivers has been proposed that requires neither polarization beam splitters (PBS) nor polarization beam rotators (PBR), giving rise to a patent [79]. Conventional polarization management network (composed by polarization splitters and/or rotator) is substituted by a so called phase-assisted distribution network. Birefringence of interconnection waveguides in the distribution network is engineered to provide dual-polarization demodulation with improved tolerances to fabrication errors, compared to PBS-based approaches [80].

1.3. Organization of the Thesis

Chapter 2 of this thesis is dedicated to the design and implementation of grating couplers for the SOI micrometric platform. In section 2.1, working principle and state of the art of grating couplers are discussed in detail. Implementation and experimental characterization of high efficiency fiber-to-chip micrometric grating couplers is presented in 2.2.1. This design approach is extended to polarization independent behavior in section 2.2.2. In 2.2.3, the implementation of a grating-based input interface for an integrated spectrometer for spacial applications is discussed. Conclusions of this part of the work are summarized in section 2.3.

Contributions developed in the field of integrated polarization management are presented in Chapter 3. State of the art of integrated polarization rotators is discussed in 3.2, focusing on the operation of rotator-waveguide-based devices. In section 3.2.1, the InP integrated polarization rotator fully compatible with a previously developed monolithic downconverter is presented. In section 3.2.2, working principle of proposed general polarization rotator scheme is discussed. In section 3.3, operation of the proposed PBS-less receiver architecture is analyzed in detail.

Finally, work presented in the previous sections is reviewed in Chapter 4, detailing what problem is faced and what solution is proposed in each design. Besides, the prospects and other contributions developed during the thesis, not included in this manuscript, and are briefly summarized.

1.4. Technology Platforms and Waveguides

A wide variety of technology platforms have been developed for the implementation of commercial photonic applications, each with specific strengths (and weaknesses). To mention a few, nonlinear crystals ($\mathrm{LiNbO_3}$) enable implementation of high performance modulators, silica offers very low (propagation and coupling) loss, silicon nitride can implement high performance devices in the visible range [81], III-V materials offer light detection and generation, and SOI offers high integration capacity and CMOS compatibility. The Photonics & RF group at the Universidad de Málaga [1] has been closely collaborating with different research groups that focus their activity on different technology platforms. Thus, designs developed for the generally considered competing SOI and InP platforms can be found in this thesis. Far from trying to thoroughly assess these two platforms, the aim of this section is to briefly summarize some characteristics that are relevant for the designs presented in the following chapters.

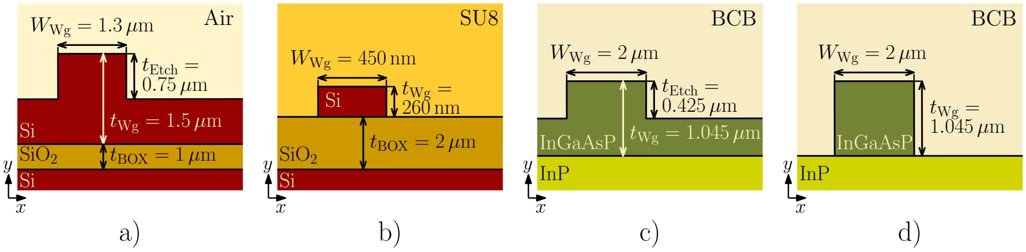

Figure 1.2.: Transversal geometry of **a)** SOI rib, **b)** Si-wire, **c)** InP rib, and **d)** InP strip waveguides.

Table 1.1.: Summary of technological parameters of interconnection waveguides considered in this thesis.

Waveguide type	Waveguide thickness	Minimum bend radius	Minimum feature	Wg. width error range
SOI Rib	1.5 μm	900 μm [82]	350 nm [69]	±100 nm [83]
Si-Wire	0.26 μm	4 μm [84]	100 nm [30]	±50 nm [85]
InP Rib	1.045 μm	1000 μm	400 nm	±100 nm
InP Strip	1.045 μm	600 μm	400 nm	±100 nm

One key element of a photonic integrated circuit is the interconnection waveguide, as it largely determines device footprint, reliability and ultimately potential performance. Four different kinds of waveguides, two SOI-based and two InP-based, are considered in this thesis:

- SOI micrometric rib (Fig. 1.2-a): used in the implementation of chip-to-fiber grating couplers discussed in section 2.2.
- Si-wire (Fig. 1.2-b): used in the implementation of a tunable polarization rotator discussed in section 3.2.2.
- InP micrometric rib (Fig. 1.2-c): used in the implementation of a polarization rotator discussed in section 3.2.1.
- InP micrometric strip (Fig. 1.2-d): used in the implementation of a dual-polarization coherent receiver discussed in section 3.3.

Minimum feature size, waveguide width fabrication tolerances and minimum bending radii considered for the designs are summarized in table 1.1. Information regarding the InP waveguides is extracted from the internal reports developed in the frame of the european projects Celtic 100GET [74] and FP7 Mirthe [47].

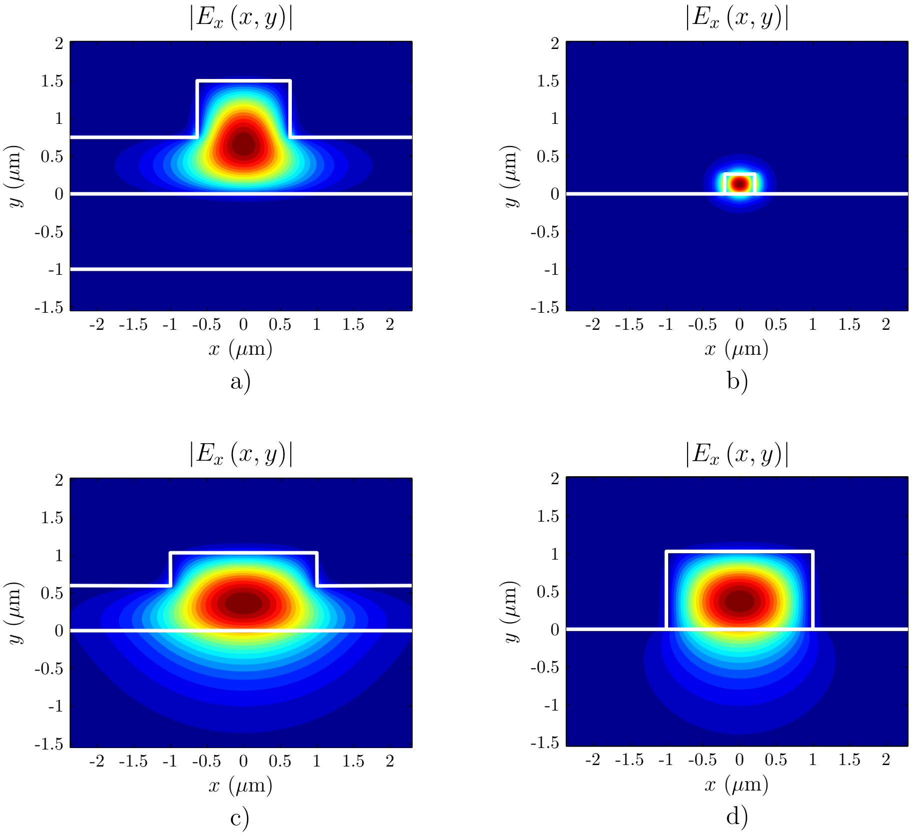

Figure 1.3.: Fundamental TE mode profile of **a)** SOI rib, **b)** Si-wire, **c)** InP rib, and **d)** InP strip waveguides at $1.55\,\mu\mathrm{m}$ wavelength, calculated using full-vectorial commercial tool FimmWave

SOI waveguides are implemented on a three layer wafer, with a top silicon layer (where waveguides are defined), a bottom oxide layer (BOX) and a silicon substrate (that provides mechanical stiffness). The high-index-contrast between the top silicon and the BOX layers provides a strong vertical confinement that avoids leakage to the silicon substrate. SOI-based rib (Figs 1.2-a) and Si-wire (Figs 1.2-b) waveguides considered in this thesis exhibit largely different characteristics. SOI rib waveguide has transversal dimensions of around $1.5\,\mu\mathrm{m}$, whereas Si-wire dimensions are in the order of hundreds of nanometers. Electric field distribution of fundamental transverse-electric (TE) mode of these waveguides is represented in Figs. 1.3-a and 1.3-b. It can be seen that rib mode is mostly confined inside the silicon, while a large part of the Si-wire mode is guided through the waveguide cladding, strongly sensing Si boundaries. Hence, Si-wire modes are much more heavily affected by the boundary conditions than rib ones, leading to larger birefringence. Also, the fact that a strong part of the field is confined in the Si boundary increases the sidewall roughness effect, producing larger propagation loss (typically of $0.1 - 0.5\,\mathrm{dB/cm}$ for micrometric rib, and $1 - 3\,\mathrm{dB/cm}$ for Si-wire). An excellent review of the state of the art of Si-wires can be found in [86]. Although SOI waveguides are generally covered with a protective $\mathrm{SiO_2}$ coating, this layer is removed in this rib waveguide to facilitate grating coupler implementation, and substituted by a polymer (SU8) in the Si-wire design to facilitate the implementation of tunable polarization phase-shifters (please refer to the corresponding sections for in depth explanation).

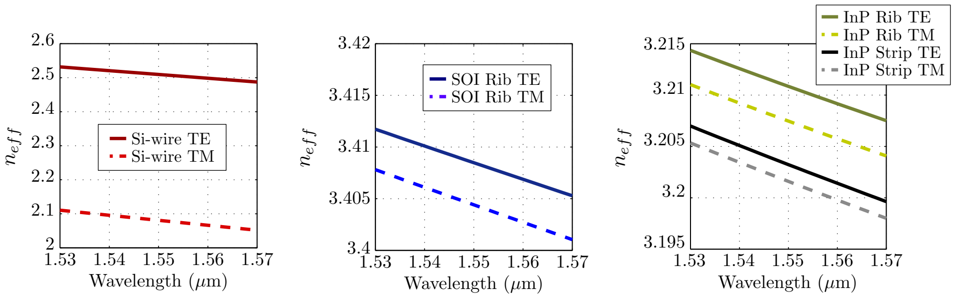

a) b) c)

Figure 1.4.: Effective index of fundamental TE and TM modes of **a)** Si-wire, **b)** SOI rib, and **c)** InP rib and strip waveguides with nominal dimensions, as a function of the wavelength, calculated using full-vectorial commercial tool FimmWave.

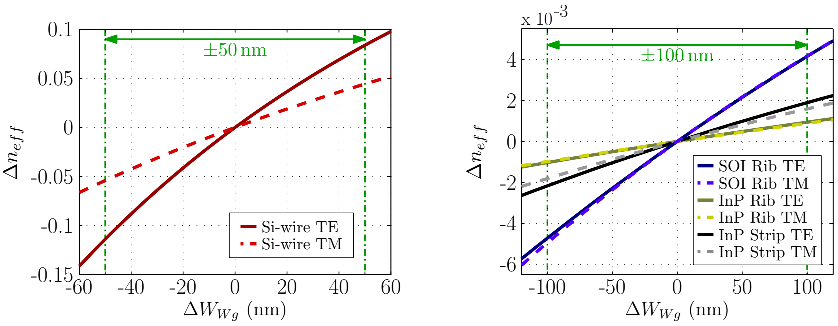

a) b)

Figure 1.5.: Effective index variation of fundamental TE and TM modes of **a)** Si-wire, **b)** SOI rib, and **c)** InP rib and strip waveguides at $1.55\,\mu\mathrm{m}$ wavelength, as a function of waveguide width variation respect to the nominal value, calculated using full-vectorial commercial tool FimmWave.

InP waveguides use InGaAsP as a guiding layer, InP as a substrate, and BCB as a protective coating. Considered rib (Fig. 1.2-c) and strip (Fig. 1.2-d) waveguides have the same waveguide thickness and width, leading a qualitative similar behavior, that slightly differs on the value of the birefringence and bending radius. Figures 1.3-c and 1.3-d show fundamental TE mode filed distribution of both waveguides. Mode field substrate penetration is substantially larger in these InP waveguides than in the SOI ones, due to the reduced index contrast between the guiding and substrate layers. The increased lateral confinement provided by the fully etch strip geometry is also clearly appreciable in the mode field distributions.

Effective indexes of the fundamental transverse-electric (TE) and transverse-magnetic (TM) modes are represented in Fig. 1.4 as a function of the wavelength for the four considered waveguides. Si-wire exhibits a lower effective index than micrometric (SOI and InP) waveguides and, as already mentioned, a far higher birefringence. Each micrometric waveguide provides different effective index and birefringence values.

Figure 1.5 shows effective index variation produced by a given waveguide width deviation from its nominal value (ΔW_{Wg}) for the four waveguides. Is worth noting that, even though waveguide width errors are much tighter for the Si-wire platform ($\pm 50\,\mathrm{nm}$) than for the micrometric waveguides ($\pm 100\,\mathrm{nm}$), the effect of fabrication tolerances on the mode effective index is an order of magnitude larger. Among micrometric waveguides, SOI rib and InP rib are the most and least sensitive to width tolerances, respectively.

2

Grating Couplers

2.1. Introduction

2.1.1. The Chip Coupling Problem

Efficient connection between the integrated chip and external devices, specially standard single-mode optical fibers, is a key functionality for any photonic technology platform that aims to lead the implementation of next generation high performance devices. This issue is remarkably challenging for the SOI waveguides, as they have a large mismatch with standard optical fibers in terms of mode size and refractive index. Direct butt-coupling between a standard optical fiber and standard SOI (micro or nanometric) waveguide would produce coupling loss larger than $12\,\mathrm{dB}$ [87]. Several alternatives, based on coupling through the chip edge, have been proposed to increase coupling efficiency. One option is to focus the light coming from the optical fiber into the waveguide using lensed fibers or lenses integrated in the chip [88]. Another option is to expand the chip waveguide fundamental mode to match the size of the optical fiber fundamental mode. This can be done by means of

- Increasing the waveguide core with i) 3-D tapers (see Fig. 2.1-a) where both, waveguide thickness and width are adiabatically increased [89, 90], or ii) multi-stage tapers (see Fig. 2.1-b) where waveguides of different thicknesses are connected through adiabatic tapers where only the width is changed [87]. This approach requires complex fabrication processes and anti-reflection (AR) coating of the waveguide edge.

- Decreasing the waveguide core (reducing the modal confinement factor and expanding the effective mode size) with i) inverse tapers (see Fig. 2.1-c) where waveguide width is adiabatically reduced [91–93] or ii) sub-wavelength (swg) tapers (see Fig. 2.1-d) where synthesized core refractive index is adiabatically reduced [94, 95]. This approach avoids the need of AR coating but requires tight control of the fabrication process (very sensitive to small width variations).

- Implementing an spot size converter using a multilayer substrate. Optical fiber is edge-coupled to an structured substrate that adiabatically transforms launched field into the chip waveguide fundamental mode [96].

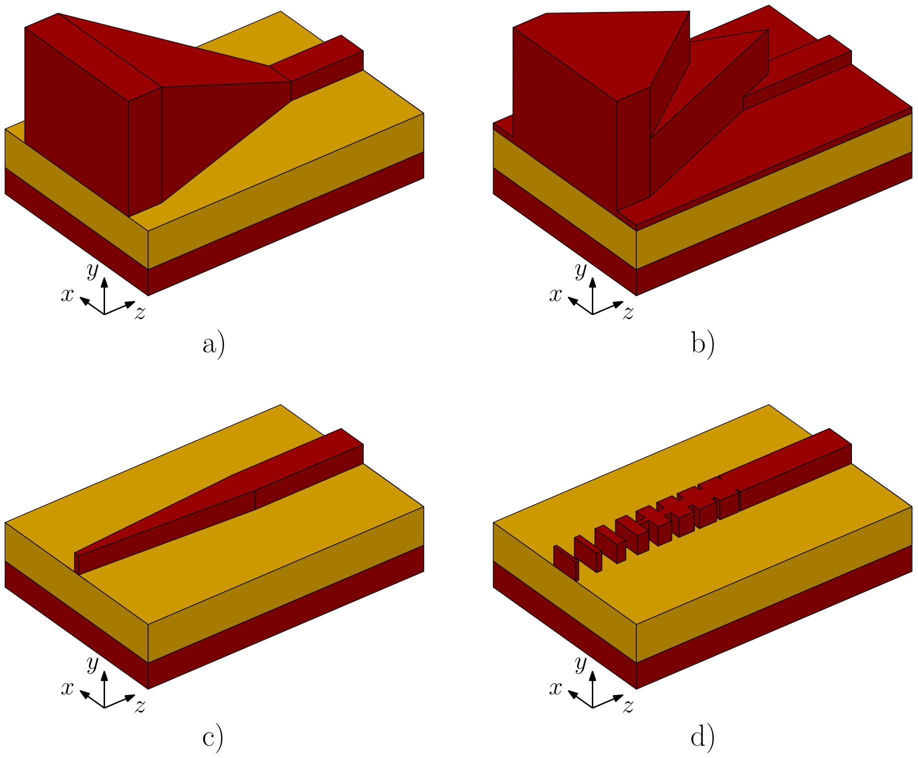

Figure 2.1.: Schematic representation of edge-coupling solutions based on: **a)** 3-D taper, **b)** multi-stage taper, **c)** inverse taper, and **d)** sub-wavelength taper.

Edge-coupling solutions can provide coupling efficiencies better than $-1\,\mathrm{dB}$ simultaneously for both polarizations in a wide wavelength range [93, 94]. However, the fact that all inputs and outputs need to be routed to the chip facet may become a major limitation in increasingly complex devices.

An alternative approach is to couple light in and out through the chip surface using grating couplers. Grating couplers can be placed anywhere in the chip, maximizing scalability, and providing relaxed alignment tolerances. Besides, they allow wafer scale testing, obviating the need to dice and polish individual devices before testing them, and potentially reducing mass production costs [11]. In principle, grating couplers exhibit lower coupling efficiency than edge-coupling solutions due to leakage to the substrate and field profile mismatch with fundamental mode of the fiber. Gratings resonant nature makes them very wavelength and polarization dependent. An enormous effort has been devoted to alleviate these drawbacks. Grating couplers with coupling efficiencies ($\sim -1\,\mathrm{dB}$) that compare to edge-coupling solutions have been experimentally demonstrated [28,40]. Solutions to provide increased bandwidth ($BW_{1\,\mathrm{dB}} \sim 280\,\mathrm{nm}$) [42] and polarization independent performance [35] have also been proposed.

Chip-to-fiber grating couplers have become a key component of the photonic building block library of Luxtera [25] and EpixFab [97]. Grating couplers are used as input-output interface in communication [98] and biosensing applications [99]. Besides, grating couplers are foreseen as a very promising solution for the chip-to-chip interconnection of photonically integrated multi-core systems [100], or the hybrid integration of

III-V photo-detectors [101] and lasers [102].

2.1.2. The Grating Coupler Working Principle

A grating coupler (see Fig. 2.2-a) is a waveguide section where a set of discontinuities, periodically distributed along the propagation direction (z), has been added to produce a radiation beam. Ideally, all the power carried by the fundamental mode of the interconnection waveguide feeding the grating is radiated up and perfectly coupled to an objective field, typically the fundamental mode of an optical fiber. Adiabatic transition between the interconnection waveguide and the grating is provided by an excitation stage, being the direct taper shown in Fig. 2.2-a and 2.2-b the most commonly used solution. The grating geometry is designed to i) maximize power radiated up, and ii) maximize matching between radiated and objective fields.

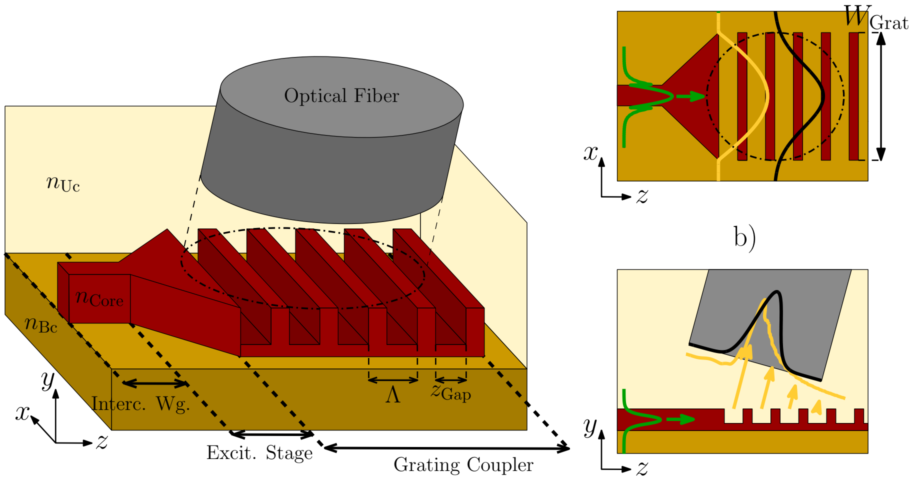

b)

a)

c)

Figure 2.2.: Schematic of chip-to-fiber grating coupler **a)** 3-D structure **b)** $x-z$ plane 2-D model, fundamental mode of interconnection waveguide (green line), access waveguide (yellow line) and optical fiber (black line) **c)** $y-z$ plane 2-D model, fundamental mode distribution along y-axis of interconnection waveguide (green line), optical fiber (black line), and radiated field (yellow line).

Due to reciprocity, grating couplers can be used to inject light to, or extract it from the chip with the same efficiency. The power extraction problem is analyzed hereafter, being all the conclusions also valid for the injecting case. The chip-to-fiber design is considered in the following discussion, being the objective field the fundamental mode of the optical fiber.

The design of the complete 3-D grating structure shown in Fig. 2.2-a is usually divided in the two 2-D problems presented in Figs. 2.2-b and 2.2-c. As the grating width is much larger than its thickness, variable separation can be applied [103]. The field radiated by the grating has an in-plane distribution along the x-axis determined by the fundamental mode of the unperturbed (without discontinuities) waveguide in the grating region (2-D problem depicted in Fig. 2.2-b). The radiated field distribution along the

z-axis is determined by the characteristics of the 2-D grating depicted in Fig. 2.2-c. For uniform gratings (constant discontinuity shape and distribution) radiated field exhibits an exponential-like distribution (yellow line in Fig. 2.2-c).

The $x - z$ plane problem (Fig. 2.2-b) is considered only to determine the grating width and the interconnection-waveguide-to-grating transition (excitation stage). Grating width (W_{Grat}) is designed to maximize matching between the fundamental mode of the unperturbed waveguide (yellow line in Fig. 2.2-b) and the fiber fundamental mode distribution along the x-axis (black solid line in Fig. 2.2-b). Excitation stage is designed to maximize coupling between interconnection waveguide fundamental mode (green line in Fig. 2.2-b) and grating. All the other grating parameters are determined by the $y - z$ plane problem (Fig. 2.2-c).

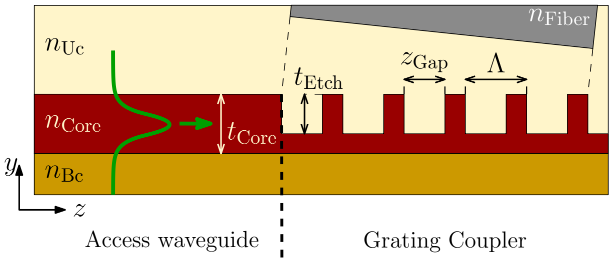

Figure 2.3.: 2-D model of canonical chip-to-fiber grating coupler.

The following discussion is referred to the canonical 2-D grating geometry depicted in Fig. 2.3, where n_{Uc}, n_{Bc}, n_{Core} and n_{Fiber} are the refractive indexes of the upper and bottom claddings, waveguide, and optical fiber, Λ is the grating longitudinal pitch, z_{Gap} is the gap length, t_{Core} is the waveguide thickness, and t_{Etch} is the gap etch depth. Duty cycle is defined as $DC = (\Lambda - z_{\text{Gap}})/\Lambda$. In this structure, access waveguide models wide slab in the grating region ($W_{\text{Grat}} \sim 15\,\mu\text{m}$). Waveguide width variation in taper is not considered. The fundamental mode of the access waveguide (green line in Fig. 2.3) is launched into the grating region to analyze device characteristics.

Bloch-Floquet modes are the solution of Maxwell's equations for periodic structures [104, 105], and thus the modes propagating along the grating. Conventional z-invariant waveguide modes are defined by a field distribution along the transversal (y) direction and a complex propagation constant ($\Gamma = \alpha + j\beta$). Bloch-Floquet modes are defined by a field distribution along a period in the $y - z$ plane, $\vartheta(y, z)$, and a propagation constant Γ_{B_o}. Propagation along the periodic structure can be calculated as

$$\vartheta(y, z + \Lambda) = \vartheta(y, z) \cdot e^{\Gamma_{\text{B}_o}\Lambda}. \tag{2.1}$$

Propagation constant Γ_{B_o} is defined as

$$\begin{aligned} \Gamma_{\text{B}_o} &= \alpha_{\text{B}} + j\beta_{\text{B}_o} \\ &= \alpha_{\text{B}} + j\frac{2\pi}{\lambda}n_{\text{B}}. \end{aligned} \tag{2.2}$$

λ is the wavelength (in vacuum). n_{B} is the mode effective index, being its value (that depends on the wavelength) between the core and cladding refractive indexes ($n_{\text{c}} <$

$n_\mathrm{B} < n_\mathrm{Core}$). The attenuation constant α_B accounts for propagation loss, mainly due to radiation and reflections.

Depending on the ratio between longitudinal pitch and the wavelength, periodic structures can be classified as:

- Non-diffractive structures ($\frac{\Lambda}{\lambda} < \frac{1}{2n_\mathrm{B}}$): also known as subwavelength grating (swg) structures, have an structural pitch shorter than half the wavelength propagating along the structure, and behave as an equivalent homogeneous waveguide with synthesized refractive index n_B [106].

- Reflective structures ($\frac{\Lambda}{\lambda} = \frac{r}{2n_\mathrm{B}}$ with r an positive integer): also known as Bragg gratings, have an structural pitch such that partial reflections in each discontinuity add in phase, and ideally behaves as a perfect reflector.

- Diffractive structures ($\frac{\Lambda}{\lambda} > \frac{1}{n_\mathrm{B}+\mathrm{Max}(n_{Uc},n_{Bc})}$): have an structural pitch large enough to produce radiation.

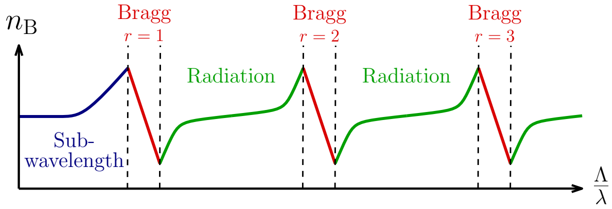

Figure 2.4.: Schematic representation of the Bloch-Floquet mode effective index (n_B) of a periodic waveguide versus the pitch-to-wavelength ratio (Λ/λ).

Figure 2.4 schematically represents Bloch-Floquet effective index (n_B) variation as a function of the pitch-to-wavelength ratio (Λ/λ). In the, so called, Bragg regions (red lines in Fig. 2.4) the condition $\frac{\Lambda}{\lambda} = \frac{r}{2n_\mathrm{B}}$ is met (n_B linearly varies with pitch) and the device behaves as a reflective structure. Devices with pitch shorter than those in the first order Bragg region (blue line in Fig. 2.4), behave as non-diffractive, swg, structures. Devices with larger pitches, that are not inside the Bragg regions, (green lines in Fig. 2.4) behave as diffractive structures, and can produce radiation. Grating couplers are designed to be in the diffraction region, being their behavior discussed in detail below.

Field distribution of a Bloch-Floquet mode can be decomposed as an harmonic sum as

$$\vartheta(y,z) = \sum f_k(y) \cdot e^{\Gamma_{\mathrm{B}_k} z}, \tag{2.3}$$

where k is an integer representing the harmonic order, $f_k(y)$ is the harmonic field distribution along the y-axis and Γ_{B_k} is the Bloch-Floquet harmonic propagation constant

$$\begin{aligned} \Gamma_{\mathrm{B}_k} &= \Gamma_{\mathrm{B}_o} + j\frac{2\pi}{\Lambda}k \\ &= \alpha_\mathrm{B} + j\beta_{\mathrm{B}_k}, \end{aligned} \tag{2.4}$$

and β_{B_k} is the Bloch-Floquet harmonic phase constant

$$\begin{aligned} \beta_{\mathrm{B}_k} &= \beta_{\mathrm{B}_o} + \frac{2\pi}{\Lambda}k \\ &= \frac{2\pi}{\lambda}n_{\mathrm{B}} + \frac{2\pi}{\Lambda}k. \end{aligned} \tag{2.5}$$

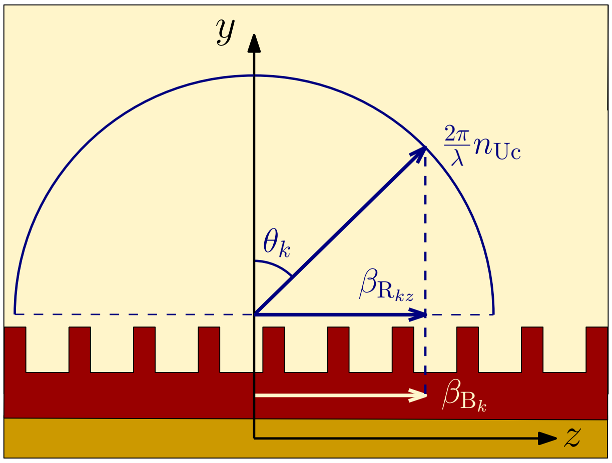

Figure 2.5.: Phase matching condition for harmonic radiation in the upper cladding.

In diffractive structures, some harmonics may exist that propagate away from the structure with an angle θ_k (defined from the vertical y axis as depicted in Fig. 2.5). Those harmonics have a longitudinal field component ($\beta_{\mathrm{R}_{kz}}$) in the (bottom or upper) cladding defined as

$$\beta_{\mathrm{R}_{kz}} = \frac{2\pi}{\lambda}n_{\mathrm{c}}\sin(\theta_k), \tag{2.6}$$

with $n_{\mathrm{c}} = n_{\mathrm{Uc}}$ or n_{Bc} for radiation in the upper or bottom cladding, that matches the Bloch-Floquet harmonic phase constant β_{B_k}

$$\begin{aligned} \beta_{\mathrm{R}_{kz}} &= \beta_{\mathrm{B}_k} \\ \frac{2\pi}{\lambda}n_{\mathrm{c}}\sin(\theta_k) &= \beta_{\mathrm{B}_o} + \frac{2\pi}{\Lambda}k. \end{aligned} \tag{2.7}$$

This phase matching condition is graphically depicted in Fig. 2.5 for radiation in the upper cladding.

Phase matching condition in eq. (2.7) can be rewritten as the very well known grating equation [104]

$$n_c\sin(\theta_k) = n_{\mathrm{B}} + k\frac{\lambda}{\Lambda}. \tag{2.8}$$

Since θ_k must be a real number

$$|\sin(\theta_k)| \leq 1, \tag{2.9}$$

it is clear from eq. (2.8) that

$$\left|n_{\mathrm{B}} + k\frac{\lambda}{\Lambda}\right| \leq n_c. \tag{2.10}$$

As $n_{\mathrm{B}} > n_c$, only harmonics with a negative order ($k = -1,\ -2,\ ...$) can be radiated.

Far from the Bragg regions, Bloch-Floquet effective index (n_{B}) is determined by the materials, duty cycle and gap etch depth, being almost independent of the grating pitch [104]. Thus, looking at eq. (2.10), it can be concluded that, for a given wavelength and grating configuration (materials, duty cycle and gap etch depth that fix n_{B}) the harmonic orders that can radiate are determined by the grating pitch. In fact, the k-th harmonic can radiate only if grating pitch meets the following condition

$$\begin{aligned} \Lambda_{Min_k} <& \quad \Lambda \quad < \Lambda_{Max_k} \\ \frac{-k\lambda}{n_{\mathrm{c}} + n_{\mathrm{B}}} <& \quad \Lambda \quad < \frac{k\lambda}{n_{\mathrm{c}} - n_{\mathrm{B}}}, \end{aligned} \tag{2.11}$$

where Λ_{Min_k} and Λ_{Max_k} are the shortest and longest pitches that allow radiation of the k-th harmonic.

If a single-beam radiation is required, as it is the case for chip-to-fiber grating couplers, only one harmonic should be able to radiate. Tamir and Peng [104] were the first to propose conditions for the grating pitch design to avoid radiation of higher order harmonics. In order to have a single ($k = -1$) harmonic radiation, grating pitch has to be shorter than the minimum pitch for $k = -2$ radiation, and enable $k = -1$ radiation, which leads to the following single-beam radiation condition

$$\begin{aligned} \Lambda_{Min_{-1}} <& \quad \Lambda \quad < min\{\Lambda_{Max_{-1}},\, \Lambda_{Min_{-2}}\} \\ \frac{\lambda}{n_{\mathrm{B}} + n_c} <& \quad \Lambda \quad < min\{\frac{\lambda}{n_{\mathrm{B}} - n_c},\, \frac{2\lambda}{n_c + n_{\mathrm{B}}}\}. \end{aligned} \tag{2.12}$$

Considering eq. (2.7), and imposing eq. (2.10), it can be found that only harmonics with phase constant

$$|\beta_{\mathrm{B}_k}| \leq \frac{2\pi}{\lambda} n_{\mathrm{c}} \tag{2.13}$$

can radiate.

Phase matching condition in eq. (2.7) is graphically represented in Fig. 2.6 for different grating configurations of interest.

- Subwavelength and first order ($r = 1$) Bragg regions (Fig. 2.6-a): grating pitch is shorter than the minimum pitch for $k = -1$ radiation, so $\Lambda < \frac{\lambda}{n_{\mathrm{c}}+n_{\mathrm{B}}}$ and $\beta_{\mathrm{B}_k} < -\frac{2\pi}{\lambda} n_{\mathrm{c}}$.

- Single-beam ($k = -1$) radiation region (Fig. 2.6-b): grating pitch meets eq. (2.12) so $-\frac{2\pi}{\lambda} n_{\mathrm{c}} < \beta_{\mathrm{B}_{-1}} < \frac{2\pi}{\lambda} n_{\mathrm{c}}$ and $\beta_{\mathrm{B}_{-2}} < -\frac{2\pi}{\lambda} n_{\mathrm{c}}$. Thus only $k = -1$ harmonic can radiate.

- Radiation perpendicular to the chip surface (Fig. 2.6-c): radiation angle is $\theta_{-1} = 0°$, from eq. (2.8) it can be found that grating meets Bragg condition ($\Lambda = r\frac{\lambda}{2n_{\mathrm{B}}}$ with $r = 2$), and behaves as a reflector. Therefore chip-to-fiber grating couplers are usually designed with a tilted radiation angle to avoid large Bragg back-reflections.

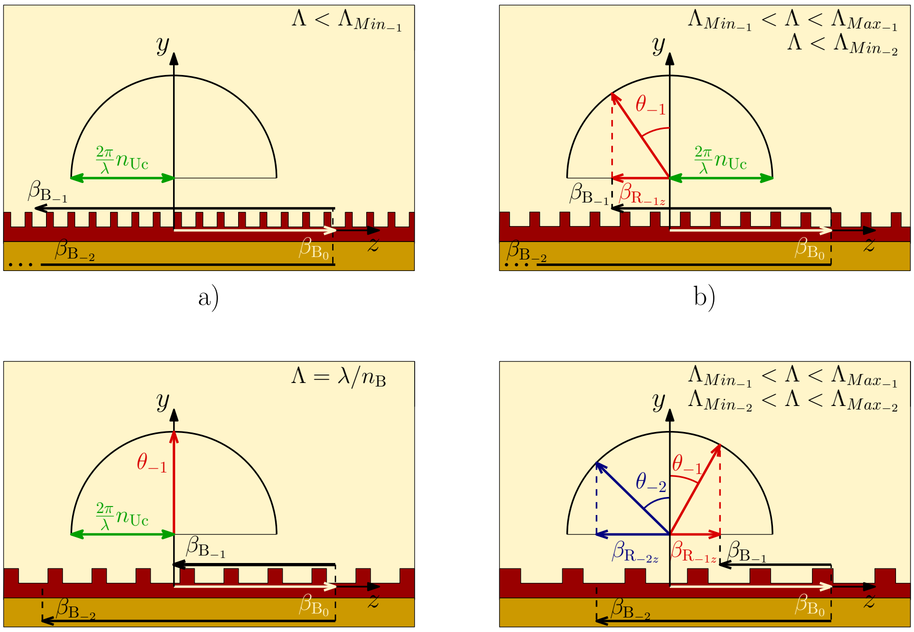

a) b) c) d)

Figure 2.6.: Examples of phase matching condition in eq. (2.7) for gratings in **a)** subwavelength and first order ($r = 1$) Bragg regions **b)** single-beam ($k = -1$) radiation region, **c)** radiation perpendicular to the chip surface, and **d)** multiple-beam ($k = -1, -2$) radiation region.

- Multiple-beam ($k = -1, -2$) radiation region (Fig. 2.6-d): each harmonic propagates with a different angle θ_k. Only one of them can be properly phase-matched with the fundamental mode of the collecting optical fiber, leading to potentially poor coupling efficiencies. Thus, single-beam radiation is usually preferred for chip-to-fiber grating couplers.

The Grating Coupler as an Antenna Array

An alternative, and maybe more intuitive, way to understand a diffractive grating is to see it as an antenna array where each discontinuity acts as an individual radiator. Input field (coming from the access waveguide) travels through the grating feeding each individual radiator. Radiators are excited with an exponentially decaying amplitude and linear phase, determined by the Bloch-Floquet attenuation (α_B) and phase (β_{B_o}) constants, as schematically depicted in Fig. 2.7.

Normalized radiation pattern [107], $F(\theta)$, of an array is determined by the product of the normalized pattern of a single radiator, $g_a(\theta)$, and the normalized complete array factor, $CAF(\theta)$, as

$$F(\theta) = g_a(\theta) \cdot \frac{CAF(\theta)}{max\{CAF(\theta)\}}. \tag{2.14}$$

$CAF(\theta)$ determines the angles at which the contribution of all the individual radiators

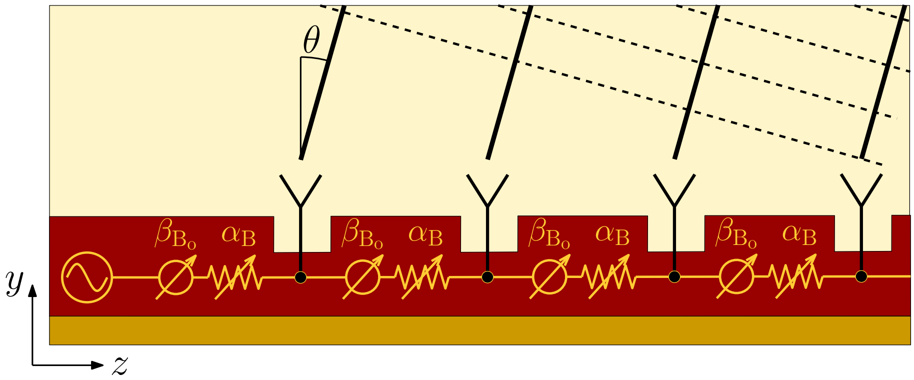

Figure 2.7.: Schematic representation of a grating coupler as an antenna array.

(discontinuities) adds constructively or destructively, and thus which are the possible radiation angles. Grating array factor is then a very useful tool to predict the number of radiation beams (and their angles) of a grating coupler. $CAF\,(\theta)$ of a grating coupler is defined by the Bloch-Floquet propagation constant ($\Gamma_{\mathrm{B}_o} = \alpha_{\mathrm{B}} + j\frac{2\pi}{\lambda}n_{\mathrm{B}}$), the separation between the radiators (grating pitch, Λ), the number of grating periods (NP) and the cladding refractive index (n_{c}) as

$$CAF\,(\theta) = \sum_{n=0}^{NP-1} e^{-\alpha_{\mathrm{B}} n} \cdot e^{j\frac{2\pi}{\lambda}\Lambda n [n_{\mathrm{c}} \sin(\theta) - n_{\mathrm{B}}]}. \tag{2.15}$$

If accurate beam width estimation is not required, as it is the case, the effect of α_{B} can be obviated. Then, the following simplified grating array factor can be defined

$$AF\,(\theta) = \sum_{n=0}^{NP-1} e^{j\frac{2\pi}{\lambda}\Lambda n [n_{\mathrm{c}} \sin(\theta) - n_{\mathrm{B}}]}. \tag{2.16}$$

Expression in eq. (2.16) is used hereafter for the calculation of grating array factors.

Figure 2.8 compares the actual radiation diagram of a grating coupler (extracted from the simulation of the complete grating structure when the fundamental mode of the access waveguide is launched into the grating) and its normalized array factor for two different grating pitches. Grating array factor accurately predicts radiation angles. Relative amplitude between different radiation beams is strongly related to normalized pattern of a single radiator [108], and can not be estimated with array factor.

2.1.3. The Chip-to-Fiber Grating Coupler Design

In this section the design of grating couplers for chip-to-fiber interconnection is analyzed and some relevant solutions proposed in literature are also reviewed.

Fiber coupling efficiency, CE, is usually the figure of merit to maximize in the chip-to-fiber grating coupler design. CE is defined as the ratio between the power coupled to the fundamental mode of the collecting optical fiber (P_{Fiber}) and the power incident into the grating (P_{Inc}), carried by the fundamental mode of the access waveguide. This

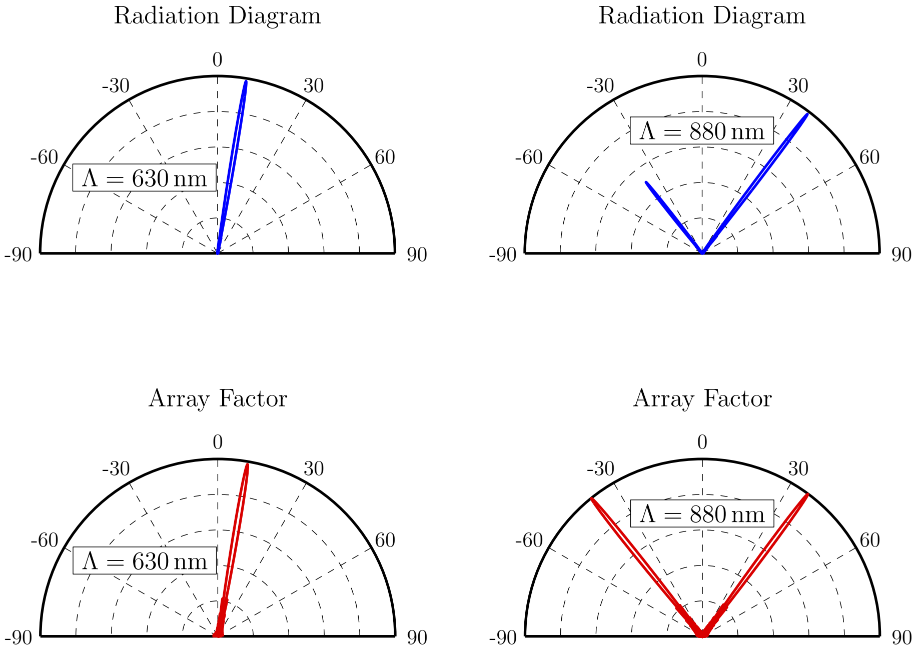

a) b)

Figure 2.8.: Radiation diagram and normalized array factor for grating coupler with $n_{\mathrm{Core}} = 3.476$ (silicon), $n_{\mathrm{Uc}} = n_{\mathrm{Bc}} = 1.444$ (silicon dioxide), $t_{\mathrm{Core}} = 220\,\mathrm{nm}$, $t_{\mathrm{Etch}} = 70\,\mathrm{nm}$, $DC = 0.5$, $\lambda = 1.55\,\mu\mathrm{m}$ and **a)** $\Lambda = 630\,\mathrm{nm}$, **b)** $\Lambda = 880\,\mathrm{nm}$.

coupling efficiency can be expressed as

$$CE = \frac{P_{\mathrm{Fiber}}}{P_{\mathrm{Inc}}} = (1 - \rho_{\mathrm{Reflec}}) \cdot \eta_{\mathrm{Up}} \cdot \eta_{\mathrm{OL}}, \tag{2.17}$$

where the reflection coefficient (ρ_{Reflec}) is the ratio between the power incident to the grating and the power reflected back, the directionality (η_{Up}) is the ratio between the power injected to and radiated up by the grating, and the factor η_{OL} is the fraction of power radiated up that is coupled to the fundamental mode of the optical fiber.

An ideal grating coupler would have no back-reflections ($\rho_{\mathrm{Reflec}} = 0$), would radiate all the power up ($\eta_{\mathrm{Up}} = 1$) and would couple all the power radiated up to the fundamental mode of the fiber ($\eta_{\mathrm{OL}} = 1$).

Other relevant figures of merit of a grating coupler are the bandwidth, and the polarization dependent performance. Table 2.1 summarizes main characteristics of most relevant grating couplers (at the discretion of the author) proposed since Taillaert et al. [26] published their implementation for Si-wires in 2002. Optimization of the parameters determining CE, bandwidth, and some different approaches proposed to cope with polarization are discussed below.

Back-reflections

Two are the sources of back-reflections in a grating coupler: i) constructive interference of partial reflections in each discontinuity (Bragg reflections), and ii) mode mismatch between the fundamental mode of the access waveguide and the grating Bloch-Floquet mode.

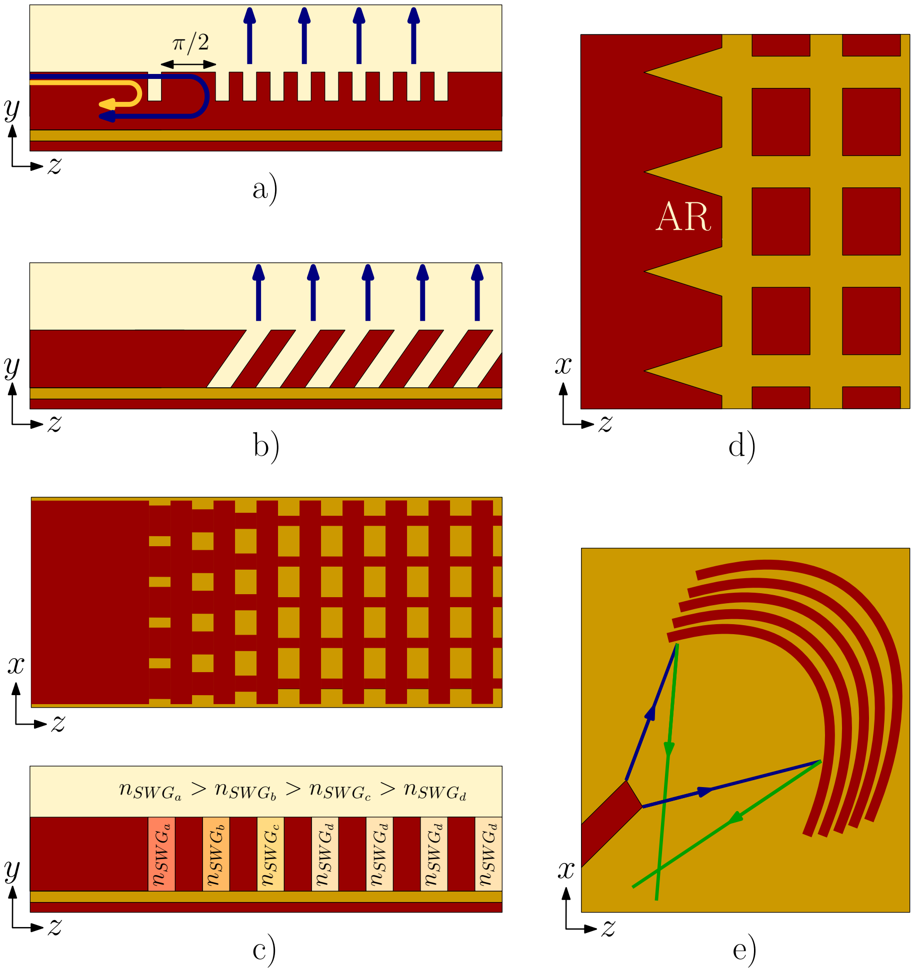

Figure 2.9.: Schematic representation of: **a)** vertically radiating grating with extra slit for Bragg reflection cancellation, **b)** vertically radiating grating with blazed teeth, **c)** sub-wavelength apodized grating for mode mismatch reflection mitigation, **d)** sub-wavelength anti-reflection (AR) layer for mode mismatch reflection mitigation, and **e)** curved grating to redirect back-reflections away from input waveguide.

Constructive interference of back-reflections occurs for gratings meeting the Bragg condition

$$\frac{\Lambda}{\lambda} = \frac{r}{2n_\mathrm{B}}, \tag{2.18}$$

with r a positive integer. From eq. (2.8) it can be found that gratings with radiation angle perpendicular to the chip surface ($\theta_k = 0°$) meet the Bragg condition (and have large back-reflections). Thus, most of grating couplers found in literature are designed to have a tilted radiation angle. However, placing a titled fiber on top of the chip is mechanically demanding, and therefore alternatives to suppress Bragg reflection in vertically radiating gratings have been investigated. One of the alternatives is introducing an extra reflection that interferes with the coupler Bragg reflection canceling it. This can by done by means of an extra teeth [33] (see Fig. 2.9-a) or even a reflecting grating [26]. Separation between the extra reflector and the grating is crucial to produce desired Bragg reflection cancellation (π phase difference between both reflections). A different approach is the use of gratings with blazed teeth (see Fig. 2.9-b), that provide radiation perpendicular to the chip surface with low back-reflections [32]. The use of swg structures that synthesize a blazed refractive index distribution along the z-axis has also been proposed [109].

Mode mismatch between waveguide and grating modes is related to the teeth effect. The wider and deeper the teeth, the larger the mismatch. For that reason many designs [26–28, 110] use a shallow etch in the grating region (typically a $70\,\mathrm{nm}$ etch in a $220-260\,\mathrm{nm}$ thick waveguide), different from the deep etch used to define the waveguides. Devices that use two different shallow etch depths [34,39] or the lag effect have also been proposed [111]. Adding an extra etch step to the process increases manufacturing costs. The following alternatives have been proposed to implement single-etch step grating couplers with low back-reflections:

- Reduce the index contrast in the teeth-to-core boundary, using lower index contrast platforms. Back-reflections of $-22\,\mathrm{dB}$ can be achieved using silicon nitride core and silicon dioxide cladding [112].

- Introduce a transversal swg along the grating gaps (see Fig. 2.9-c). Swg allows to reduce the strength (teeth effect) of the grating at the beginning of the structure to implement a smooth waveguide-to-grating transition. Back-reflections of $-30\,\mathrm{dB}$ have been experimentally demonstrated based on this approach [29].

- Introduce an anti-reflection (AR) layer between the waveguide and the grating (see Fig. 2.9-d). Swg AR layers have been successfully used in Echelle gratings [113]. Chip-to-fiber grating couplers with AR layer have shown back-reflections of $-24\,\mathrm{dB}$ [114].

- Adapting the excitation field to match Bloch-Floquet mode in the grating region, allows back-reflections of $-27\,\mathrm{dB}$ [61]. This approach, that is one of the main contributions of this thesis is discussed in detail in section 2.2.1.

An alternative approach consists on redirecting back-reflections out of the access waveguide, rather than avoiding them. Grating couplers with gap lines following and elliptical distribution in the $x-z$ plane have been proposed that focus the field collected by the grating into the waveguide, substantially reducing excitation stage length (compared to conventional adiabatic tapers) [25, 37, 115, 116]. Recently, a modified gap line distribution has been proposed that focus back-reflected power away from the access waveguide (see Fig. 2.9-e), demonstrating back-reflections of $-50\,\mathrm{dB}$ [117].

Directionality

Directionality can be calculated as

$$\eta_{\mathrm{Up}} = \frac{P_{\mathrm{Up}}}{P_{\mathrm{Up}} + P_{\mathrm{Down}} + P_{\mathrm{Tx}}}, \tag{2.19}$$

being P_{Up}, P_{Down} the power radiated up and down by the grating and P_{Tx} the power that goes through the grating (is not radiated). P_{Tx} is minimized by properly choosing the number of periods (make grating long enough to radiate all the injected power). Assuming $P_{\mathrm{Tx}} \sim 0$, all the power injected into the grating is radiated up or down, and $\eta_{\mathrm{Up}} \sim P_{\mathrm{Up}}/(P_{\mathrm{Up}} + P_{\mathrm{Down}})$. Two are the alternatives found in literature to optimize directionality:

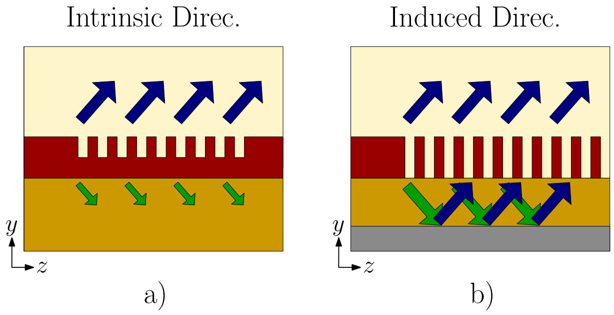

Figure 2.10.: Schematic representation of grating coupler with **a)** etch depth optimization for high intrinsic directionality, and **b)** bottom reflector for high induced directionality.

- Optimize intrinsic directionality, i.e. power radiated up by the grating surrounded by infinite upper and bottom claddings (Fig. 2.10-a). Grating couplers that are vertically symmetric have a directionality of $\eta_{\mathrm{Up}} = 0.5$ [108]. Grating couplers with high intrinsic directionality break this vertical symmetry to increase power radiated up [108]. Directionalities higher than $\eta_{\mathrm{Up}} > 0.8$ have been demonstrated for structures based on etch depth optimization [34, 40, 61] or the use of polysilicon [118] or amorphous silicon [110] overlays in the grating region. Remarkably high directionality of $\eta_{\mathrm{Up}} > 0.9$ can be achieved using a double-teeth configuration [39].

- Optimize induced directionality, i.e. using partially or totally reflecting bottom mirrors to redirect up the power that is radiated down (Fig. 2.10-b). Gratings that redirect the power radiated down optimize mirror position or radiation angle to achieve constructive interference in the upper cladding and improve directionality. SOI grating couplers using the partial reflection produced in the BOX-to-substrate interface have been demonstrated with directionalities of $\eta_{\mathrm{Up}} > 0.8$ [27, 33, 37, 38, 42, 111]. Mirrors implemented with metals [28, 36, 69, 116], multilayer structures [26, 35] or swg structures [119] have also been proposed that exhibit directionalities of $\eta_{\mathrm{Up}} \sim 1$.

Radiated Field to Optical Fiber Matching

Fraction of power radiated up that is coupled to the fundamental mode of the optical fiber can be calculated as

$$\eta_{\mathrm{OL}} = \frac{|\langle E_{\mathrm{Up}}, E_{\mathrm{Objec}} \rangle|^2}{\langle E_{\mathrm{Up}}, E_{\mathrm{Up}} \rangle \langle E_{\mathrm{Objec}}, E_{\mathrm{Objec}} \rangle}, \tag{2.20}$$

where E_{Up} is the field radiated up, E_{Objec} is the fundamental mode of the optical fiber, and $\langle a, b\rangle$ denotes the overlap integral defined as

$$\langle a, b\rangle = \int a \cdot b^{*} \mathrm{d}z', \tag{2.21}$$

being z' the axis along which the fundamental mode of the optical fiber is defined. Note that radiated field and fundamental mode need to match in amplitude and phase to maximize coupled power. In a multi-beam radiating grating, each beam propagates with a different angle (θ_k), and therefore only one of them can be in-phase with the fundamental mode of the optical fiber, leading to a low coupling efficiency. For that reason, single-beam radiating gratings are preferred for the implementation of chip-to-fiber interconnects.

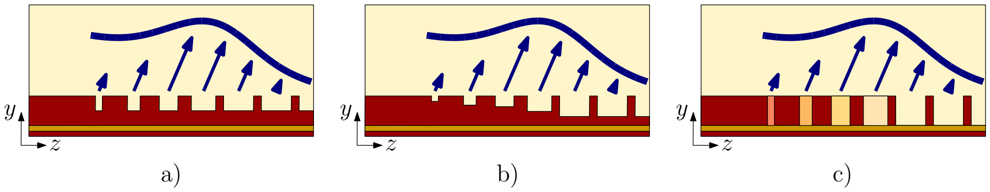

Figure 2.11.: Schematic representation of grating couplers with η_{OL} optimization based on **a)** duty cycle apodization, **b)** etch depth and duty cycle apodization, and **c)** swg apodization.

Field radiated by an uniform grating (constant pitch and gap shape) has an exponential-like distribution determined by the grating strength (defined by the term α_{B} of the Bloch-Floquet propagation constant) [104]. Fundamental mode of the fiber has a Gaussian-like distribution. Maximum overlap between an exponential and a Gaussian is $\eta_{\mathrm{OL}} \sim 0.8$ [61]. If higher coupling ratios are aimed, non-uniform (apodized) gratings need to be used, that vary the grating strength to reshape the radiated field, adapting it to the desired Gaussian profile [103]. Overlap efficiencies of $\eta_{\mathrm{OL}} > 0.9$ have been shown for structures based on:

- Duty cycle apodization (Fig. 2.11-a): duty cycle is reduced at the begining of the grating to reduce grating strength [28, 32, 33, 40].
- Etch depth apodization (Fig. 2.11-b): etch depth is reduced at the begining of the grating to reduce grating strength [34, 111].
- Swg apodization (Fig. 2.11-c): synthesized refractive index in gaps is increased (and thus grating strength is reduced) at the beginning of the grating to reduce grating strength [29, 30, 37, 38].

Note that to maximize overlap both, amplitude and phase need to be matched. Thus, grating pitch needs to be properly adjusted to maintain radiation angle constant along the apodized structure.

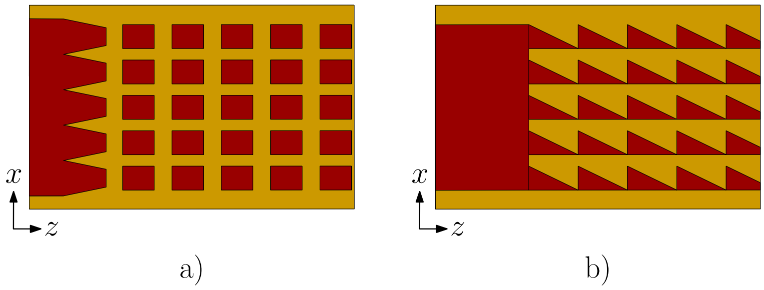

Figure 2.12.: Schematic representation of grating coupler with Bloch-Floquet mode effective index reduction for bandwidth increasing based on **a)** swg square stripes separated by gaps, and **b)** swg triangular structure.

Bandwidth

Most of the grating coupler designs found in literature are focused on maximizing peak coupling efficiency, but the subject of bandwidth is gaining attention. As an antenna array, grating couplers perform the so called angle frequency scanning, i.e. radiation angle changes with the wavelength [107]. This angle variation is the main limitation of coupling efficiency bandwidth [112].

From eq. (2.8), and substituting $\lambda = \lambda_o + \Delta\lambda$ and $\theta_k = \theta_{ko} + \Delta\theta$ it can be found that angle variation with wavelength is proportional to

$$\frac{\Delta\theta}{\Delta\lambda} = \frac{n_\mathrm{c}\sin(\theta_{ko}) - n_\mathrm{B}}{\lambda_o n_\mathrm{c}\cos(\theta_{ko})}. \tag{2.22}$$

Radiation angle is usually designed to be slightly titled from the vertical ($\theta_k \sim \pm 10°$), thus $|n_\mathrm{c}\sin(\theta_{ko})| \ll n_\mathrm{B}$. Then, from eq. (2.22) it is clear that, reducing grating Bloch-Floquet mode effective index (n_B) reduces $\Delta\theta/\Delta\lambda$ and increases bandwidth. Two are the alternatives found in literature to reduce n_B:

- Use lower reffractive index materials. Silicon nitride grating couplers have shown a 1 dB bandwidth of 67 nm [112].

- Use transversal swg structures. A 1 dB bandwidth of 73 nm has been experimentally demonstrated for a grating alternating gaps and transversal swg stripes (see Fig. 2.12-a) [114]. A remarkable 1 dB bandwidth of 290 nm has theoretically been shown for a grating based on triangular swg structures (see Fig. 2.12-b) [42].

Polarization

Performance of grating couplers is generally strongly polarization dependent [26, 112]. Equation (2.8), repeated here for the TE and TM cases for clarity,

$$\begin{aligned} n_c\sin(\theta_k^{\mathrm{TE}}) &= n_\mathrm{B}^{\mathrm{TE}} + k\frac{\lambda}{\Lambda} \\ n_c\sin(\theta_k^{\mathrm{TM}}) &= n_\mathrm{B}^{\mathrm{TM}} + k\frac{\lambda}{\Lambda} \end{aligned} \tag{2.23}$$

shows that the radiation angle (θ_k^{TE}, θ_k^{TM}) depends on Bloch-Floquet effective index ($n_{\mathrm{B}}^{\mathrm{TE}}$, $n_{\mathrm{B}}^{\mathrm{TE}}$). Bloch-Floquet effective index is largely different for TE and TM polarizations in Si-wire gratings ($n_{\mathrm{B}}^{\mathrm{TE}} \sim 2.8$, $n_{\mathrm{B}}^{\mathrm{TM}} \sim 2$ for a $200\,\mathrm{nm}$ Si thickness based grating). Therefore radiation angles are also very different and achieving high coupling efficiency for both polarizations is not feasible. For that reason, most gratings are designed to couple only one, TE or TM, polarization.

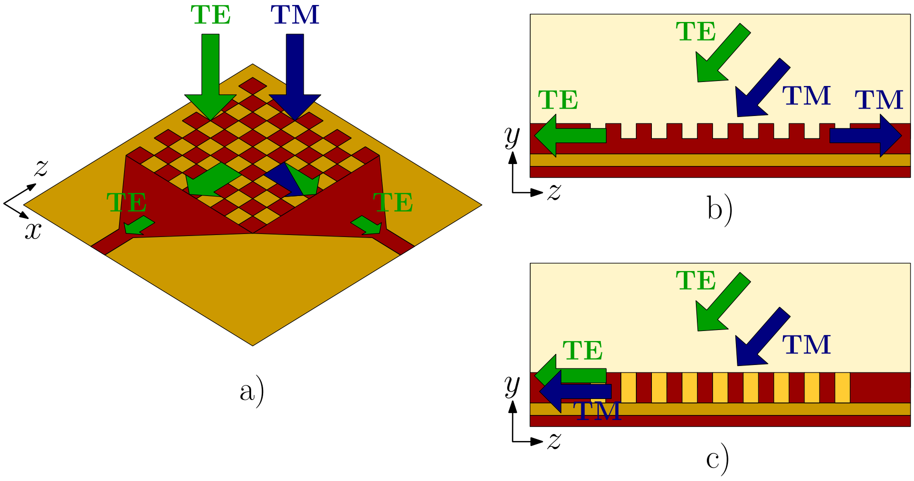

Figure 2.13.: Schematic representation of: **a)** 2-D grating coupler for polarization splitting and TM-to-TE rotation, **b)** grating coupler for polarization splitting, and **c)** grating coupler for polarization independent behavior.

Three are the main approaches found in literature to cope with this strong polarization dependence:

- Polarization splitter-rotator 2-D grating: two grating couplers (one for TE and another for TM) are superimposed in a 2-D grid, as shown in Fig. 2.13-a. Each orthogonal polarization is coupled into a different output waveguide, being the incoming TM polarization rotated to TE [41]. Coupling efficiencies of $-3.2\,\mathrm{dB}$ for both TE and TM polarizations has been experimentally demonstrated [25].

- Polarization splitter grating: structure pitch is designed to provide opposite radiation angles for TE and TM ($\theta_{-1}^{TE} = -\theta_{-1}^{TM}$). This way orthogonal polarizations impinging into the grating are coupled forward or backward into the waveguide, as schematically depicted in Fig. 2.13-b. A polarization splitter grating with $-2.4\,\mathrm{dB}$ coupling efficiency for both polarizations (at different ports) with an extinction ratio better than $25\,\mathrm{dB}$ has experimentally been demonstrated [36].

- Polarization independent grating based on transversal swg: in a conventional Si-wire TE mode have larger effective index than TM. In a transversal swg structure effective index is larger for TM than for TE. These two effects are compensated to achieve a grating coupler with almost the same Bloch-Floquet effective index for both polarizations ($n_{\mathrm{B}}^{\mathrm{TE}} \sim n_{\mathrm{B}}^{\mathrm{TM}}$). Polarization independent coupling efficiency of $-1.9\,\mathrm{dB}$ has theoretically been shown, based on this approach [35].

Grating couplers based on micrometric waveguides have a lower birefringence, facilitating polarization independent behavior. The design of a polarization independent grating coupler for the micrometric rib SOI platform [69], which is other of the contributions of this thesis, is discussed in detail in section 2.2.2.

Table 2.1.: Overview of chip-to-fiber grating coupler designs from 2002 to now.

Year & Ref.	CE	BW	Exper.	Single Etch	Pol.	Directionality Optimization	Overlap Optimization	Back-Reflec. Optimization	BW Optimiz.	Other
2002 [26]	$-1.3\,\mathrm{dB}$	$3\,\mathrm{dB}$ $15\,\mathrm{nm}$	✗	✗	TE	Induced: multilayer mirror	✗	Extra reflec. grating	✗	Vertical coupling
2003 [41]	$-7\,\mathrm{dB}$	-	✗	✗	TE & TM	-	-	-	✗	2-D grating, pol splitter.
2005 [32]	$-1.2\,\mathrm{dB}$	–	✗	✗	TE	✗	Duty cycle apodiz.	Blazed teeth	✗	Vertical coupling
2006 [27]	$-2.6\,\mathrm{dB}$	$3\,\mathrm{dB}$ $20\,\mathrm{nm}$	✓	✗	TE	Induced: substrate reflec.	✗	✗	✗	–
2007 [33]	$-0.97\,\mathrm{dB}$	-	✗	✗	TE	Induced: substrate reflec.	Duty cycle apodiz.	Extra slit reflec.	✗	Vertical coupling
2007 [39]	$-1.25\,\mathrm{dB}$	$3\,\mathrm{dB}$ $60\,\mathrm{nm}$	✗	✗	TE	Intrinsic: double teeth	✗	Double teeth	✗	-
2009 [29]	$-3\,\mathrm{dB}$	-	✗	✓	TM	✗	Swg apodiz. ($\eta_{\mathrm{OL}} = 0.94$)	Swg apodiz. ($-30\,\mathrm{dB}$)	✗	-
2010 [111]	$-1.9\,\mathrm{dB}$	$1\,\mathrm{dB}$ $43\,\mathrm{nm}$	✓	✗	TE	Induced: substrate reflec.	Etch depth apodiz.	Etch depth apodiz.	✗	-
2010 [61] This Thesis	$-1.8\,\mathrm{dB}$	$3\,\mathrm{dB}$ $40\,\mathrm{nm}$	✗	✓	**TE**	**Intrinsic: etch depth optimi.** ($\eta_{\mathrm{Up}} = 0.89$)	✗	**Mode adaptation** ($-27\,\mathrm{dB}$)	✗	**Micro. rib waveguides**
2010 [110]	$-1.6\,\mathrm{dB}$	$3\,\mathrm{dB}$ $80\,\mathrm{nm}$	✓	✗	TE	Intrinsic: aSi overlay	✗	✗	✗	-

Overview of chip-to-fiber grating coupler designs from 2002 to now.

Year & Ref.	CE	BW	Exper.	Single Etch	Pol.	Directionality Optimization	Overlap Optimization	Back-Reflec. Optimization	BW Optimiz.	Other
2010 [30]	$-3\,\text{dB}$	$3\,\text{dB}$ $60\,\text{nm}$	✓	✓	TM	✗	Swg apodiz.	Swg apodiz. ($-30\,\text{dB}$)	✗	-
2010 [112]	$-4.2\,\text{dB}$	$1\,\text{dB}$ $67\,\text{nm}$	✓	✓	TE	Induced: substrate reflec.	✗	Reduced index contrast ($-22\,\text{dB}$)	Reduced index contrast	Si_3N_4 core
2011 [35]	$-1.9\,\text{dB}$	$3\,\text{dB}$ $65\,\text{nm}$	✗	✓	TE & TM	Induced: multilayer mirror	✗	Swg apodiz. ($-10\,\text{dB}$ TE, $-21\,\text{dB}$ TM)	✗	Pol. independent
2011 [25]	$-3.2\,\text{dB}$	-	✓	✓	TE & TM	-	-	-	✗	2-D grating, inplane focus.
2011 [67]	$-3\,\text{dB}$	$3\,\text{dB}$ $65\,\text{nm}$	✓	✗	TE	Intrinsic: etch depth optimi.	✗	Mode adaptation	✗	Micro. rib waveguides
2011 [63] This Thesis	$-2.2\,\text{dB}$	$3\,\text{dB}$ $40\,\text{nm}$	✓	✓	**TE**	**Intrinsic: etch depth optimi.**	✗	**Mode adaptation** ($-21\,\text{dB}$)	✗	**Micro. rib waveguides.**
2012 [42]	$-2.18\,\text{dB}$	$1\,\text{dB}$ $290\,\text{nm}$	✗	✓	TM	Induced: substrate reflec.	✗	✗	2-D triangular swg	-
2012 [68]	-	-	✓	✗	**TE**	Intrinsic: etch depth optimi. ($\eta_{\text{Up}} = 0.75$)	✗	Mode adaptation	✗	Micro. rib waveguides. photodiode
2012 [114]	$-5.6\,\text{dB}$	$1\,\text{dB}$ $73\,\text{nm}$	✓	✓	TE	✗	✗	AR swg layer ($-14\,\text{dB}$)	Swg index reduction	-

Overview of chip-to-fiber grating coupler designs from 2002 to now.

Year & Ref.	CE	BW	Exper.	Single Etch	Pol.	Directionality Optimization	Overlap Optimization	Back-Reflec. Optimization	BW Optimiz.	Other
2012 [69] This Thesis	$-2.8\,\text{dB}$	-	✗	✓	**TE & TM**	**Intrinsic: etch depth optimi.**	✗	**Mode adaptation**	✗	**Micro. rib waveguides, pol independent.**
2012 [37]	$-3.5\,\text{dB}$	$3\,\text{dB}$ $90\,\text{nm}$	✓	✓	TE or TM	Induced: substrate reflec.	Swg apodiz. ($\eta_{\text{OL}} = 0.95$)	AR swg layer ($-15\,\text{dB}$)	Swg index reduction	Susp wg MIR, inplane focus.
2013 [34]	$-1.5\,\text{dB}$	$3\,\text{dB}$ $54\,\text{nm}$	✓	✗	TE	Intrinsic: etch depth apodiz.	Etch depth apodiz.	Etch depth apodiz.	✗	Two etch depths
2013 [116]	$-2.3\,\text{dB}$	–	✓	✓	TE	Induced: metal mirror	✗	Reduced index contrast	Reduced index contrast	Si_3N_4 core, inplane focus.
2013 [31]	$-2.2\,\text{dB}$	-	✓	✗	TE	Intrinsic: aSi overlay	-	Focus reflec off wg ($-40\,\text{dB}$)	✗	Inplane focus.
2013 [36]	$-2.4\,\text{dB}$	-	✓	✗	TE & TM	Induced: metal mirror	✗	✗	✗	Pol. splitter
2013 [38]	$-1.74\,\text{dB}$	$3\,\text{dB}$ $60\,\text{nm}$	✓	✓	TE	Induced: substrate reflec.	Swg apodiz.	Swg apodiz.	✗	-
2013 [40]	$-1.05\,\text{dB}$	$3\,\text{dB}$ $50\,\text{nm}$	✓	✓	TE	Intrinsic: etch depth optimi.	Duty cycle apodiz.	Duty cycle apodiz.	✗	-
2014 [28]	$-0.62\,\text{dB}$	$1\,\text{dB}$ $40\,\text{nm}$	✓	✗	TE or TM	Induced: metal mirror	Duty cycle apodiz.	Duty cycle apodiz.	✗	-

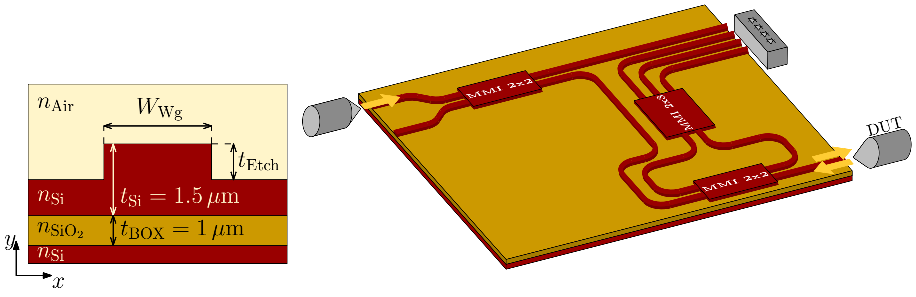

a) b)

Figure 2.14.: a) SOI Rib waveguide transverse geometry. **b)** Schematic of Six-port reflectometer with facet in-out coupling.

2.2. Grating Couplers for Micrometric SOI Rib Waveguides

In this section, the implementation of grating couplers for micrometric rib SOI waveguides, as the one depicted in Fig. 2.14-a, is discussed. The high level of maturity of this technology, together with the reduced propagation loss, lower birefringence and the compatibility with standard i-line stepper lithography make the micrometric SOI platform very attractive for the implementation of high performance devices, including multimode interference couplers [120], arrayed waveguide grating wavelength multi/demultiplexers [121], fourier-transform spectrometers [122] or differential phase-shift keying (DPSK) demodulators [123]. Furthermore, losses bellow $0.02\,\mathrm{dB}$ per 90° bend, with radii of only $10\,\mu\mathrm{m}$ for $4\,\mu\mathrm{m}$ thick SOI waveguides have recently been experimentally demonstrated [43]. This opens the way to integration densities for the micron-scale platform comparable with those of the Si-wires, benefiting from the aforementioned advantages.

Although grating couplers have been successfully used in the Si-wire platform, their implementation in the micrometric platform is not straightforward. Two are the main challenges of micrometric SOI grating couplers:

- Whereas Si-wire grating couplers are vertically single-mode, due to the larger thickness of the micrometric platform (hundreds of nanometers for Si-wire, and $1-5\,\mu\mathrm{m}$ for micrometric waveguides), grating region is vertically multimode.
- Due to the larger minimum feature sizes of their standard fabrication processes ($\sim\,100\,\mathrm{nm}$ for Si-wires and $\sim\,350\,\mathrm{nm}$ for the micrometric platform), eligible grating pitch and duty cycle are limited.

A few innovative solutions that circumvent the intrinsic technology constraints of micrometric SOI grating couplers are proposed in this section. High efficiency grating couplers, implementable with a single standard fabrication etching step, are presented together with a comprehensive design process. This novel approach has opened an exciting path that has been followed by companies such as Intel [67] and Oracle [68].

This section is organized as follows. In 2.2.1 the design and experimental characterization of a micrometric rib SOI chip-to-fiber grating coupler is discussed in detail. In

2.2.2 the grating design is extended to provide polarization independent behavior. Finally, in 2.2.3, the design and experimental characterization of a micrometric grating array for an integrated multi-aperture spectrometer is presented.

2.2.1. Grating Coupler for Chip-to-Fiber Interconnects

In this section the design of a grating coupler for micrometric SOI rib waveguides, that ensures single-beam air radiation meeting the design constraints, is presented. Maximization of coupling efficiency and minimization of back-reflections are also discussed. The initial motivation of this work was the implementation of a grating coupler that could work as an input and output interface for Six-Port reflectometer devices [124] previously developed in the Photonics & RF group at the Universidad de Málaga [1]. This reflectometer, based on the micrometric rib SOI waveguides depicted in Fig. 2.14-a, is composed by a variety of multimode interference couplers (MMI) and interconnection waveguides, as schematically depicted in Fig.2.14-b. The device has one input port and one bidirectional port connected to standard SMF-28 single-mode fibers, and four output ports that can be connected to optical fibers or photodetectors. Due to the nature of the device, low reflectivity at the input and output ports is desired. The grating coupler approach, is aimed as a simple alternative to facet coupling, that provides high coupling efficiency with reduced reflections adding no extra steps to the fabrication process and avoiding the need of facet dicing, polishing and AR coating.

Device Specifications

Grating coupler should be optimized for TE polarization (electrical field parallel to the chip surface) and $1550\,\mathrm{nm}$ wavelength. In order to be compatible with the Six-Port fabrication process, the following design constraints have to be considered:

- Silicon and BOX thicknesses are respectively fixed to of $t_{Si} = 1.5\,\mu\mathrm{m}$ and $t_{BOX} = 1\,\mu\mathrm{m}$.
- Silicon dioxide or air cladding (i.e. no cladding) configurations are eligible. Air cladding is preferable to avoid interference effects the may occur in the silicon-dioxide-to-air boundary.
- Single etch step is required for the implementation of grating couplers, interconnection waveguides and MMIs composing the device.
- Maximum etch depth is set to $t_{\mathrm{Etch}} \leq 750\,\mathrm{nm}$, to ensure single-mode behavior of interconnection waveguides.
- Minimum feature size is set to $350\,\mathrm{nm}$ in order to be compatible with standard i-line stepper lithography.

Figure 2.15 shows the 2-D model used to analyze the grating. The refractive indexes of air, silicon and silicon dioxide are denoted as n_{Air}, n_{Si}, n_{SiO_2} respectively. Λ is the grating longitudinal pitch, z_{Gap} is the grating gap longitudinal length, and t_{Etch} is the gap etch depth. Silicon and BOX thicknesses are fixed to $t_{\mathrm{Si}} = 1.5\,\mu\mathrm{m}$ and

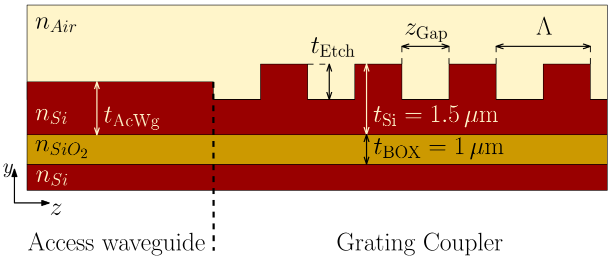

Figure 2.15.: 2-D model of proposed chip-to-fiber grating coupler.

$t_{\mathrm{BOX}} = 1\,\mu\mathrm{m}$ respectively. Access waveguide thickness t_{AcWg} is designed to optimize grating performance.

TE polarization and $1550\,\mathrm{nm}$ wavelength are assumed hereafter unless otherwise specified.

Device Particularities and Challenges

In this section intrinsic challenges of a micrometric grating coupler, compared with Si-wire gratings, are discussed in detail. Solutions proposed to overcome these limitations are qualitatively described.

Owing to the aforementioned constraints, two challenges, that hinder the implementation of single-beam radiation gratings, have to be faced in the micrometric design:

- Grating region is multimode for silicon thickness of $t_{Si} = 1.5\,\mu\mathrm{m}$.
- Minimum grating pitch for i-line stepper compatibility is $\Lambda_{min} = 700\,\mathrm{nm}$ (minimum size of $350\,\mathrm{nm}$ for gap and silicon teeth).

Interconnection waveguides width ($W_{\mathrm{Wg}} = 1.3\,\mu\mathrm{m}$) and etch depth ($t_{\mathrm{Etch}} \leq 750\,\mathrm{nm}$) are designed to meet Soref's single mode condition [125]. In the grating region, as the waveguide is substantially wider ($W_{\mathrm{Wg}} \sim 15\,\mu\mathrm{m}$), Soref' condition is not met and the waveguide is vertically (and laterally) multimode [120]. Similarly, the grating region supports several Bloch-Floquet modes. Even if an adiabatic transition between the interconnection waveguide and the grating region is implemented, ensuring that only the fundamental mode of the access waveguide is launched into the grating, higher order Bloch-Floquet modes may be excited in the waveguide-to-grating discontinuity. This way, the field in the grating region is a linear combination of the supported Bloch-Floquet modes

$$E(y,z) = \sum_i c_i \vartheta_i(y,z), \tag{2.24}$$

where c_i is the i-th Bloch-Floquet mode complex amplitude, that depends on the input field launched into the grating region. Field radiated by the grating is the weighted sum of the contribution of each mode. Therefore, the grating array factor (AF), in this case,

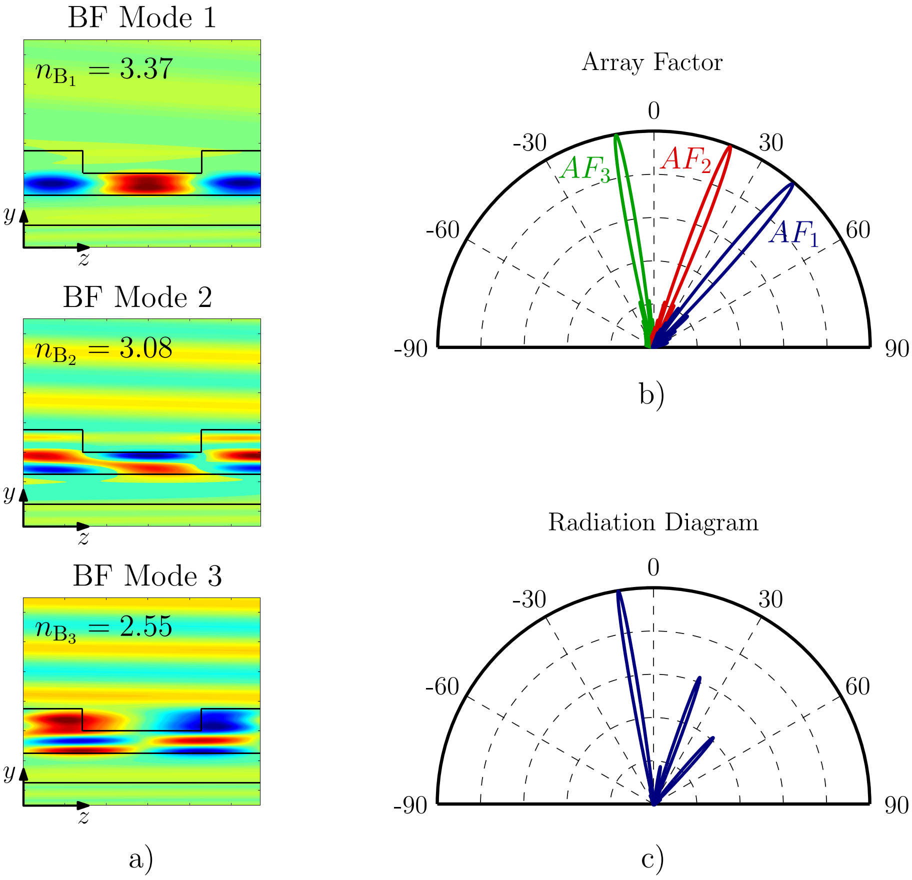

a) b) c)

Figure 2.16.: For a grating with $t_{\mathrm{Etch}} = 750\,\mathrm{nm}$, $DC = 0.5$, and a pitch $\Lambda = 570\,\mathrm{nm}$: **a)** field distribution of first three Bloch-Floquet modes, **b)** normalized array factor, and **c)** radiation pattern when the fundamental mode of an access waveguide of $t_{\mathrm{AcWg}} = 1.5\,\mu\mathrm{m}$ is launched into the proposed grating.

can be expressed as

$$\begin{aligned} AF(\theta) &= |c_1| \cdot AF_1(\theta) + |c_2| \cdot AF_2(\theta) + |c_3| \cdot AF_3(\theta) \qquad (2.25) \\ AF_1(\theta) &= \sum_{n=0}^{NP-1} e^{j\frac{2\pi}{\lambda}\Lambda n\left[n_c \sin(\theta) - n_{B_1}\right]} \\ AF_2(\theta) &= \sum_{n=0}^{NP-1} e^{j\frac{2\pi}{\lambda}\Lambda n\left[n_c \sin(\theta) - n_{B_2}\right]} \\ AF_3(\theta) &= \sum_{n=0}^{NP-1} e^{j\frac{2\pi}{\lambda}\Lambda n\left[n_c \sin(\theta) - n_{B_3}\right]}, \end{aligned}$$

where $AF_i(\theta)$ is the grating array factor of the i-th Bloch-Floquet mode (with effective index n_{B_i}), NP is the number of periods and n_c is the cladding refractive index. It is clear that, even if the single-beam radiation condition for pitch expressed in eq. (2.12) is met, there may be several radiation beams corresponding to the $k = -1$ harmonic of each Bloch-Floquet mode.

To illustrate this problem, radiation characteristics are analyzed for a grating with $t_{\mathrm{Etch}} = 750\,\mathrm{nm}$, $DC = 0.5$, and a pitch $\Lambda = 570\,\mathrm{nm}$ that meets the single-beam radiation condition in eq. (2.12). Field distribution, $\vartheta_i(y,z)$, of the first three Bloch-Floquet modes of the grating, with effective indexes of $n_{\mathrm{B}_1} = 3.37$, $n_{\mathrm{B}_2} = 3.08$, and $n_{\mathrm{B}_1} = 2.55$ are shown in Fig. 2.16-a. Grating array factor, extracted from eq. (2.25) assuming $|c_i|^2 = 1$, is represented in 2.16-b. Three radiation beams appear (with angles of $\sim$ 41°, 20°, −10°) corresponding to the $k = -1$ harmonic of the first, second and third Bloch-Floquet modes. Grating radiation diagram, when the fundamental mode of an access waveguide of $t_{\mathrm{AcWg}} = 1.5\,\mu\mathrm{m}$ is launched into the grating, is represented in Fig. 2.16-c. This access waveguide excitation produces three radiation beams with angles determined by the grating array factor and relative amplitudes related to the power coupled into each Bloch-Floquet mode. As power radiated by unwanted radiation beams is lost (propagates with a different angle and can not be properly coupled to a single-mode fiber), any grating structure exciting higher order modes will potentially result in a low coupling efficiency.

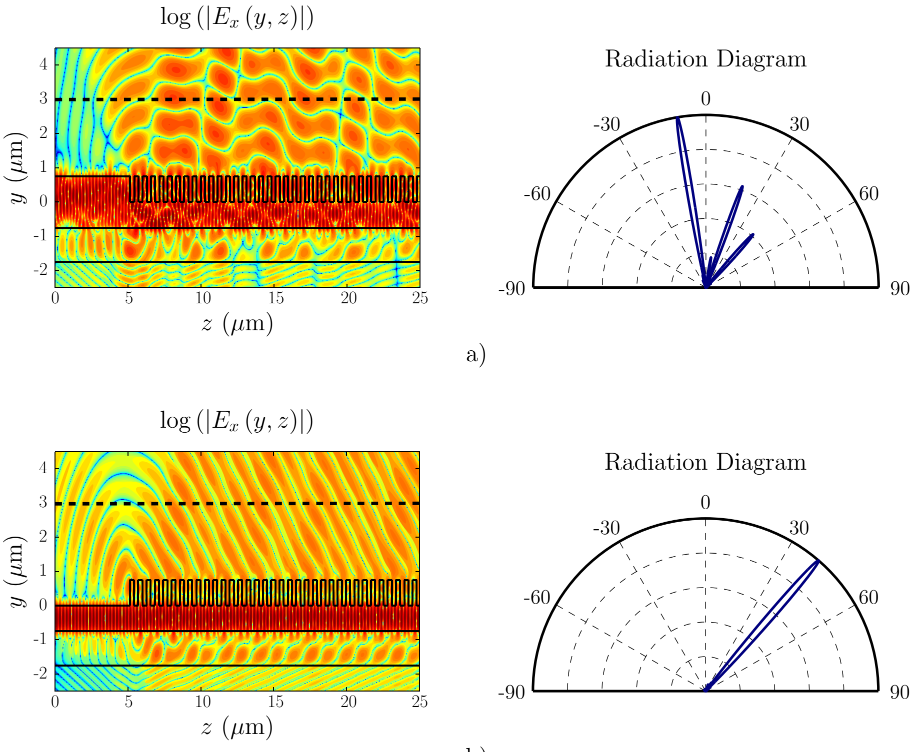

a)

b)

Figure 2.17.: Device geometry, radiated field, and calculated grating radiation diagram for a grating coupler with $t_{\mathrm{Etch}} = 750\,\mathrm{nm}$, $DC = 0.5$, $\Lambda = 570\,\mathrm{nm}$ and 40 periods with **a)** thicker access waveguide ($t_{\mathrm{AcWg}} = 1.5\,\mu\mathrm{m}$), and **b)** thinner access waveguide ($t_{\mathrm{AcWg}} = 750\,\mathrm{nm}$).

Bloch-Floquet mode excitation (and radiation characteristics) depends on the field launched into the grating. In the 2-D model used for the grating design (see Fig. 2.15), excitation field is determined by the access waveguide height (t_{AcWg}). Figure 2.17 shows device geometry, radiated field, and calculated grating radiation diagram for the same grating coupler geometry used in Fig. 2.16. A thicker, $t_{\mathrm{AcWg}} = 1.5\,\mu\mathrm{m}$, and a thinner, $t_{\mathrm{AcWg}} = 750\,\mathrm{nm}$, access waveguides are used. Grating coupler with thicker access waveguide (Fig. 2.17-a) exhibits, as mentioned before, three radiation beams that interfere producing this blurred distribution in the region above the grating. An interference pattern, typical from higher order waveguide mode excitation, can be seen in the thinner slab in the grating region, confirming the multimode behavior of the structure. Grating coupler with thinner access waveguide (Fig. 2.17-b) has a single radiation beam, corresponding to the $k = -1$ order of the fundamental Bloch-Floquet mode, exhibiting very clean plane phase fronts inside and above the grating. Design procedure has to find optimum access waveguide height that ensures single Bloch-Floquet mode excitation.

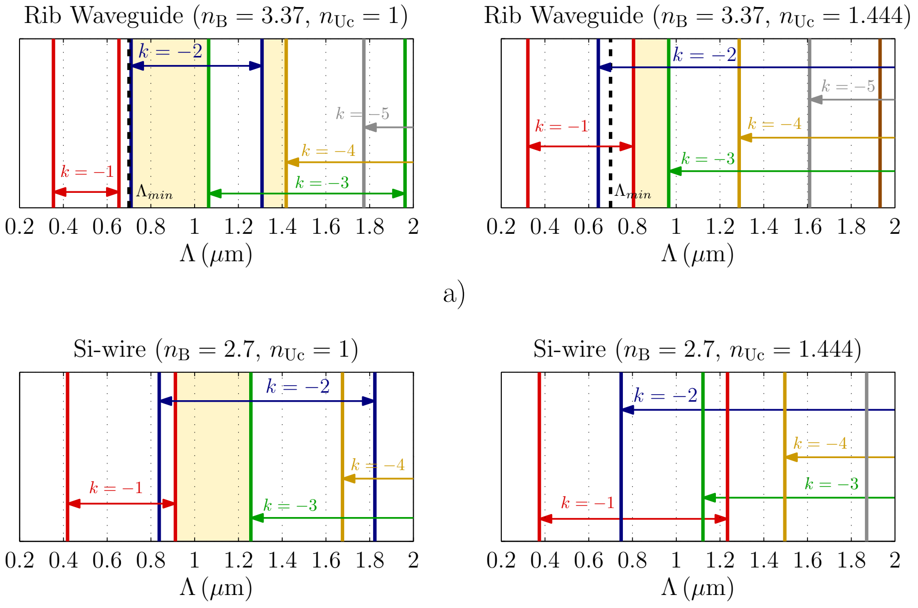

a)

b)

Figure 2.18.: Radiation condition in eq. (2.11) evaluated for different harmonic orders considering air and silicon dioxide claddings for: **a)** Bloch-Floquet effective index of $n_{\mathrm{B}} = 3.37$, corresponding to the fundamental mode of a micrometric grating and **b)** Bloch-Floquet effective index of $n_{\mathrm{B}} = 2.7$, corresponding to a Si-wire grating with $t_{\mathrm{AcWg}} = t\mathrm{Si} = 220\,\mathrm{nm}$, $t_{\mathrm{Etch}} = 70\,\mathrm{nm}$ and $n_{\mathrm{Uc}} = 1.444$. Single-beam radiation regions for higher order harmonics are shown in beige.

Due to minimum feature size constraints, even if single Bloch-Floquet mode excitation of the grating region is provided, single-beam radiation can not be provided following the conventional single $k = -1$ harmonic radiation approach, proposed by T. Tamir and S. Peng [104]. From eq. (2.12), assuming that fundamental Bloch-Floquet mode effective index is in the range between that of the thickest ($t_{\mathrm{Etch}} = 0$, $t_{\mathrm{AcWg}} = 1.5\,\mu\mathrm{m}$, $n_{\mathrm{eff}} = 3.44$) and the thinnest allowed access waveguides ($t_{\mathrm{Etch}} = 750\,\mathrm{nm}$, $t_{\mathrm{AcWg}} = 750\,\mathrm{nm}$, $n_{\mathrm{eff}} = 3.37$), and considering that $n_{\mathrm{B}_1} > n_{\mathrm{B}_2} > n_{\mathrm{B}_3}$ it can be found that for air cladding, maximum allowed pitch for single ($k = -1$) harmonic radiation is $\Lambda = 650\,\mathrm{nm}$ ($\Lambda = 640\,\mathrm{nm}$ for $\mathrm{SiO_2}$ cladding). This pitch is shorter than the minimum pitch ($\Lambda_{min} = 700\,\mathrm{nm}$) for i-line stepper compatibility. Thus, grating pitches in the single $k = -1$ radiation region are not eligible. To circumvent this limitation the use of larger pitches, that allow radiation of higher order ($k = -2, -3, ...$) harmonics, is proposed. Grating pitch is judiciously designed to provide single-beam radiation in a higher order harmonic. It is, to the best of our knowledge, the first time a higher order harmonic is used for the implementation of a grating coupler.

In order to have single harmonic radiation for the order $k = -2$, a window inside $k = -2$ radiation region should be found where adjoining harmonic orders ($k = -1$, -3) can not radiate. This single-beam $k = -2$ harmonic radiation window can only occur if maximum pitch for $k = -1$ radiation ($\Lambda_{\mathrm{Max}_{-1}}$) is shorter than minimum pitch for $k = -3$ radiation ($\Lambda_{\mathrm{Min}_{-3}}$)

$$\begin{aligned} \Lambda_{\mathrm{Max}_{-1}} &< \Lambda_{\mathrm{Min}_{-3}} \\ \frac{\lambda}{n_\mathrm{c} - n_\mathrm{B}} &< \frac{3\lambda}{n_\mathrm{c} + n_\mathrm{B}}. \end{aligned} \tag{2.26}$$

This translates to the following condition

$$n_\mathrm{B} > 2 \cdot n_\mathrm{c} \tag{2.27}$$

for the Bloch-Floquet mode effective index, n_B, and the (upper and/or bottom) cladding refractive index $n_\mathrm{c} = n_\mathrm{Uc}, n_\mathrm{Bc}$. This condition is largely fulfilled for the upper cladding in the micrometric gratings under study, with $n_\mathrm{B} = 3.44 - 3.37$ and $n_\mathrm{Uc} = 1$. Grating couplers implemented on Si-wires typically have a lower Bloch-Floquet effective index, ($n_\mathrm{B} \sim 2.7$), that hinders the opening of higher order single-beam radiation windows. In Fig. 2.18, radiation condition in eq. (2.11) is evaluated for different harmonic orders considering air and silicon dioxide claddings for: i) Bloch-Floquet effective index of $n_\mathrm{B} = 3.37$, corresponding to the fundamental mode of a micrometric grating (Fig. 2.18-a), ii) Bloch-Floquet effective index of $n_\mathrm{B} = 2.7$, corresponding to a Si-wire grating with (Fig. 2.18-b). Higher order single-beam radiation windows appear in the micrometric grating case, beige regions in Fig. 2.18-a, for pitches meeting i-line stepper compatibility restriction ($\Lambda > 700\,\mathrm{nm}$) regardless the considered cladding. In the Si-wire case, single-beam higher order radiation can only be achieved if air cladding is used.

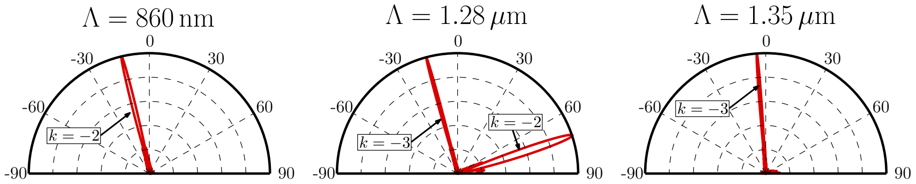

a) b) c)

Figure 2.19.: Normalized grating array factor for $n_\mathrm{B} = 3.37$, $n_\mathrm{Uc} = 1$, 40 periods and pitches of **a)** $\Lambda = 860\,\mathrm{nm}$, **b)** $1.28\,\mu\mathrm{m}$, and **c)** $1.35\,\mu\mathrm{m}$.

As an example, grating array factors for $n_\mathrm{B} = 3.37$, $n_\mathrm{Uc} = 1$ and pitches of $\Lambda = 860\,\mathrm{nm}$, $1.28\,\mu\mathrm{m}$, $1.35\,\mu\mathrm{m}$ are represented in Figs. 2.19-a, 2.19-b and 2.19-c. As expected, grating couplers with pitches of $\Lambda = 860\,\mathrm{nm}$ and $\Lambda = 1.35\,\mu\mathrm{m}$ (inside the single-beam region for $k = -2$ and $k = -3$ respectively) exhibit a unique radiation beam, whereas the grating with $\Lambda = 1.28\,\mu\text{m}$ (outside the single-beam region) has two radiation beams.

Design procedure should find higher order single-beam radiation windows for the structures under study.

Grating Coupler Design

In this section, conditions for single Bloch-Floquet mode excitation of the grating region are derived. Optimum grating dimensions (etch depth, pitch and duty cycle) compatible with fabrication process ensuring single-beam (higher order) radiation are also presented that maximize fiber coupling efficiency minimizing back-reflections.

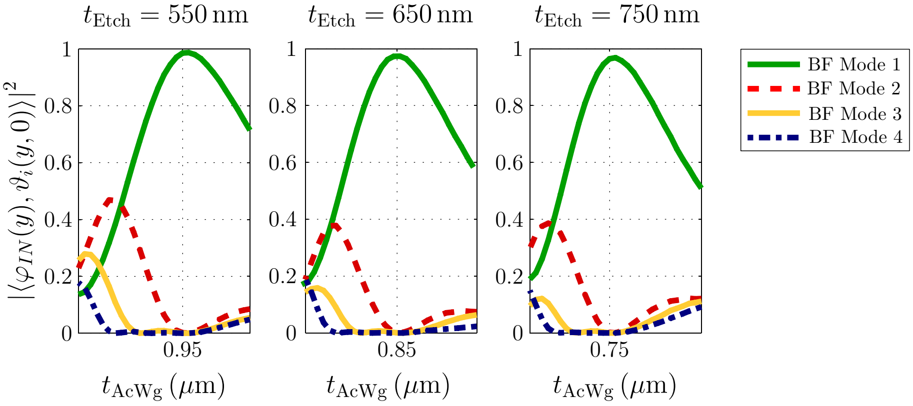

Figure 2.20.: Overlap integral in eq. (2.28) between access waveguide fundamental mode and Bloch-Floquet modes in the grating region as a function of the access waveguide height (t_{AccWg}) for three different grating gap etch depths ($t_{\text{Etch}} = 550\,\text{nm}$, $650\,\text{nm}$ and $750\,\text{nm}$).

The coupling to a specific Bloch-Floquet mode is proportional to the matching between the excitation field and the mode profile. This field matching is represented by the following overlap integral:

$$\langle\varphi_{IN}(y), \vartheta_i(y,0)\rangle = \int \varphi_{IN}(y) \cdot \vartheta_i^*(y,0)\,\mathrm{d}y, \tag{2.28}$$

where the excitation field $\varphi_{IN}(y)$ corresponds to the fundamental mode of the access waveguide in Fig. 2.15 and depends on its thickness (t_{AcWg}).

Single-mode excitation of the grating is achieved when the following condition is satisfied [61]

$$\langle\varphi_{IN}(y), \vartheta_i(y,0)\rangle \approx 0 \,\text{for}\, i \neq 1. \tag{2.29}$$

Field matching, defined in eq. (2.28), is evaluated, and represented in Fig. 2.20, as a function of the t_{AcWg} for three different etch depths ($t_{\text{Etch}} = 550\,\mu\text{m}$, $650\,\mu\text{m}$, $750\,\mu\text{m}$) in the allowed range (ensure single-mode behavior of interconnection waveguides). It is found that there is an optimum access waveguide thickness, related to the etch depth as

$$t_{\text{AcWg}}^{Opt} \sim t_{\text{Si}} - t_{\text{Etch}}, \tag{2.30}$$

that ensures single-mode excitation of the grating region. It has been verified that condition (2.30) remains valid for a broad range of wavelengths, etch depths, grating pitches and duty cycles. The use of an inverse taper to adiabatically transite between the interconnection waveguide and the optimized excitation is discussed in the following section.

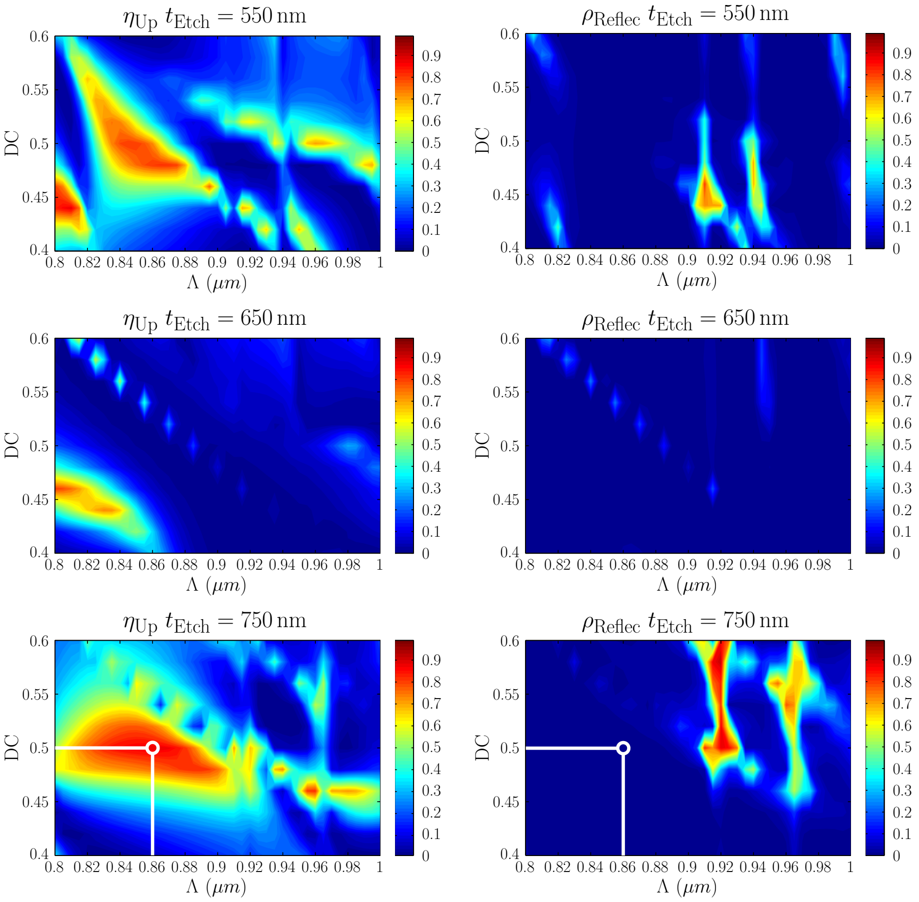

a) b)

Figure 2.21.: **a)** Grating directionality (η_{Up}) and **b)** reflection coefficient (ρ_{Reflec}) as a function of grating pitch (Λ) and duty cycle DC for 40 periods and three different etch depths ($t_{\mathrm{Etch}} = 550\,\mathrm{nm}$, $650\,\mathrm{nm}$ and $750\,\mathrm{nm}$), calculated with our Fourier-expansion based in-house tool [126] when the fundamental mode of the optimized access waveguide ($t_{\mathrm{AccWg}} = t_{\mathrm{Si}} - t_{\mathrm{Etch}}$) is launched into the grating.

Once conditions for single-mode excitation have been set, fiber coupling efficiency optimization is discussed. Fiber coupling efficiency is determined, as discussed in section 2.1.3, by the grating reflection coefficient (ρ_{Reflec}), directionality (η_{Up}), and matching between the radiated field and the fundamental mode of the fiber (η_{OL}), as expressed in eq. (2.17), repeated here for clarity

$$CE = \frac{P_{\mathrm{Fiber}}}{P_{\mathrm{Inc}}} = (1 - \rho_{\mathrm{Reflec}}) \cdot \eta_{\mathrm{Up}} \cdot \eta_{\mathrm{OL}}. \tag{2.31}$$

First, grating reflection coefficient and directionality, are studied for different grating geometries to find regions of interest (minimize ρ_{Reflec} and maximize η_{Up}). Then, coupling to fiber is analyzed for gratings within those regions to find optimum design. Optimized access waveguide height ($t_{\text{AcWg}}^{Opt} = t_{\text{Si}} - t_{\text{Etch}}$) is used at the input. Only grating geometries that ensure single ($k = -2$ or $k = -3$) harmonic radiation meeting minimum pitch ($\Lambda > 700\,\text{nm}$) for i-line stepper compatibility are considered.

Grating directionality and reflection coefficient are calculated, using our Fourier expansion based in-house tool [126], when the fundamental mode of the optimized access waveguide is launched into the grating. Figure 2.21 shows calculated η_{Up} and ρ_{Reflec} results as a function of pitch and duty cycle for three different etch depths ($t_{\text{Etch}} = 550\,\text{nm}$, $650\,\text{nm}$, $750\,\text{nm}$). Optimum dimensions (white point in Fig. 2.21) are found to be $t_{\text{Etch}} = 750\,\text{nm}$, $\Lambda = 860\,\text{nm}$, $DC = 0.5$ and 40 periods. The optimized grating exhibits a remarkable directionality of $\eta_{\text{Up}} \sim 0.9$ with back-reflections as low as $P_{Reflec} \sim -27\,\text{dB}$. Radiation angle, $\theta_k = -13.4°$, corresponds to the $k = -2$ harmonic. Proposed device shows relatively large tolerances to grating pitch and duty cycle (see Fig. 2.21). Dependence on etch depth and wavelength are represented in Figs. 2.22-a and 2.22-b. $\eta_{\text{Up}} > 0.8$ is ensured in the range of $(-15\,\text{nm},\ 50\,\text{nm})$ variations in etch depth. Nominal device exhibits $P_{up} > 0.8$ in a $30\,\text{nm}$ bandwidth. Reflections below $-17\,\text{dB}$ are ensured in the analyzed ranges.

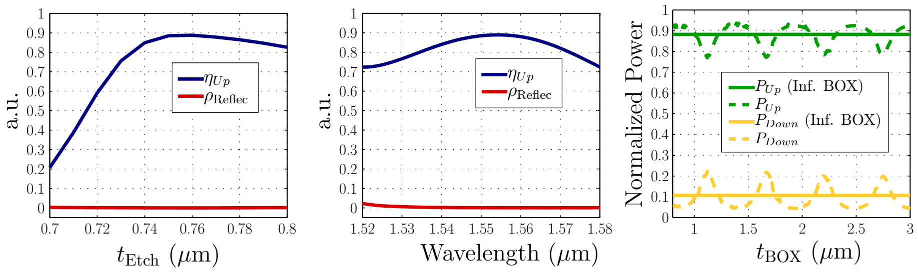

a) b) c)

Figure 2.22.: Grating directionality (η_{Up}) and reflection coefficient (ρ_{Reflec}) for proposed grating with optimized access waveguide ($t_{\text{AccWg}} = t_{\text{Si}} - t_{\text{Etch}}$) and 40 periods as a function of **a)** etch depth (t_{Etch}) and **b)** wavelength. **c)** Power radiated up (P_{Up}) and down (P_{Down}) as a function of BOX thickness (t_{BOX}) compared with the infinite BOX thickness case.

Reduced back-reflections are provided by the combination of i) a very good matching between the access waveguide and the grating fundamental mode (due to optimized access waveguide thickness) and ii) a grating pitch ($\Lambda = 860\,\text{nm}$ and radiation angle $\theta = -13.4°$) far from the Bragg region that avoids Bragg reflections.

High directionality is provided by the intrinsic grating coupler characteristics, with a negligible contribution of the BOX-to-substrate discontinuity. The proposed grating with an infinite BOX thickness shows a directionality of $\eta_{\text{Up}} \sim 0.9$. Power radiated to the air (P_{Up}) and substrate (P_{Down}) are analyzed in Fig. 2.22-c as a function of the BOX thickness and compared with the infinite BOX thickness case. Device is very robust to BOX thickness, with power variations of $\pm 5\,\%$ in the analyzed range.

Finally, coupling efficiency to standard single-mode fiber SMF-28 of the proposed grating coupler is analyzed. In order to quantify the effect of the grating excitation on

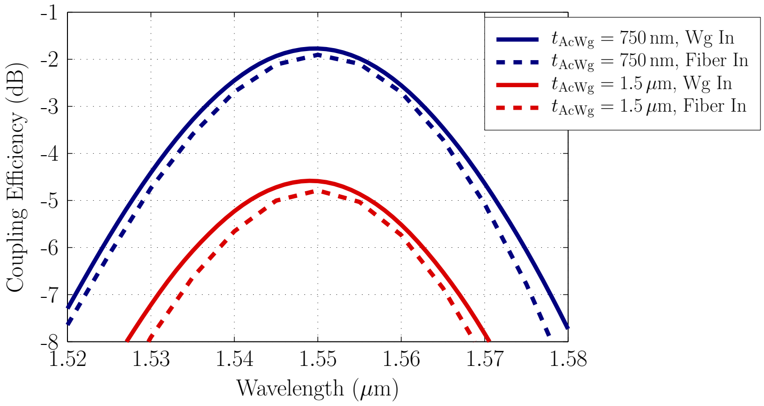

Figure 2.23.: Coupling efficiency of the proposed grating coupler ($t_{\mathrm{Etch}} = 750\,\mathrm{nm}$, $\Lambda = 860\,\mathrm{nm}$, $DC = 0.5$ and 40 periods) for access waveguide with optimized $t_{\mathrm{AcWg}} = 750\,\mathrm{nm}$ (blue lines) and conventional $t_{\mathrm{AcWg}} = 1.5\,\mu\mathrm{m}$ (red lines) thicknesses when i) fundamental mode of the access waveguide is launched into the grating and coupling to the fundamental mode of the fiber is calculated using our Fourier-expansion based in-house tool [126] (solid lines), and ii) fundamental mode of the fiber is launched into the grating and coupling to the fundamental mode of the access waveguide is calculated using FDTD commercial tool RSoft (dashed lines).

the coupling efficiency, two access waveguide thicknesses are considered: i) optimized (single-mode excitation) $t_{\mathrm{AcWg}} = 750\,\mathrm{nm}$, and ii) conventional $t_{\mathrm{AcWg}} = 1.5\,\mu\mathrm{m}$. In order to double-check results, two simulation scenarios are considered:

- Fundamental mode of the access waveguide is launched into the grating and coupling to the fundamental mode of the fiber is calculated using our Fourier-expansion based in-house tool [126].
- Fundamental mode of the fiber is launched into the grating and coupling to the fundamental mode of the access waveguide is calculated using commercial Finite Difference Time Domain (FDTD) tool (RSoft, FullWave).

Results are presented in Fig. 2.23, showing a very good agreement between both simulation scenarios ($0.2\,\mathrm{dB}$ peak coupling efficiency difference). Grating with optimized access waveguide height exhibits a $CE \sim -1.9\,\mathrm{dB}$ (worst case simulation) with a $3\,\mathrm{dB}$ bandwidth of $40\,\mathrm{nm}$, whereas peak coupling efficiency for the conventional access waveguide is $CE \sim -4.8\,\mathrm{dB}$. These results show that single Bloch-Floquet mode excitation (provided by an optimized access waveguide) of the grating coupler substantially improves coupling efficiency.

Excitation Stage Design

The excitation stage has to efficiently couple the fundamental mode of the interconnection waveguide (shown in Fig. 2.24-a) to the optimum excitation field (shown in Fig. 2.24-b), and vice versa. The use of an inverse taper as excitation stage of the grating coupler is discussed below.

An optimum excitation field, $E_{in}^{Opt}(x,y) = E_{in_x}^{Opt}(x) \cdot E_{in_y}^{Opt}(y)$, is defined that has:

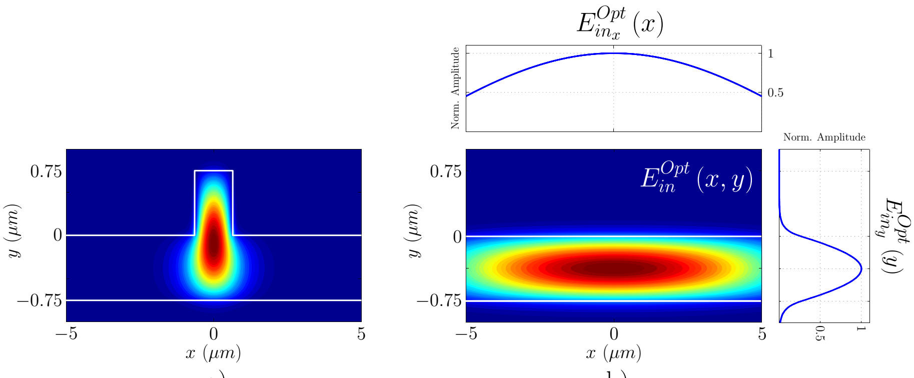

a) b)

Figure 2.24.: Electrical field distribution in the $x - y$ plane of **a)** fundamental mode of interconnection rib waveguide, **b)** optimum excitation field for the proposed grating coupler design composed by i) the fundamental mode of a thinner slab of $t_{\mathrm{Si}} - t_{\mathrm{Etch}} = 750\,\mathrm{nm}$ thickness in the y-axis and ii) the fundamental mode of a $15\,\mu\mathrm{m}$ wide slab in the x-axis.

- Field distribution along the y-axis, $E^{Opt}_{in_y}(y)$, that ensures single-mode excitation of the grating region. According to the criteria defined in previous section, $E^{Opt}_{in_y}(y)$ is the fundamental mode of a waveguide of thickness $t^{Opt}_{\mathrm{Acwg}} = t_{\mathrm{Si}} - t_{\mathrm{Etch}}$.
- Field distribution along the x-axis, $E^{Opt}_{in_x}(x)$, that maximizes in-plane matching with optical fiber fundamental mode. $E^{Opt}_{in_x}(x)$ is the fundamental mode of the access waveguide whose width is designed to optimize overlap with the mode of the optical fiber [103].

Optimum excitation field for the proposed grating coupler design (see Fig. 2.24-b) is composed by i) the fundamental mode of a thinner slab of $t_{\mathrm{Si}} - t_{\mathrm{Etch}} = 750\,\mathrm{nm}$ thickness in the y-axis and ii) the fundamental mode of a $15\,\mu\mathrm{m}$ wide slab in the x-axis.

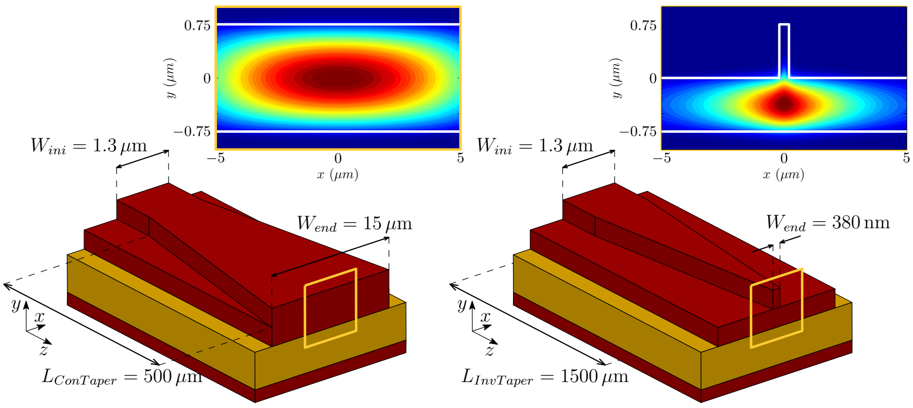

a) b)

Figure 2.25.: Schematic 3-D geometry and field profile at the end of **a)** conventional direct taper, and **b)** inverse taper.

The conventional taper approach, depicted in Fig. 2.25-a, is not the proper solution for this device. While the desired field distribution in the x-axis dimension is provided, there is a large mismatch in the y-axis dimension as the field at the end of the taper is confined in the thicker slab of thickness $t_{\mathrm{Si}} = 1.5\,\mu\mathrm{m}$. This mismatch would result in large back-reflections ($-5\,\mathrm{dB}$) and excitation of unwanted higher order modes in the grating region. To circumvent this problem, the use of an inverse taper, depicted in Fig. 2.25-b, is proposed that pushes the rib waveguide mode down to the thinner $750\,\mathrm{nm}$ slab and expands it in the x dimension, providing very good matching with the optimum excitation field in the $x - y$ plane.

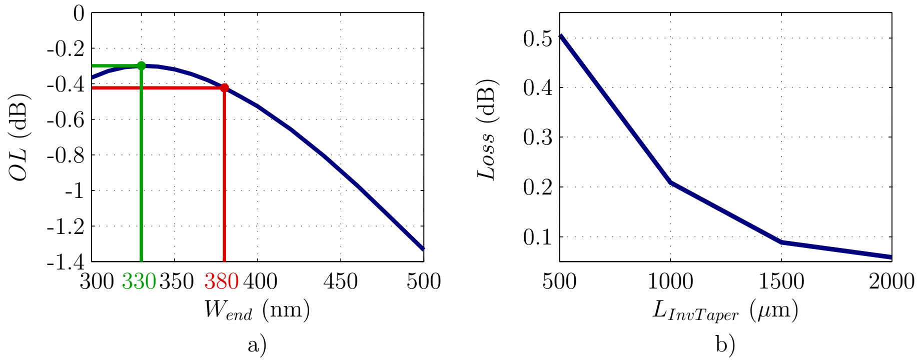

Figure 2.26.: a) Overlap between optimum excitation field and field at the end of the taper as a function of the end tip width (W_{end}). **b)** Taper loss as a function of its length ($L_{InvTaper}$).

Overlap between the optimum excitation field (Fig. 2.24-b) and the field at the end of the taper (Fig. 2.25-b) is represented in Fig. 2.26-a as a function of taper end tip width W_{end}. Field matching is maximized for an end tip of $W_{end} = 330\,\mathrm{nm}$ ($OL = -0.3\,\mathrm{dB}$). Figure 2.26-b shows the loss of the taper as a function of its length ($L_{InvTaper}$). Insertion losses below $0.1\,\mathrm{dB}$ are obtained for a taper length of $L_{InvTaper} = 1500\,\mu\mathrm{m}$.

Note that the inverse taper has to be longer than the conventional taper (typically $L_{ConvTaper} = 500\,\mu\mathrm{m}$), because it does not only laterally expand the field but also transforms it in the vertical (y) direction, whereas the mode transformation the vertical dimension in the conventional taper is minimal.

Due to fabrication constraints minimum end tip is set to $W_{end} = 380\,\mathrm{nm}$. The use of this suboptimal tip width produces a $0.1\,\mathrm{dB}$ penalty in the overlap with optimum excitation field (see Fig. 2.26-a).

Experimental Results

In this section the experimental characterization of the proposed grating coupler is discussed.

Identical grating couplers with conventional (Fig. 2.27-a) and inverse (Fig. 2.27-b) tapers are characterized in order to experimentally verify the impact of the excitation stage. Variations from the optimized pitch and gap dimensions are included to compensate typical fabrication tolerances. The devices were fabricated using i-line stepper lithography and reactive ion etching at the Canadian Photonic Fabrication Center

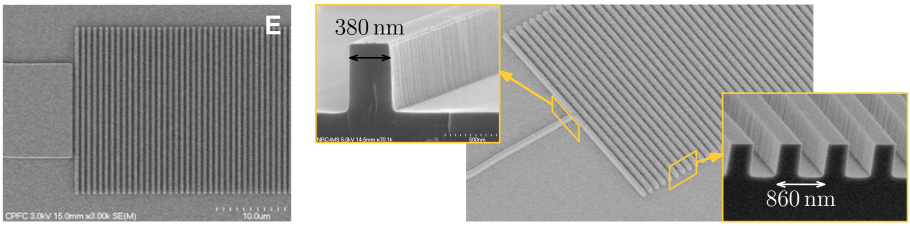

a) b)

Figure 2.27.: Scanning electron microscope image of the fabricated chip-to-fiber grating coupler with excitation stage based on **a)** conventional direct taper, and **b)** proposed inverse taper.

(CPFC).

Geometrical parameters (see Fig. 2.25) of fabricated excitation stages are:

- Conventional taper: initial width of $W_{ini} = 1.3\,\mu\text{m}$, final width $W_{end} = 15\,\mu\text{m}$ and taper length of $L_{ConvTaper} = 500\,\mu\text{m}$. Simulated insertion loss < 0.1 dB.
- Inverse taper: initial width of $W_{ini} = 1.3\,\mu\text{m}$, final width $W_{end} = 380\,\text{nm}$ and taper length of $L_{InvTaper} = 1500\,\mu\text{m}$. Simulated insertion loss < 0.1 dB.

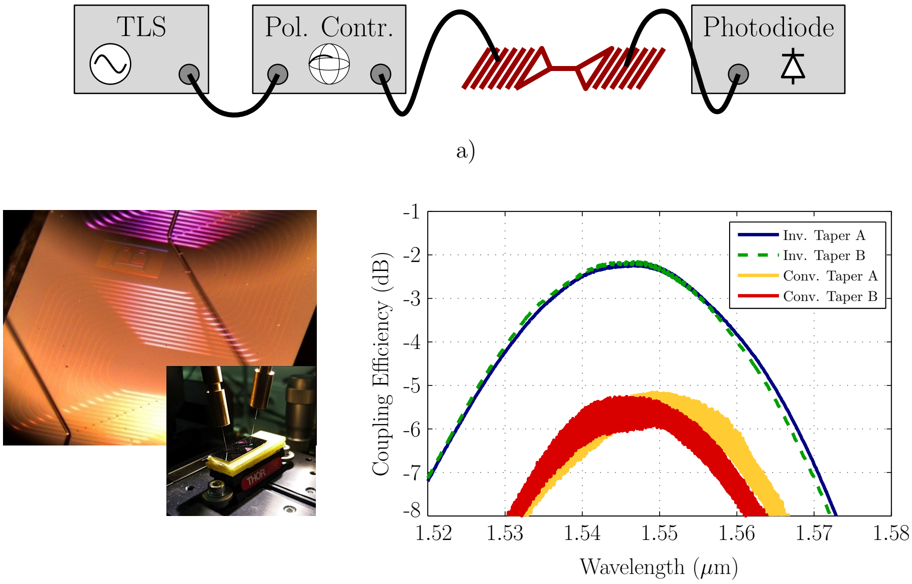

a)

b) c)

Figure 2.28.: Measurement setup for characterization of back-to-back grating couplers is shown in **a)** and **b)**. **c)** Experimental coupling efficiency for two different realizations of grating couplers with inverse and direct tapers.

Two nominally identical couplers are arranged together in a back-to-back configuration, light being injected to chip with one grating and extracted with the other (see Fig. 2.28-a and 2.28-b). Light coming from a tunable laser source (TLS) is coupled to the chip using a cleaved single mode fiber (SMF-28). A polarization controller is used to set transverse electric (TE) polarization (electric field parallel to the chip plane). Light diffracted by the output grating is collected using a cleaved SMF-28 fiber and injected to an InGaAs photodetector. Coupling efficiency of one grating coupler is obtained from power measured in the photodetector, subtracting setup loss (polarization optics, optical fiber patchcords and photodetector) and interconnection waveguide propagation loss, and dividing by two. Setup loss of $P_{\mathrm{setup}} = -3.7\,\mathrm{dB}$ at $1550\,\mathrm{nm}$ is estimated from the power at the InGaAs photodetector when the input and output fibers are butt-coupled (without the chip). An interconnection waveguide loss of $2.5\,\mathrm{dB/cm}$, mainly due to scattering on the sidewall roughness, is determined in an independent measurement using the minimum phase technique [127].

Measured coupling efficiency is represented in Fig. 2.28-c for two different couples of grating couplers with conventional and inverse tapers, showing a very good agreement with the simulation results (see Fig. 2.23). Gratings with optimized inverse taper exhibit a measured peak coupling efficiency of $-2.2\,\mathrm{dB}$ with a $3\,\mathrm{dB}$ bandwidth of $40\,\mathrm{nm}$, that improves state of the art non-apodized single-etch Si-wire grating couplers without bottom reflectors. This is a $3.3\,\mathrm{dB}$, improvement compared to grating couplers with conventional taper ($-5.5\,\mathrm{dB}$ coupling efficiency). The effect of reduced back-reflections in the inverse taper case compared with the conventional one can be clearly seen in the amplitude of the Fabry-Perot ripple. Back reflections of 8% are estimated, using the minimum phase technique, for the conventional taper, which is a ten-fold penalty compared to the inverse taper. A slight blue shift deviation ($\sim 5\,\mathrm{nm}$) of the peak coupling efficiency from the design wavelength can be attributed to the reduction of effective index of the fundamental Bloch mode produced by some overetching.

These results, demonstrate for the first time that grating couplers implemented on micrometric rib waveguides can exhibit comparable or even superior performance to Si-wire based ones.

2.2.2. Polarization Independent Grating Coupler

Grating couplers implemented on Si-wires are, in principle, highly polarization sensitive. Large birefringence in a Si-wire based grating coupler ($\Delta n_{\mathrm{B}} = \left|n_{\mathrm{B}}^{\mathrm{TE}} - n_{\mathrm{B}}^{\mathrm{TM}}\right| \sim 0.8$) produces a large difference in optimum radiation angle for TE and TM ($\Delta\theta = \left|\theta^{\mathrm{TE}} - \theta^{\mathrm{TM}}\right| > 30^{\circ}$). Thus, most of the devices found in literature are designed to couple only one (TE or TM) polarization. Different approaches have been proposed, that benefit from this large birefringence, to implement grating couplers that behave as polarization splitters [25,36,41]. In order to have polarization independent performance, Δn_{B} needs to be reduced. Whereas in typical Si-wires $n_{\mathrm{B}}^{\mathrm{TE}} \gg n_{\mathrm{B}}^{\mathrm{TM}}$, transversal swg structures can be designed to have the opposite behavior $n_{\mathrm{B}}^{\mathrm{TE}} \ll n_{\mathrm{B}}^{\mathrm{TM}}$ [128]. Based on this approach, polarization independent coupling efficiency of $-1.9\,\mathrm{dB}$ has been theoretically shown [35]. Please refer to section 2.1.3 for details on state of the art of polarization management in grating couplers.

Due to the lower birefringence of gratings implemented on micrometric rib SOI waveguides ($\Delta n_{\mathrm{B}} \sim 0.1$ and $\Delta\theta \sim 5^{\circ}$), polarization independent behavior can be achieved obviating the need of swg structures, that would have dimensions non compatible with standard fabrication processes (minimum feature size of $350\,\mathrm{nm}$).

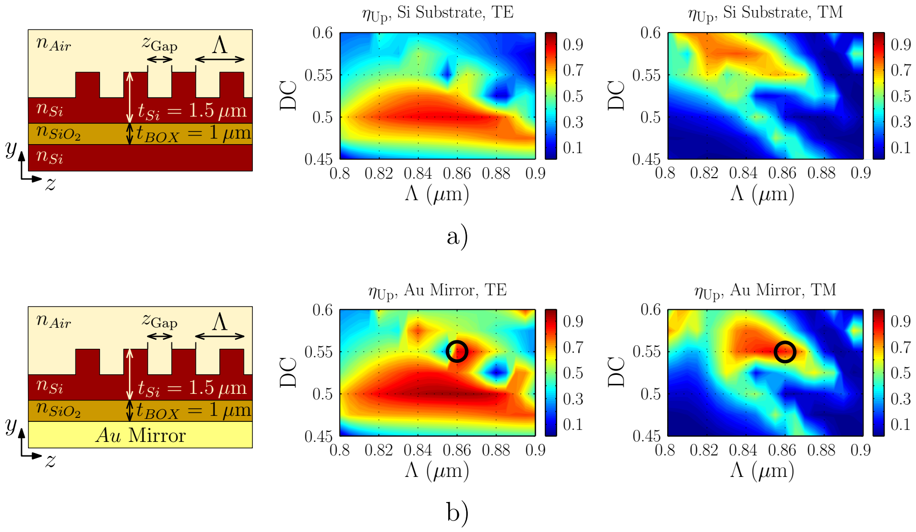

Figure 2.29.: Grating geometry and directionality (η_{Up}) for TE and TM polarizations as a function of grating pitch (Λ) and duty cycle DC for 40 periods, and etch depth $t_{\mathrm{Etch}} = 750\,\mathrm{nm}$ for $1.55\,\mu\mathrm{m}$ wavelength. Gratings with **a)** silicon substrate and **b)** gold bottom mirror are considered. η_{Up} is calculated with our Fourier-expansion based in-house tool [126] when the fundamental mode of the optimized access waveguide ($t_{\mathrm{AccWg}} = 750\,\mathrm{nm}$) is launched into the grating.

In this section, the implementation of a polarization independent grating for micrometric SOI rib waveguides is theoretically discussed. The design approach presented in section 2.2.1 is extended to a dual polarization configuration.

Device Specifications

Grating coupler should be optimized for TE and TM polarizations at $1550\,\mathrm{nm}$ wavelength. The following geometric parameters are set in order to be compatible with the design presented in section 2.2.1

- Silicon and BOX thicknesses are respectively fixed to $t_{Si} = 1.5\,\mu\mathrm{m}$ and $t_{BOX} = 1\,\mu\mathrm{m}$.
- Air cladding
- Etch depth is set to $t_{\mathrm{Etch}} = 750\,\mathrm{nm}$.
- Minimum feature size is set to $350\,\mathrm{nm}$ in order to be compatible with standard i-line stepper lithography.

Grating Coupler Design

Directionality is analyzed as a function of the grating pitch (Λ) and duty cycle (DC), when the fundamental mode of the access waveguide ($t_{\mathrm{AcWg}} = 750\,\mathrm{nm}$) is launched into the grating. Only designs that provide single $k = -2$ order radiation are considered. Figure 2.29-a shows η_{Up} for TE and TM polarizations. Despite grating low birefringence ($\Delta n_{\mathrm{B}} \sim 0.1$) directionality performance is strongly polarization dependent. Unfortunately, no combination of pitch and duty cycle can be found where both polarizations exhibit $\eta_{Up} > 0.6$. To circumvent this directionality limitation the use of a bottom mirror is proposed. In order to maximize directionality, field radiated down and reflected in the bottom mirror and field (directly) radiated up need to interfere constructively [26]. Typically, grating geometry is fixed and mirror position is optimized to provide required path length difference [26, 33, 116]. In the proposed design, mirror position is fixed, and grating pitch and duty cycle (and thus radiation angle) are changed to maximize directionality (constructive interference). This way, the bottom mirror can be implemented by a thin gold layer deposited just underneath the $1\,\mu$m BOX (see schematic representation in Fig. 2.29-b). SiO_2 can be used as an etch stop layer for the selective removal process of the Si substrate [129], simplifying the fabrication process and avoiding the problem of etch depth tolerances.

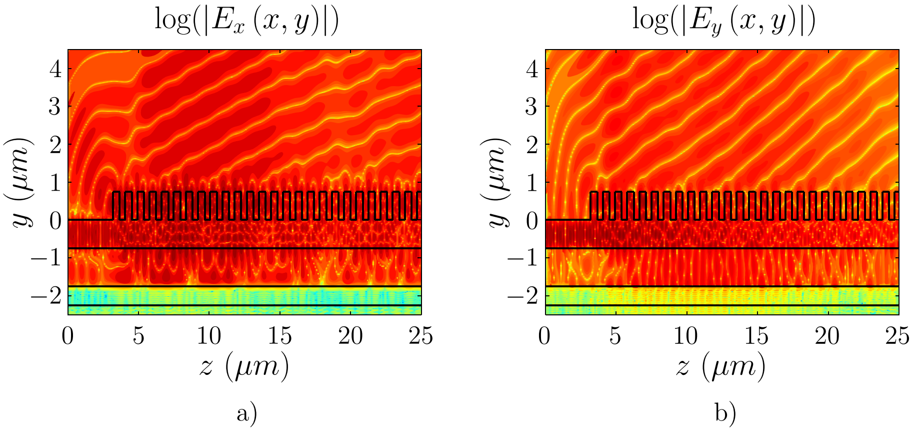

Figure 2.30.: Device geometry and radiated field for a grating coupler with $t_{\mathrm{Etch}} = 750\,\mathrm{nm}$, $DC = 0.55$, $\Lambda = 860\,\mathrm{nm}$, 40 periods and gold bottom mirror when the fundamental **a)** TE or **b)** TM mode of the access waveguide ($t_{\mathrm{AcWg}} = 750\,\mathrm{nm}$) at $1.55\,\mu$m wavelength is launched into the grating.

Directionality is analyzed as a function of the grating pitch and duty cycle, considering a bottom metal mirror. Results are presented in Fig. 2.29-b. Directionality better than $\eta_{\mathrm{Up}} > 0.84$ can be achieved for both TE and TM polarizations for a grating with $\Lambda = 860\,\mathrm{nm}$ and $DC = 0.55$ (black circle in Fig. 2.29-b). Field radiation for the optimized design is presented in Fig. 2.30 for TE and TM polarizations.

Coupling efficiency is analyzed for the proposed design. Coupling to the fundamental (TE, TM) mode of the access waveguide when the fundamental (TE, TM) mode of the optical fiber is launched into the grating is calculated using commercial FDTD tool RSoft FullWave. Calculated CE as a function of the fiber angle (θ_{IF}, defined from the vertical axis as depicted in Fig. 2.31) for the proposed grating coupler with and without bottom mirror is shown in Fig. 2.31. The use of a bottom mirror substantially increases directionality for the TE polarization enabling high CE for both polarizations at the same time. Directionality for the TM polarization was already very high for the Si substrate

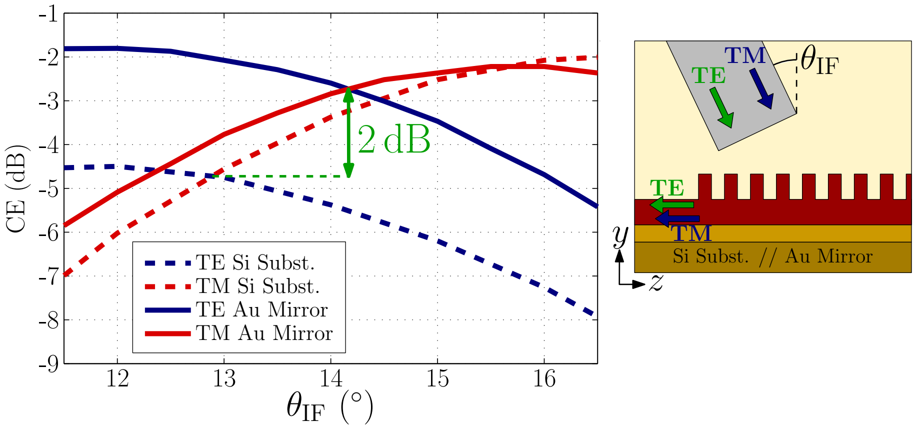

Figure 2.31.: Coupling to the fundamental mode of the access waveguide when the fundamental mode of the optical fiber is launched into the proposed grating with $t_{\mathrm{Etch}} = 750\,\mathrm{nm}$, $DC = 0.55$, $\Lambda = 860\,\mathrm{nm}$ and 40 periods considering silicon substrate (dashed lines) and gold bottom mirror (solid lines). CE is calculated for TE (blue lines) and TM (red lines) using commercial FDTD tool RSoft FullWave.

grating, hence the mirror effect is minimal. It can be seen that, although optimum fiber angle is different for TE ($\theta^{\mathrm{TE}} = 11.5°$) and TM ($\theta^{\mathrm{TM}} = 16.5°$) polarizations, when the a bottom mirror is used and fiber is placed at an angle

$$\theta_{\mathrm{IF}} \sim \frac{\theta^{\mathrm{TE}} + \theta^{\mathrm{TM}}}{2} \tag{2.32}$$

dual-polarization coupling efficiency better than $CE = -3\,\mathrm{dB}$ can be achieved.

2.2.3. Grating Coupler for Integrated Spectrometer

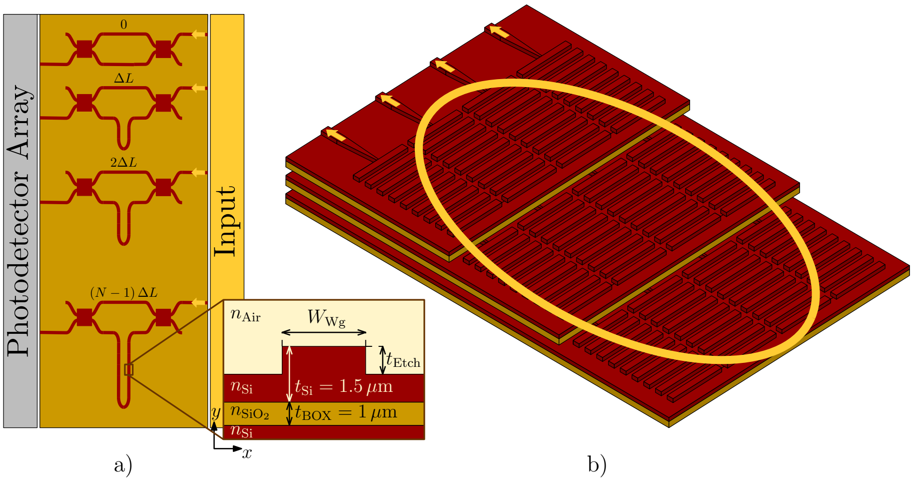

a) b)

Figure 2.32.: Schematic representation of **a)** integrated multi-aperture Fourier-transform scpetrometer, and **b)** 2-D grating array for increased throughput.

In this section the design and experimental characterization of an efficient input interface for an integrated multi-aperture Fourier-transform spectrometer (FTS) is presented. The FTS is developed in the frame of a collaborative project between the National Research Council Canada, the company ComDev and the Canadian Space Agency, and aims to monitor water vapor absorption in the atmosphere from an Earth satellite [71,72]. The FTS (see Fig. 2.32-a) uses a variety of inputs, arranged in a 1-D array, each feeding one Mach-Zehnder interferometer. This configuration substantially increases optical throughput (*étendue*) compared to single aperture spectrometers [122]. In order to further increase the *étendue* of the FTS, the use of a 2-D grating array, as the one shown in Fig. 2.32-b, that can potentially provide $100\,\%$ fill factor of the focal plane is proposed.

The FTS uses $1.5\,\mu\mathrm{m}$ thick SOI rib waveguides (see Fig. 2.32-a). Therefore the design approach proposed in section 2.2.1 is used to optimize grating dimensions. Note that, in this case, the input field is a windowed plane wave (and not the fundamental mode of an optical fiber). Design criteria are developed for this plane-wave-to-grating problem optimization. Device design and experimental characterization are discussed below.

Device Specifications

Grating coupler should be optimized for TE polarization (electrical field parallel to the chip surface) and $1364\,\mathrm{nm}$ (peak water absorption) wavelength. In order to be compatible with the FTS fabrication process, the following design constraints have to be considered:

- Silicon and BOX thicknesses are respectively fixed to of $t_{Si} = 1.5\,\mu\mathrm{m}$ and $t_{BOX} = 1\,\mu\mathrm{m}$.
- Silicon dioxide or air cladding (i.e. no cladding) configurations are eligible. Air cladding is preferable to avoid interference effects the may occur in the silicon-dioxide-to-air boundary.
- Single etch step is required, for the implementation of grating couplers, interconnection waveguides and MMIs composing the device.
- Etch depth is fixed to $t_{\mathrm{Etch}} = 750\,\mathrm{nm}$.
- Minimum feature size is set to $350\,\mathrm{nm}$ in order to be compatible with standard i-line stepper lithography.

Design and Experimental Characterization

Directionality is analyzed to find optimum grating dimensions. Access waveguide height is set to $t_{\mathrm{AcWg}} = 750\,\mathrm{nm}$, to ensure single-mode excitation of the grating. Only combinations of pitch (Λ) and duty cycle (DC) that provide single $k = -2$ order radiation are considered. Calculated directionality is shown in Fig. 2.33. It can be seen that $\eta_{\mathrm{Up}} > 0.8$ can be achieved for a variety of grating pitches and duty cycles. Pitch and duty cycle of $\Lambda = 740\,\mu\mathrm{m}$ and $DC = 0.5$ (black circle in Fig. 2.33) are chosen as the proposed design, as they provide $\eta_{\mathrm{Up}} > 0.83$ with a suitable radiation angle of $\theta_{-2} = -15.8°$. Note that the required grating length to radiate all the power is substantially larger at

$1364\,\mathrm{nm}$ wavelength ($>\ 120\,\mu\mathrm{m}$) than at $1550\,\mathrm{nm}$ ($>\ 30\,\mu\mathrm{m}$). Nevertheless, as the window size is a design parameter, it can be fit to the optimum grating length.

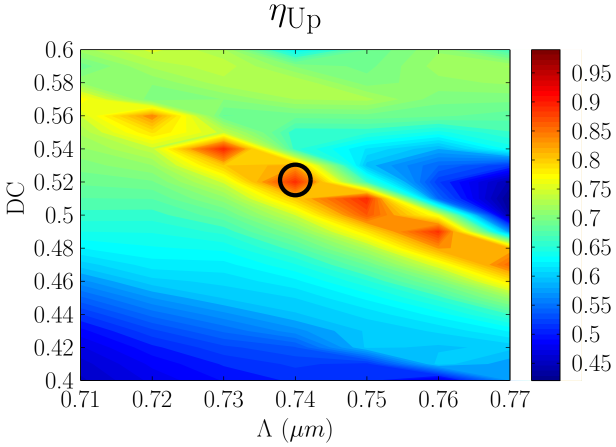

Figure 2.33.: Grating directionality (η_{Up}) for TE polarization as a function of grating pitch (Λ) and duty cycle DC for 200 periods, and etch depth $t_{\mathrm{Etch}} = 750\,\mathrm{nm}$ for $1364\,\mathrm{nm}$ wavelength. η_{Up} is calculated with our Fourier-expansion based in-house tool [126] when the fundamental mode of the optimized access waveguide ($t_{\mathrm{AccWg}} = 750\,\mathrm{nm}$) is launched into the grating.

Illumination of one grating coupler inside the 2-D array is modeled as a windowed plane wave, as schematically depicted in Fig. 2.34-a. In order to find the window length (L_{W}) that maximizes coupling efficiency, matching (η_{OL}) between the radiated field and the plane wave is analyzed. The ratio of the radiated field that is coupled to the objective field can be calculated using eq. (2.20), repeated here for clarity

$$\eta_{\mathrm{OL}} = \frac{|\langle E_{\mathrm{Up}}, E_{\mathrm{Objec}}\rangle|^2}{\langle E_{\mathrm{Up}}, E_{\mathrm{Up}}\rangle \langle E_{\mathrm{Objec}}, E_{\mathrm{Objec}}\rangle}. \tag{2.33}$$

In the following discussion radiation field and plane wave are assumed to have the same angle. This way, field radiated by the grating can be defined as a decaying exponential

$$E_{\mathrm{Up}} = e^{-\alpha_{\mathrm{B}} z}, \tag{2.34}$$

where α_{B} is the attenuation constant of the Bloch-Floquet mode propagating along the grating. Plane wave is simply modeled as

$$E_{\mathrm{Objec}} = 1. \tag{2.35}$$

Then η_{Up} can be calculated as a function of the window length (L_{W}) as

$$\eta_{\mathrm{OL}} = \frac{\left|\int_0^{L_{\mathrm{W}}} e^{-\alpha_{\mathrm{B}} z}\,\mathrm{d}z\right|^2}{\int_0^{L_{\mathrm{W}}} e^{-\alpha_{\mathrm{B}} z}\,\mathrm{d}z \cdot \int_0^{L_{\mathrm{W}}}\,\mathrm{d}z}. \tag{2.36}$$

Equation (2.36) can be rewritten as

$$\eta_{\mathrm{OL}} = \frac{2 \cdot \left[1 - e^{-t}\right]}{t}, \tag{2.37}$$

where $t = \alpha_{\mathrm{B}} L_{\mathrm{W}}$. η_{OL} is maximized for $t \sim 1.256$. Then, for a given grating geometry (chosen to maximize η_{Up}), α_{B} is fixed, and window length that maximizes coupling efficiency can be calculated as

$$L_{\mathrm{B}}^{Opt} = \frac{1.256}{\alpha_{\mathrm{B}}}. \tag{2.38}$$

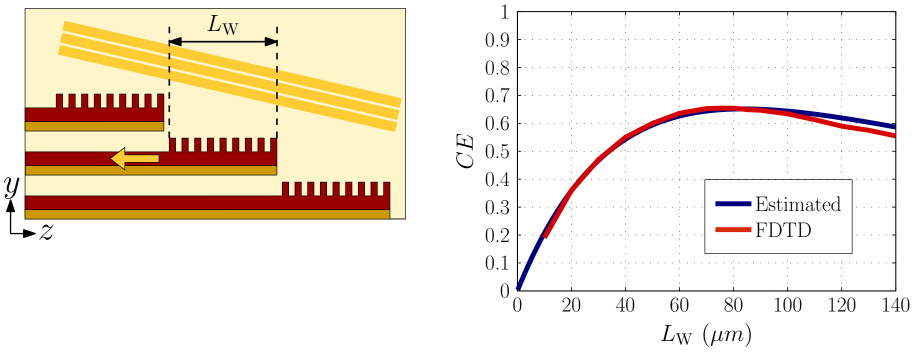

a) b)

Figure 2.34.: a) Schematic representation of illumination of a single grating coupler inside the 2-D array. **b)** Coupling efficiency for grating coupler with $\Lambda = 740\,\mathrm{nm}$ and $DC = 0.53$ as a function of window length L_{W} calculated: i) using eq. (2.39) (blue line), and ii) launching a plane wave into the grating at the optimum angle and calculating power coupled to the fundamental mode of the access waveguide using commercial FDTD tool RSoft FullWave (red line).

Grating-to-plane-wave coupling efficiency can then be estimated using the following expression

$$CE_{Esti.} = \frac{P_{\mathrm{Up}}}{P_{\mathrm{Up}} + P_{\mathrm{Down}}} \cdot \frac{2 \cdot \left[1 - e^{-t}\right]}{t}, \tag{2.39}$$

where the power radiated up (P_{Up}) and down (P_{Down}) are extracted form the directionality analysis presented in Fig 2.33. Figure 2.34-b, shows coupling efficiency estimated for the proposed grating design (blue line) as a function of the window length (L_{W}). Coupling to the fundamental mode of the access waveguide when a plane wave (at the optimum angle) is launched into the grating is calculated using commercial FDTD tool RSoft Fullwave as a function of the window length (red line in Fig. 2.34-b). The very good agreement between both results validates the proposed optimization process.

Note that the 2-D model shown in Fig. 2.34-a used for the CE simulations and estimation presented in 2.34-a does not account for the mismatch along the transversal x dimension between the field radiated by the grating (with a Gaussian-like shape) and the plane wave. Hence, although the CE dependence with window length (L_{W}) is correctly predicted, its calculated value is overestimated.

In order to experimentally characterize the proposed design, $\sim 90\,\mu$m x $90\,\mu$m grating arrays (composed of six individual grating couplers $15\,\mu$m x $90\,\mu$m each) were fabricated at the Canadian Photonics Fabrication Center using i-line stepper lithography and reactive ion etching (see Figs 2.35-a and 2.35-b). Couples of nominally identical grating arrays are arranged in a back-to-back configuration interconnected by an array

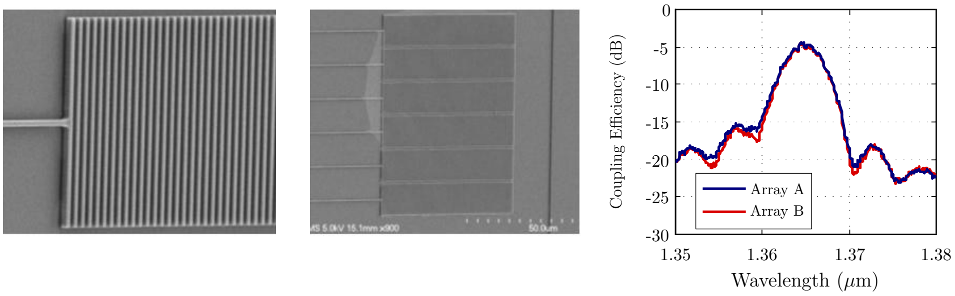

a) b) c)

Figure 2.35.: Scanning electron microscope image of the fabricated devices showing **a)** closeup of end of inverse taper and grating coupler, and **b)** $90\,\mu\mathrm{m}$ x $90\,\mu\mathrm{m}$ grating array, composed of six individual grating couplers $15\,\mu\mathrm{m}$ x $90\,\mu\mathrm{m}$ each. **c)** Experimental coupling efficiency for two different realizations of the grating array.

of rib waveguides of identical length. Light coming from a polarized tunable laser is coupled to the chip via a polarization maintaining fiber connected to a collimating GRIN lens ($0.4\,\mathrm{mm}$ diameter beam $1/e^2$ intensity at $1354\,\mathrm{nm}$ wavelength). Light diffracted by the output grating array is collected using a multimode fiber and injected to an InGaAs photodetector. Coupling efficiency of one grating coupler is obtained from power measured in the photodetector, subtracting setup loss and interconnection waveguide propagation loss, and dividing by two. Setup loss is calibrated recording the signal transmitted through a $100\,\mu\mathrm{m}$ x $100\,\mu\mathrm{m}$ slit, similar to the area of the grating array. An interconnection waveguide loss of $\sim 2\,\mathrm{dB/cm}$ at $1354\,\mathrm{nm}$ wavelength is determined in an independent measurement using the minimum phase technique [127]. Figure 2.35-c shows measured coupling efficiency for two different couples of grating arrays. Peak coupling efficiency of $-4.5\,\mathrm{dB}$ are demonstrated for an array of gratings with the proposed $\Lambda = 740\,\mathrm{nm}$ and $DC = 0.53$.

2.3. Conclusions

The recent experimental demonstration of bending radii of only $10\,\mu\mathrm{m}$ for $4\,\mu\mathrm{m}$ thick SOI waveguides [43] has brought back the focus to the micron-scale SOI technology. Integration density comparable to that of the nanometric Si-wires is potentially achievable for the micrometric SOI waveguides with the advantages of their superior performance in terms of loss and polarization dependence. Thus, the implementation of micrometric grating couplers, widely used in Si-wires, becomes a key issue to match the features of both platforms. Transferring the grating concept from the nano to the micron scale waveguides is not obvious for two reasons:

- Grating couplers in micrometric waveguides are vertically multimode, potentially producing several radiation beams (with different angles) thus reducing maximum achievable coupling efficiency

- Minimum feature size of standard fabrication processes, $\sim 350\,\mathrm{nm}$, avoids the use of the $k = -1$ radiation order, used in Si-wire gratings to provide single beam radiation.

One of the main contributions of this thesis is the proposal, and demonstration, for the first time (to the best of our knowledge) of alternative solutions to circumvent these two intrinsic limitations, consisting on

- The use of an inverse taper as excitation stage to avoid the excitation of higher order modes in the grating region and minimize back-reflections.
- The use of the $k = -2$ order in the grating design, that enables larger dimensions and thus the use of standard i-line stepper fabrication. Conditions are derived to ensure single-beam radiation for gratings working with higher-order harmonics.

The proposed solutions have been successfully applied to grating coupler designs for both TE and TM polarizations and wavelengths of $1550\,\mathrm{nm}$ and $1364\,\mathrm{nm}$ [61,63,69,71,72].

Using inverse taper excitation stage and $k = -2$ harmonic order, coupling efficiency of $-2.2\,\mathrm{dB}$ between an uniform grating and a cleaved single-mode fiber SMF-28 has been experimentally demonstrated [63]. Grating couplers have been fabricated with a single etch step (for grating coupler and interconnection waveguides) on a $1.5\,\mu\mathrm{m}$ thick SOI rib waveguide [63]. High directionality ($\eta_{\mathrm{Up}} \sim 0.9$) is achieved just by judiciously choosing etch depth ($t_{\mathrm{Etch}} = 750\,\mathrm{nm}$), pitch ($\Lambda = 860\,\mathrm{nm}$) and duty cycle ($DC = 0.5$), without the need of any bottom reflector. Furthermore, grating performance is slightly affected by the BOX thickness. This design has been theoretically extended to polarization independent behavior adding a bottom metal reflector, showing coupling efficiency of $-3\,\mathrm{dB}$ simultaneously for both TE and TM polarizations [69]. 2-D grating array composed by 6 gratings ($15\,\mu\mathrm{m}$ x $90\,\mu\mathrm{m}$ each, using inverse taper and $k = -2$ harmonic radiation) has been designed to increase optical throughput of a Fourier-transform spectrometer to monitor water vapor absorption in the atmosphere form an Earth satellite [71]. Coupling efficiency of $-4.5\,\mathrm{dB}$ has been measured when the grating array is illuminated with a plane wave at $1364\,\mathrm{nm}$ (peak water absorption) [72].

3

Polarization Management

3.1. Introduction

Direct detection modulation formats have been widely and successfully used to implement optical communication systems, specially since the development of the erbium doped fiber amplifier (EDFA) in the early nineties. More recently, the improvement of laser coherence (narrower spectral linewidth), and the increased data rate requirements have driven the use of coherent phase-modulated systems. The use of higher order modulation schemes such as QPSK or 16QAM, has been proposed to improve system capacity. In order to further increase available data rates, the use of polarization-multiplexed communications systems has been proposed [130]. In these systems, two coherent phase-modulated signals are carried by two orthogonal polarization states of the optical fiber. In fact, polarization-multiplexed coherent communication systems are foreseen as the key technology in future generation 100-400Gb/s communication systems [47].

Preferred architectures for polarization multiplexed transceivers are defined by the Optical Internetworking Forum (OIF) [131]. In the transmitter side [60] (see Fig. 3.1-a) TE light coming from a laser source is split in two branches. Each branch is phase-modulated with a different information. A polarization beam rotator (PBR) placed in one of the arms transforms modulated TE signal to TM polarization. A polarization beam combiner (PBC) is used to combine both branches generating the polarization-multiplexed phase-modulated signal. In the receiver side [60, 132–134] (see Fig. 3.1-b) incoming signal is polarization split in a polarization beam splitter (PBS). Then each polarization component is launched into a different downconverter. If a PBR is used, both downconverters can be designed to work with the same polarization, typically TE.

Monolithic integration of all the elements composing the transmitter and receiver is aimed to make the system more stable and robust to environmental conditions, and to reduce the number of fiber couplers and packaging costs. Stringent fabrication tolerances of integrated polarization rotators [51, 56, 75] and splitters [135, 136] reduce their yield, hindering their use in commercial applications. For that reason, despite the advantages of monolithic integration, commercial dual-polarization transceivers implement polarization management (PBS and PBR) off-chip [60]. Thus, development of integrated polarization rotators and splitters with improved robustness to fabrication errors is pur-

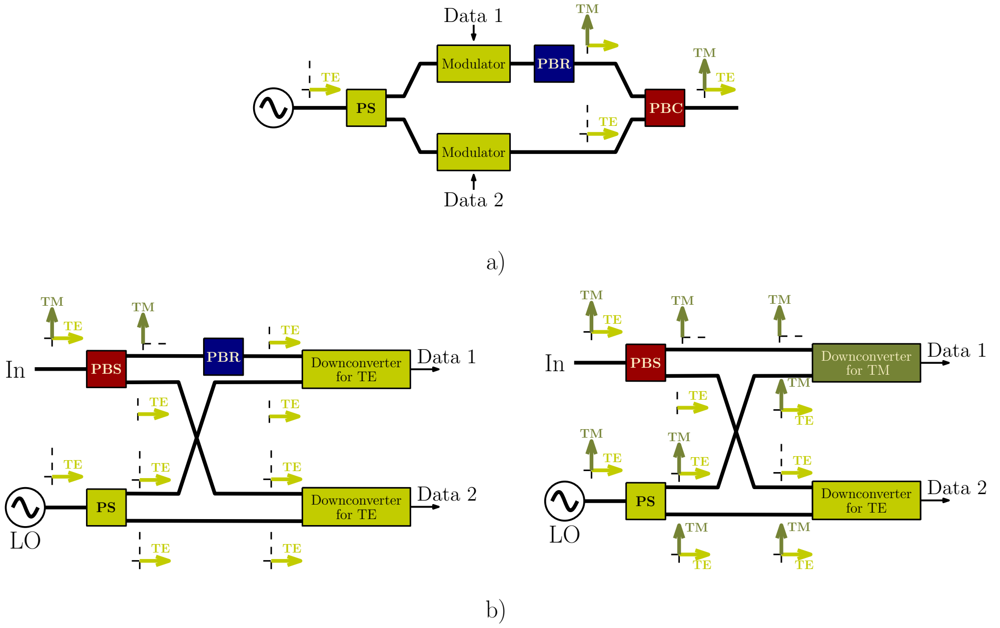

Figure 3.1.: Schematic representation of polarization-multiplexed **a)** transmitter and **b)** receiver, composed by a PBS, PBR and a PS (left hand side) or a PBS and BS (right hand side). PBS, PBR, and PS stand for polarization beam splitter, polarization beam rotator and power splitter, respectively.

sued [77,136–138], as they are considered key building blocks of future generation high-performance polarization-multiplexed transceivers.

3.2. Integrated Polarization Rotators

This section is dedicated to the analysis and design of passive integrated polarization rotators. First, working principle of integrated polarization rotators is qualitatively described. Special attention is devoted to the rotator waveguide approach, as it is a key component of the designs proposed in this section. In section 3.2.1 the design of a rotator waveguide integrable with an InP front-end is discussed, that illustrates stringent fabrication tolerances of integrated polarization rotators. Finally, in section 3.2.2, a novel polarization rotation scheme is presented that substantially increases tolerances to fabrication errors.

Working Principle

Most of the passive integrated polarization rotators proposed in literature are based on one of the following approaches:

- Mode evolution (Fig. 3.2-a): waveguide transversal geometry is adiabatically changed to produce the desired polarization transformation [48].
- Cross-polarization coupling (Fig. 3.2-b): fundamental TE (TM) mode of the waveguide is coupled to a higher order TM (TE) mode of the same waveguide [49] or

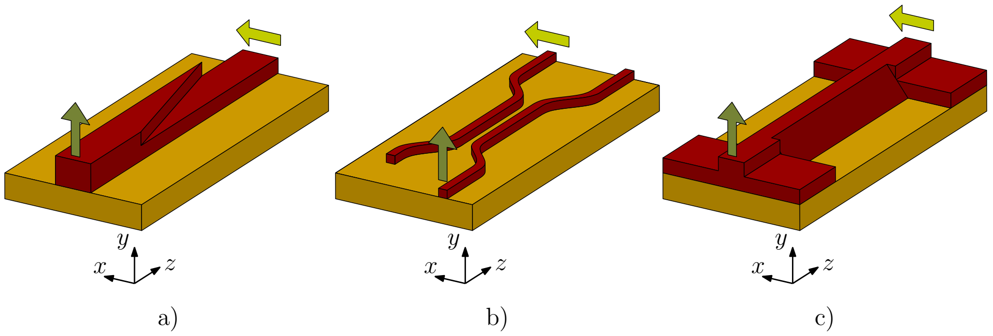

Figure 3.2.: Passive integrated polarization rotators based on: **a)** mode evolution, **b)** cross polarization coupling, and **c)** rotator waveguide section.

hybrid super-modes of a directional coupler [50]. Polarization rotation is provided by the power transfer between the coupled modes.

- Rotator waveguide section (Fig. 3.2-c): this is a widely used solution, specially in the InP platform. Its working principle discussed in detail below.

Rotator Waveguide

In rotator waveguide based rotators, one or several sections of waveguides that support hybrid modes (that are tilted respect to the canonical TE and TM modes) are placed between an input and an output conventional waveguides. Figure 3.2-c schematically represents a single-section rotator waveguide device.

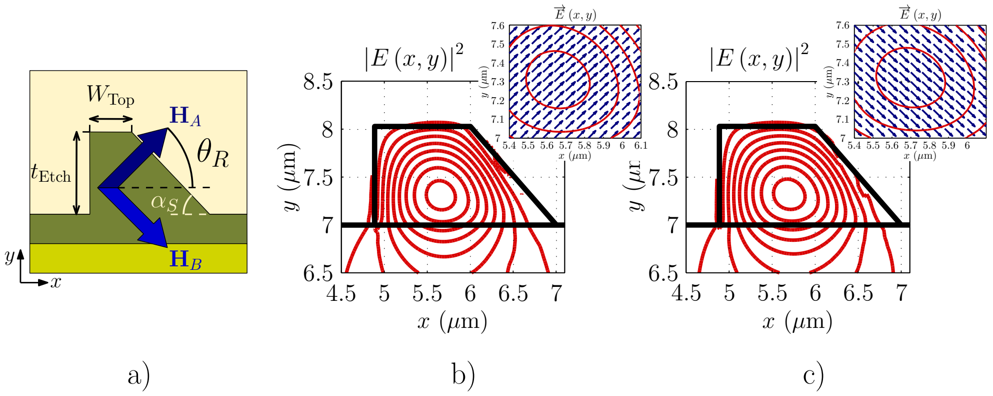

Figure 3.3.: **a)** Transversal geometry of slanted rotator waveguide and orientation of the two first hybrid modes (H_A and H_B). Electric field distribution of **b)** first and **c)** second hybrid modes.

In order to support hybrid modes, rotator waveguides use transversal geometries that are neither vertically, nor horizontally symmetric. Rotator waveguides with one [51–53] or two [54] slanted walls, a single [55] or multiple trenches [56], slanted slots [57], or two thicknesses [58] have been proposed.

Rotator waveguides are generally described by means of two modal characteristics: the hybrid modes tilt angle, θ_R, and modal phase-shift, ϕ_R. Hybrid modes (H_A and H_B) in a rotator waveguide are aligned to orthogonal axis that are θ_R tilted respect to the canonical TE/TM axis, as described in Fig. 3.3-a. θ_R can be calculated from the mode field distribution as

$$\theta_R = \arctan\left(\frac{\int\int_\Omega |E_y|^2 \, \mathrm{d}\Omega}{\int\int_\Omega |E_x|^2 \, \mathrm{d}\Omega}\right), \tag{3.1}$$

with Ω the modal area, and E_x, E_y the horizontal and vertical electrical components, respectively [77]. Modal phase-shift, ϕ_R, describes the phase-shift produced between the hybrid modes as they propagate along the waveguide, and can be calculated as

$$\phi_R = (\beta_{\mathrm{H}_A} - \beta_{\mathrm{H}_B})\, L_R, \tag{3.2}$$

being β_{H_A} and β_{H_B} the phase propagation constants of the two first hybrid modes, and L_R the length of the rotator waveguide section. Note that ϕ_R depends on the rotator waveguide modal properties (and thus on wavelength, and waveguide transversal geometry and materials) and rotator waveguide length (L_R), while θ_R only depends on waveguide modal properties.

Multi-section rotator waveguide devices are usually very long ($\sim 1\,\mathrm{mm}$) and have high insertion loss ($2 - 3\,\mathrm{dB}$) [139, 140]. Thus, single-section rotators are generally preferred. In order to have perfect rotation in a single-section device, rotator waveguide needs to have $\theta_R = 45°$ and $\phi_R = 180°$ [51]. For that reason, the length required to produce a 180° modal phase-shift, so called half-beat length (L_{180}), is another parameter used to describe rotator waveguides. Half-beat length can be calculated as

$$L_{180} = \frac{\pi}{\beta_{\mathrm{H}_A} - \beta_{\mathrm{H}_B}}. \tag{3.3}$$

Figure 3.3-a schematically depicts transversal geometry of a typical slanted rotator waveguide. Slant angle (α_S) is determined by the fabrication process, being waveguide top width (W_{Top}) and etch depth (t_{Etch}) designed to achieve desired hybrid modes tilt angle (θ_R) [51]. Figures 3.3-b and 3.3-c show field mode profile ($|E(x,y)|^2$ in red lines, and $\overrightarrow{E}(x,y)$ in blue arrows) of the two first hybrid modes supported by a rotator waveguide designed to have $\theta_R = 45°$. It can clearly be seen that the electric filed of the modes is tilted, exhibiting an hybrid distribution (neither TE, nor TM).

Working principle of TE-to-TM polarization rotation in an ideal single-section rotator waveguide ($\theta_R = 45°$ and $\phi_R = 180°$) is schematically depicted in Fig. 3.4. The TE-to-TM rotation can be described as a three steps process:

- i) The canonical TE mode coming from the input waveguide is projected onto the two hybrid modes of the rotator waveguide, exciting them in the same amount.
- ii) Due to their different phase constants, excited hybrid modes are phase-shifted as they propagate along the rotator waveguide. At the end of the waveguide, they are 180°-shifted.
- iii) Hybrid modes are projected onto the canonical output waveguide modes exciting only the TM mode, and thus, producing the desired rotation.

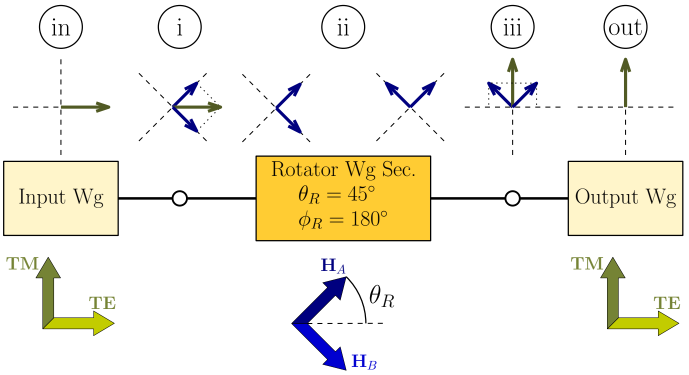

Figure 3.4.: Working principle of TE-to-TM polarization rotation in an ideal single-section rotator waveguide ($\theta_R = 45°$ and $\phi_R = 180°$).

Polarization transformation produced in any (ideal or not) single-section rotator waveguide can be described, generalizing this three steps process, using the Jones matrix formalism [77]. Complete device is modeled as follows:

- i) Projection from canonical to hybrid modes can be described by the projection Jones matrix, $J_P\left(\theta_R\right)$,

$$J_P(\theta_R) = \begin{bmatrix} cos(\theta_R) & sin(\theta_R) \\ -sin(\theta_R) & cos(\theta_R) \end{bmatrix}, \tag{3.4}$$

- ii) Modal phase-shift can be described using the phase-shift Jones matrix, $J_{PS}\left(\phi_R\right)$,

$$J_{PS}(\phi_R) = \begin{bmatrix} e^{(j\phi_R)} & 0 \\ 0 & 1 \end{bmatrix}, \tag{3.5}$$

- iii) Final hybrid to canonical mode projection can be described by the projection Jones matrix, $J_P\left(-\theta_R\right)$,

$$J_P(-\theta_R) = \begin{bmatrix} cos(\theta_R) & -sin(\theta_R) \\ sin(\theta_R) & cos(\theta_R) \end{bmatrix}. \tag{3.6}$$

Then, a rotator Jones matrix $J_R\left(\theta_R,\, \phi_R\right)$, can be defined that describes the complete rotator as

$$\begin{aligned} J_R\left(\theta_R,\, \phi_R\right) &= J_P\left(-\theta_R\right) \cdot J_{PS}\left(\phi_R\right) \cdot J_P\left(\theta_R\right) \qquad (3.7) \\ &= \begin{bmatrix} e^{(j\phi_R)} cos^2(\theta_R) + sin^2(\theta_R) & \frac{e^{(j\phi_R)}-1}{2} sin(2\theta_R) \\ \frac{e^{(j\phi_R)}-1}{2} sin(2\theta_R) & cos^2(\theta_R) + e^{(j\phi_R)} sin^2(\theta_R) \end{bmatrix}. \end{aligned}$$

This way, generic polarization states at the input (A_{in}) and output (A_{out}) of the rotator are related by $J_R\left(\theta_R,\, \phi_R\right)$ as

$$\begin{aligned} A_{out} &= J_R(\theta_R, \phi_R) \cdot A_{in} \qquad (3.8) \\ \begin{bmatrix} A_{out}^{TE} \\ A_{out}^{TM} \end{bmatrix} &= J_R(\theta_R, \phi_R) \cdot \begin{bmatrix} A_{in}^{TE} \\ A_{in}^{TM} \end{bmatrix} \end{aligned}$$

being $A^{TE,TM}_{in,out}$ the complex amplitudes of the TE and TM field components at the input and output of the rotator.

Quality of a (TE-to-TM or TM-to-TE) polarization rotator is usually measured using the polarization conversion efficiency (PCE) [51]. PCE is defined as the ratio between the power in the desired polarization (TM for TE input or TE for TM input) and the total power at the output of the rotator

$$PCE = \frac{P^{W}_{out}}{P^{W}_{out} + P^{UW}_{out}}, \tag{3.9}$$

being P^{W}_{out} and P^{UW}_{out} the power in the wanted and unwanted polarization components at the output waveguide. Ideally, perfect rotation is produced, and all the power is in the desired polarization, then $PCE = 1$.

Using eqs. (3.7) and (3.8), and assuming that input field is either TE or TM polarized, PCE can be rewritten as a function of the rotator waveguide characteristic parameters θ_R and ϕ_R as

$$PCE = \sin^2(2\theta_R) \cdot \sin^2(\phi_R/2). \tag{3.10}$$

From eq. (3.10), it is clear that perfect rotation ($PCE = 1$) can only be achieved for $\theta_R = \pm 45°$ and $\phi_R = \pm 180°$. It can also be seen that rotator performance quickly deteriorates when rotator parameters deviate from the optimum ones. Polarization conversion efficiency is four times more sensitive to deviations in the hybrid modes tilt angle (θ_R) than to modal phase-shift (ϕ_R) deviations, as θ_R is multiplied by two in the $\sin$ argument while ϕ_R is divided by two. For instance, if a $PCE > 0.95$ is aimed, the maximum allowed deviations for θ_R and ϕ_R are $\pm 5°$ and $\pm 20°$ respectively. Unfortunately, these requirements are very difficult to meet due to tolerances of fabrication processes, complicating the realization of waveguide polarization rotators with high PCE.

3.2.1. Polarization Rotator for InP Waveguides

As already mentioned in the introduction of this chapter, integrated polarization splitters and rotators are a key component of future generation monolithically integrated dual-polarization coherent transceivers. In this section, the implementation of an integrated polarization rotator fully compatible with a previously reported monolithic InP frontend for coherent 100GE [141] is discussed. The proposed design example illustrates the stringent fabrication tolerances of integrated polarization rotators.

Device design

In order to be monolithically integrable with the existing receiver, rotator waveguide should be compatible with interconnection waveguides used in the rest of the device. Interconnection waveguide transversal geometry is depicted in Fig. 3.5-a. Waveguide thickness and etch depth are fixed to $t_{\mathrm{Wg}} = 1045\,\mathrm{nm}$ and $t_{\mathrm{Etch}} = 450\,\mathrm{nm}$ [141].

The most typical approach to implement polarization rotators in the InP platform is the slanted waveguide (see Fig. 3.5-b) [51–53]. In order to be able to support $\theta_R = 45°$ tilted hybrid modes (required to provide perfect rotation), the slanted rotator waveguide etch depth needs to be $t_{\mathrm{Etch}} > 0.7 \cdot t_{\mathrm{Wg}}$ [51]. Interconnection waveguides have an etch

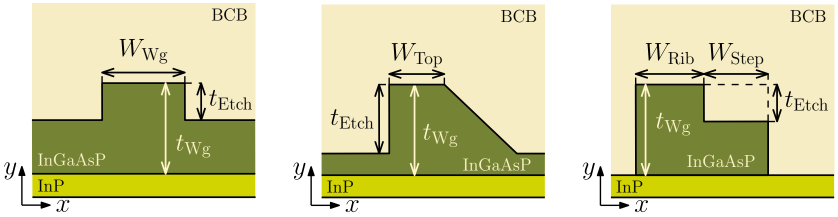

a) b) c)

Figure 3.5.: Transversal geometry of: **a)** interconnection rib waveguide, **b)** typical slanted rotator waveguide, and **c)** proposed two thicknesses rotator waveguide.

depth $t_{\mathrm{Etch}} = 0.43 \cdot t_{\mathrm{Wg}}$. Hence, the implementation of a circuit that comprises rib interconnection waveguides and the slanted rotator waveguide would require three etch steps: one dry (shallow) etch step for the interconnection waveguides, one dry (deep) etch step for the straight rotator wall, and one wet etch step for the slanted rotator wall.

In order to reduce device fabrication complexity, the use of a two thicknesses rotator waveguide, depicted in Fig. 3.5-c, is proposed. This two steps geometry could intuitively be understood as a first order approximation of a slanted wall. Waveguide thickness t_{Wg} and etch depth t_{Etch} are respectively set to $1045\,\mathrm{nm}$ and $425\,\mathrm{nm}$ to be compatible with the interconnection waveguides. As discussed below, $45°$ tilt can be achieved by properly choosing the widths W_{Rib} and W_{Step}. This way, a circuit that includes interconnection waveguides and proposed rotator waveguide could be fabricated using only two dry etch steps: one for interconnection waveguides and shallow etched rotator wall, and one for fully etched rotator wall.

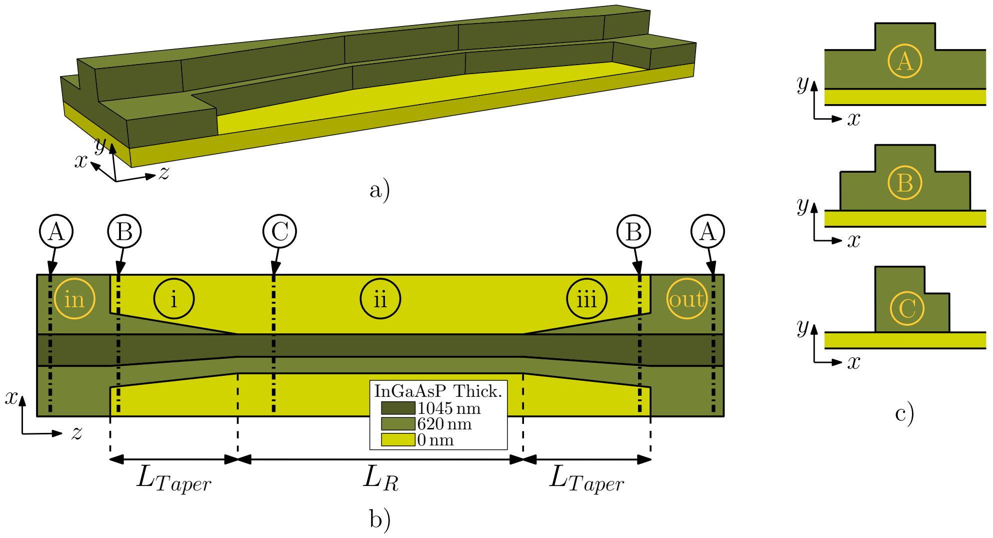

a) b) c)

Figure 3.6.: **a)** 3-D structure, and **b)** top view of complete proposed rotator scheme. **c)** Transversal geometry of A input and output waveguides, B beginning of taper and, C rotator waveguide.

Complete rotator is schematically represented in Fig. 3.6. Input and output waveguides have a rib transversal geometry (that of the interconnection waveguides) that supports canonical TE-TM modes. Rotator waveguide section is implemented using the proposed two thicknesses transversal geometry, designed to support $\theta_R = 45°$ tilted hybrid modes. Projections between TE-TM and hybrid modes (and viceversa) occurs in the tapers (regions i and iii in Fig. 3.6-b). Taper length ($L_{Taper} = 70\,\mu\text{m}$) is chosen to be long enough to minimize insertion loss, and short enough to ensure that both hybrid modes are excited in the same amount.

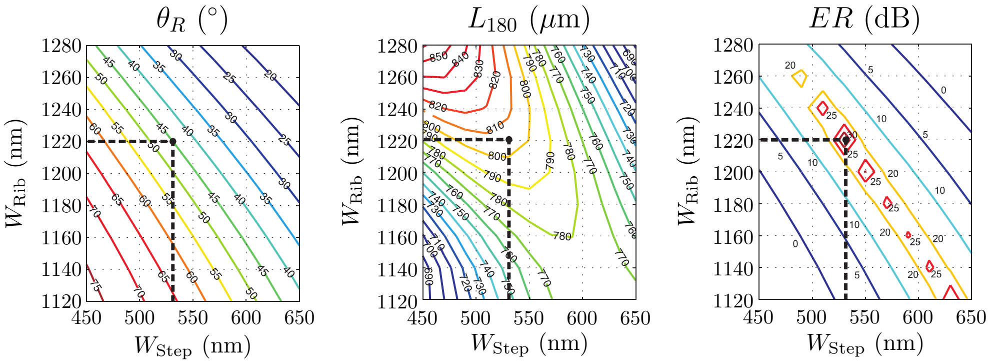

a) b) c)

Figure 3.7.: a) Hybrid modes tilt angle (θ_R) as a function of the widths W_{Rib}, W_{Step}. **b)** Half-beat length (L_{180}) of the waveguide rotator as a function of the widths W_{Rib}, W_{Step}. **c)** ER as a function of the widths W_{Rib}, W_{Step} for $L_R = 805\,\mu\text{m}$.

Hybrid modes tilt angle θ_R, defined in eq. (3.1), and the rotator half-beat length L_{180}, defined in eq. (3.3), are analyzed to optimize rotator waveguide geometry. As mentioned before, waveguide thickness and etch depth are fixed ($t_{\text{Wg}} = 1045\,\text{nm}$ and etch depth $t_{\text{Etch}} = 425\,\text{nm}$), and only waveguide widths W_{Rib} and W_{Step} (defined in Fig. 3.5-b) can be designed to provide desired rotator performance. Minimum boundaries of $W_{\text{Rib}} > 1100\,\text{nm}$ and $W_{\text{Step}} > 450\,\text{nm}$ are set in order to have sufficient modal field confinement and to avoid too small feature sizes. 3-D modal analysis is performed using the full-vectorial commercial tool Fimmwave.

Calculated θ_R is presented in Fig. 3.7-a, showing that the desired $\theta_R = 45°$ can be achieved for a variety of W_{Rib} and W_{Step} pairs. θ_R is found to be very sensitive to width errors. A typical $\pm 100\,\text{nm}$ width error, i.e. a $\sim 5\%$ deviation from nominal value, produces changes of $\pm 20°$ ($\sim 45\%$) in the hybrid modes tilt angle.

Calculated L_{180} is presented in Fig. 3.7-b. Rotator half-beat length is more robust to waveguide width errors, with changes of $\sim 10\%$ for $\pm 100\,\text{nm}$ width errors.

Polarization extinction ratio (ER), defined as the ratio between the power in the wanted (P_{out}^{W}) and unwanted (P_{out}^{UW}) polarizations components in the output waveguide, is calculated from the polarization conversion efficiency, defined in eq. (3.10), as

$$ER = \frac{P_{out}^{W}}{P_{out}^{UW}} = \frac{PCE}{1 - PCE}. \tag{3.11}$$

Figure 3.7-c shows calculated ER as a function of rotator waveguide widths. Rotator length is fixed to $L_R = 805\,\mu\text{m}$, corresponding to the half-beat length for $W_{\text{Rib}} = 1220\,\text{nm}$ and $W_{\text{Step}} = 530\,\text{nm}$. As expected, ER is very sensitive to fabrication errors.

A waveguide width variation of 5% ($\pm 100\,\mathrm{nm}$) reduces ER below $5\,\mathrm{dB}$. Comparing ER results with θ_R and ϕ_R it can be seen that the main factor limiting rotator tolerance to fabrication errors is hybrid mode tilt angle deviation.

Finally, propagation along the 3-D structure shown in Fig. 3.6-a is analyzed using Fimmprop. Optimum dimensions are found to be $W_{\mathrm{Rib}} = 1220\,\mathrm{nm}$, $W_{\mathrm{Step}} = 530\,\mathrm{nm}$, $L_R = 748\,\mu\mathrm{m}$ and $L_{Taper} = 70\,\mu\mathrm{m}$. Rotator length ($L_R$) is slightly shorter than calculated half-beat length ($L_{180} = 805\,\mu\mathrm{m}$) as the phase-shift produced in the input and output tapers needs to be compensated. Optimized device exhibits a calculated ER of $40\,\mathrm{dB}$ at $1550\,\mathrm{nm}$ wavelength with insertion loss of $0.04\,\mathrm{dB}$, covering the full telecommunications C-band with an ER better than $20\,\mathrm{dB}$.

Conclusions

The use of a two thicknesses rotator waveguide has been proposed. Rotator waveguide geometry, that can be fabricated using two dry etch steps, is designed to be fully compatible with a previously reported monolithically integrated InP coherent receiver [141] exhibiting calculated ER of $40\,\mathrm{dB}$ with $0.04\,\mathrm{dB}$ insertion loss. However, tolerance analysis shows that the device is very sensitive to waveguide width errors hindering its practical implementation.

3.2.2. Tunable Polarization Rotator Scheme

Many different alternatives have been proposed for the implementation of integrated polarization rotators. However, all of them relay on the use of a very precise waveguide transversal geometry, and thus are very sensitive to fabrication errors. This limitation seriously hinders their use in large scale commercial applications where yield is a key issue. Thus, a large effort is being devoted to improve rotator tolerances [137, 138]. In this section, a novel polarization rotator scheme is presented that enables correction of fabrication errors, based on conventional (thermo-optic or electro-optic) actuators, substantially improving device robustness and yield. Furthermore, the proposed scheme enables dynamic selection of desired central wavelength.

Proposed Scheme

The very well known manual fiber polarization controller can perform any required polarization transformation, including perfect TE-to-TM or TM-to-TE rotation. This ability to produce any arbitrary polarization rotation is not subject to stringent restrictions on the characteristics of the elements composing the controller.

This controller is generally composed by three paddles loaded with winded fiber sections, whose relative angle can be manually controlled (see Fig. 3.8-a). The device can be modeled (see Fig. 3.8-b) as a concatenation of three polarization rotators with:

- Adjustable hybrid modes tilt angles θ_{R_i}, determined by the relative position between the paddles.
- Arbitrary (i.e. unknown and not tightly controllable) modal phase-shifts ϕ_{R_i}, determined by the winding of the fiber inside the paddle

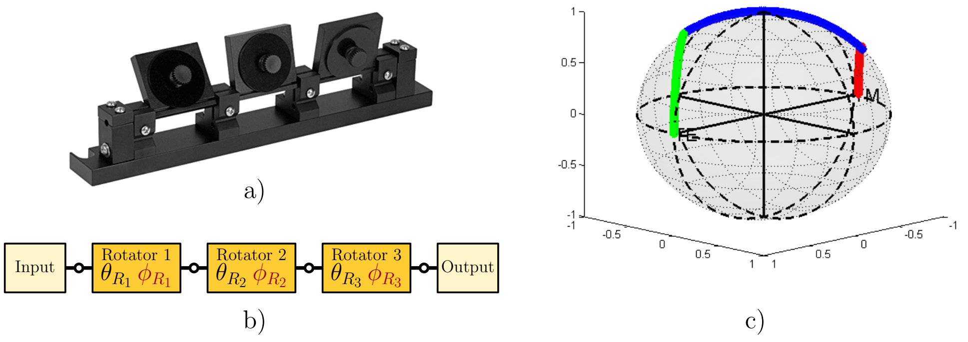
a)
b)
c)

Figure 3.8.: Manual polarization controller: **a)** example, **b)** block diagram. **c)** Polarization transformation produced when TE polarized light is launched into a fiber controller with $\phi_{R_i} = 90°$, $\theta_{R_1} = 25.36°$, $\theta_{R_2} = 68.49°$, and $\theta_{R_3} = 21.13°$.

As an example of the controller behavior, polarization transformation produced when TE polarized light is launched into a fiber controller with $\phi_{R_i} = 90°$ is represented in the Poincaré sphere in Fig. 3.8-c. Hybrid mode tilt angles ($\theta_{R_1} = 25.36°$, $\theta_{R_2} = 68.49°$, and $\theta_{R_3} = 21.13°$) are chosen to provide perfect (TE-to-TM) rotation.

By concatenating three different rotators, requirements on each single device are substantially relaxed. Thanks to this, perfect rotation can be achieved for a wide range of modal phase-shifts (ϕ_{R_i}) by properly adjusting rotators tilt angles (θ_{R_i}).

Unfortunately, the manual fiber polarization controller scheme can not be used to alleviate stringent fabrication tolerances of rotator waveguides implemented on SOI or InP platforms. In the controller scheme, hybrid modes tilt angle need to be adjustable during operation to provide a wide working range. In integrated rotator waveguides, transversal geometry, and thus θ_R, are fixed once fabricated, precluding dynamic θ_R tunning.

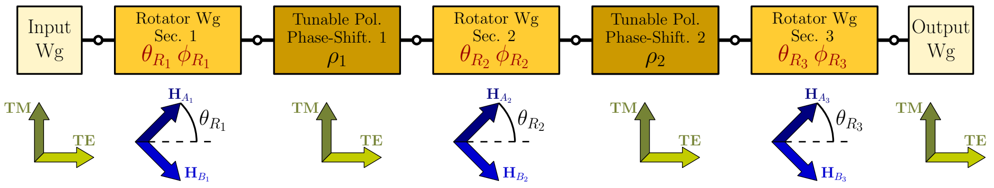

Figure 3.9.: Proposed tunable rotator scheme, composed by input and output waveguides, three rotator waveguide sections, and two tunable polarization phase-shifters.

An alternative rotator scheme, compatible with integrated SOI and InP platforms, is proposed that provides perfect rotation for rotator waveguide sections with a wide range of hybrid projection angles and modal phase-shifts. Proposed scheme, presented in Fig. 3.9, is composed by:

- Input and output waveguides that support canonical TE and TM modes.

- Three rotator waveguide sections with arbitrary hybrid mode tilt angles (θ_{R_i}) and modal phase-shifts (ϕ_{R_i}) that model the effect of unknown and uncontrolled fabrication errors.

- Two polarization phase-shifters, that introduce adjustable phase-shifts (ρ_1, ρ_2) between TE and TM components. They can be implemented, for example, applying the thermo-optic or electro-optics effects on conventional birefringent waveguides.

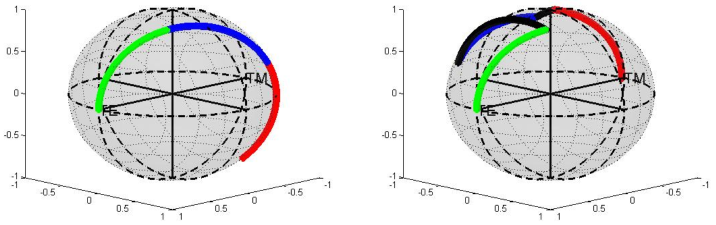

a) b)

Figure 3.10.: Polarization transformation produced when TE polarized light is launched into the tunable scheme with rotator waveguide sections with $\theta_{R_i} = 57°$ and $\phi_{R_i} = 77°$ when polarization phase-shift are **a)** $\rho_1 = \rho_2 = 0°$, i.e no phase-shift, and **b)** $\rho_1 = 91.6°$, $\rho_2 = 342.8°$, i.e. adjusted for perfect rotation.

Three rotators and two phase-shifters are the minimum number of elements required to achieve perfect polarization rotation with non-ideal rotator waveguide sections. Deviations in the parameters of the rotator waveguides produced by fabrication errors can be compensated by means of properly choosing the polarization phase-shifts ρ_1 and ρ_2. Figure 3.10-a represents polarization transformation produced in the proposed scheme when rotator waveguide sections largely deviated from nominal values ($\theta_{R_i} = 57°$, $\phi_{R_i} = 77°$) are considered, and no polarization phase-shift is introduced ($\rho_1 = \rho_2 = 0°$). When the proper polarization phase-shifts are used ($\rho_1 = 91.6°$, $\rho_2 = 342.8°$), rotator waveguide deviations are compensated and perfect rotation is achieved, as shown in Fig. 3.10-b.

It can be demonstrated (see Appendix A.1) that the proposed scheme can provide perfect polarization rotation for any triplet of rotator waveguide sections meeting the following condition

$$[\alpha_{R_2} \cdot \gamma_{R_1} - \alpha_{R_1} \cdot \gamma_{R_2}]^2 < \gamma_{R3}^2 < [\alpha_{R_2} \cdot \gamma_{R_1} + \alpha_{R_1} \cdot \gamma_{R_2}]^2 , \qquad (3.12)$$

being α_{R_i} and γ_{R_i} a function of the rotators characteristic parameters θ_{R_i} and ϕ_{R_i}

$$\begin{aligned} \alpha_{R_i} &= \sin(2\theta_{R_i}) \cdot \sin(\phi_{R_i}/2) \qquad (3.13) \\ \gamma_{R_i} &= \sqrt{\cos^4(\theta_{R_i}) + \sin^4(\theta_{R_i}) + 2 \cdot \cos^2(\theta_{R_i}) \cdot \sin^2(\theta_{R_i}) \cdot \cos(\phi_{R_i})}. \end{aligned}$$

Considering that the three rotator waveguide sections can be placed very close in the chip layout, it is reasonable to assume that they are affected by the same fabrication errors.

Then, they have the same characteristic parameters ($\theta_{R_i} = \theta_R$ and $\phi_{R_i} = \phi_R$), and eq. (3.12) reduces to

$$\sin^2(2\theta_R) \cdot \sin^2(\phi_R/2) > \frac{1}{4}. \tag{3.14}$$

Note that the left-hand side of eq. (3.14) resembles the polarization conversion efficiency definition given in eq. (3.10). Thus, it can be concluded that the minimum requirement to be able to achieve perfect rotation ($PCE = 1$) with the proposed tunable scheme is to use rotating elements that can provide $PCE > 0.25$ each. This is a substantial improvement compared to the conventional approach. For instance, if a $PCE > 0.95$ is aimed, the maximum allowed deviations for θ_R and ϕ_R in the conventional configuration are $\Delta\theta_R = \pm 5°$ and $\Delta\phi_R = \pm 20°$, respectively. In the tunable scheme, $PCE = 1$ can be achieved with deviations as large as $\Delta\theta_R = \pm 30°$ or $\Delta\phi_R = \pm 120°$. Combinations of θ_R and ϕ_R that provide: i) $PCE > 0.95$ in the conventional approach, and ii) feasible perfect rotation ($PCE = 1$) in the tunable scheme are marked in red in Figs. 3.11-a and 3.11-b. Improvement of the region of interest provided by the tunable scheme is clearly appreciable.

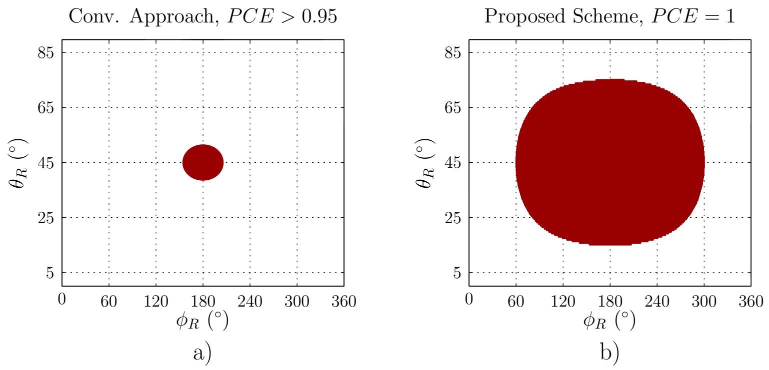

Figure 3.11.: Combinations of θ_R and ϕ_R (marked in red) that provide **a)** $PCE > 0.95$ in the conventional approach, and **b)** feasible perfect rotation ($PCE = 1$) in the tunable scheme.

Design Example

To illustrate the potential of the tunable rotator scheme, the performance of a Si-wire-based rotator waveguide is analyzed when placed inside the conventional and proposed schemes.

Input and output waveguides are Si-wires, as the one depicted in Fig. 3.12-a, with $t_{\mathrm{Wg}} = 260\,\mathrm{nm}$ and $W_{\mathrm{Wg}} = 415\,\mathrm{nm}$. Rotator waveguide is based on the two-trenches transversal geometry proposed in [56] and schematically presented in Fig. 3.12-b. Nominal dimensions are $G_1 = 60\,\mathrm{nm}$, $t_{E_1} = 210\,\mathrm{nm}$; $G_2 = 85\,\mathrm{nm}$, $t_{E_2} = 238\,\mathrm{nm}$; $W_1 = 200\,\mathrm{nm}$, $W_2 = 40\,\mathrm{nm}$ and $W_3 = 30\,\mathrm{nm}$. The refractive indices of the bottom oxide, silicon waveguide core and SU8 cladding at $1550\,\mathrm{nm}$ wavelength are $n_{\mathrm{SiO_2}} = 1.444$, $n_{\mathrm{Si}} = 3.476$ and $n_{\mathrm{SU8}} = 1.58$ respectively. The corresponding thermo-optical coefficients are $\mathrm{d}n_{\mathrm{SiO_2}}/\mathrm{d}T = 1 \times 10^{-5}\,°\mathrm{C}^{-1}$, $\mathrm{d}n_{\mathrm{Si}}/\mathrm{d}T = 1.8 \times 10^{-4}\,°\mathrm{C}^{-1}$ and

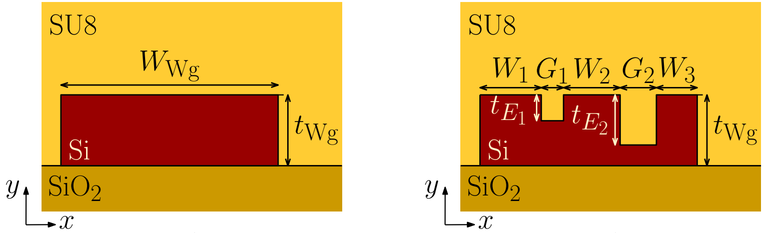

a) b)

Figure 3.12.: Cross section of **a)** Si-wire used for input-output waveguides and polarization phase-shifters, and **b)** double trench rotator waveguide.

$\mathrm{d}n_{\mathrm{SU8}}/\mathrm{d}T = -1.1 \times 10^{-4}\,^{\circ}\mathrm{C}^{-1}$ [84, 142]. All results shown in the following correspond to 3-D full-vectorial simulations of the complete rotator structure, using the commercial tool Fimmwave.

Let us first consider the conventional approach. Rotator waveguide length is set to $L_R = 13\,\mu\mathrm{m}$ ($\sim L_{180}$). Low loss transitions are used to connect rotator to the input and output waveguides. Device with nominal dimensions exhibits a calculated extinction ratio $ER > 25\,\mathrm{dB}$ when TE fundamental mode of the input waveguide is used as an input. However, as shown in Fig. 3.13-a, variations of $\Delta G = 5\,\%$ in the size of the trenches can reduce the extinction ratio to below $5\,\mathrm{dB}$. Similar performance deteriorations are observed in the InP rotator discussed in section 3.2.1, and generally in all other integrated single-section polarization rotator waveguides.

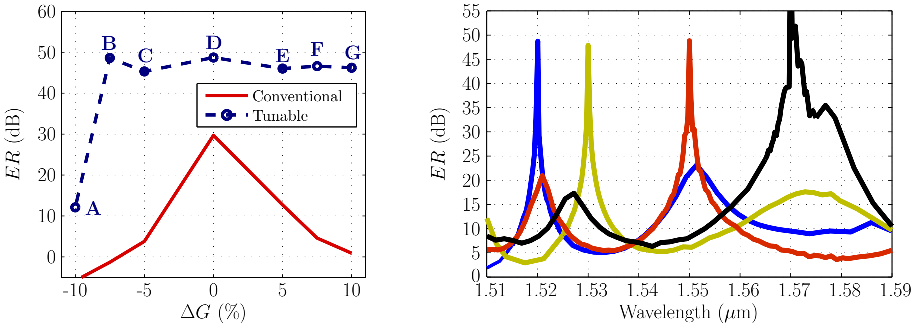

a) b)

Figure 3.13.: **a)** ER for a two-trenches rotator waveguide inside conventional (red solid line) and proposed (blue dashed line) schemes for various fabrication errors at $1550\,\mathrm{nm}$ wavelength. **b)** ER as a function of wavelength for a two-trenches rotator with a gap variation of $\Delta G = 5\%$ inside the proposed scheme tunned for various central wavelengths. Temperature increments (ΔT_1, ΔT_2) set in each case are described in table 3.1.

Let us now analyze the proposed scheme. The proposed tunable rotator scheme (see Fig. 3.9) is implemented as follows. Input and output waveguides use the same Si-wire as in conventional approach. Rotator waveguide sections use the same transversal geometry as in the conventional approach ($\theta_{R_i} = 45°$). Length of the three rotator sections is set to $L_R = 13\,\mu\mathrm{m}$ ($\phi_{R_i} = 180°$). This way nominal rotator waveguide is in

Table 3.1.: Temperature increments (ΔT_1, ΔT_2) for perfect rotation for different gap errors (ΔG) and central wavelengths (λ_c).

ΔG	λ_c (nm)	ΔT_1	ΔT_2
-10%	1550	16.5°C	16.1°C
-7%	1550	25.9°C	10.4°C
-5%	1550	31°C	9.3°C
0%	1550	33.2°C	8.7°C
5%	1550	12.3°C	37.1°C
7%	1550	2.6°C	17.2°C
10%	1550	19.8°C	2.1°C
5%	1520	38.1°C	12.1°C
5%	1530	23.7°C	36.3°C
5%	1570	3.2°C	27.4°C

the middle of the feasible perfect rotation region, depicted in Fig. 3.11-b, maximizing the range of compensable θ_R variations. Tunable polarization phase-shifters use the same the transversal geometry as input and output waveguides. In these waveguides the TE mode is mainly confined within the silicon waveguide core, which has a positive thermo-optical coefficient while the TM mode strongly senses the SU8 cladding, which has a negative thermo-optical coefficient. Hence, effective index variation with temperature is largely different for TE and TM modes, with calculated values of

$$\begin{aligned} \frac{\mathrm{d}n_{\text{eff}}^{TE}}{\mathrm{d}T} &= 1.7 \times 10^{-4}\,{}^{\circ}\mathrm{C}^{-1} \\ \frac{\mathrm{d}n_{\text{eff}}^{TM}}{\mathrm{d}T} &= 1.1 \times 10^{-4}\,{}^{\circ}\mathrm{C}^{-1} \end{aligned} \tag{3.15}$$

This way, polarization phase-shift can be tuned changing temperature as

$$\rho = L_P \frac{2\pi}{\lambda}\left(n_{\text{eff}}^{TE} - n_{\text{eff}}^{TM}\right) + L_P \frac{2\pi}{\lambda}\left(\frac{\mathrm{d}n_{\text{eff}}^{TE}}{\mathrm{d}T} - \frac{\mathrm{d}n_{\text{eff}}^{TM}}{\mathrm{d}T}\right)\Delta T, \tag{3.16}$$

being λ the wavelength and L_P the length of the polarization phase-shifters. Polarization phase-shifter lengths are set to $L_P = 700\,\mu\mathrm{m}$ to be able to tune ρ_i over 360° with temperature increments $\Delta T < 40°\mathrm{C}$. Compact footprint and lower consumption can be achieved spiralling shifter waveguides [84].

Fully compensation of fabrication errors between $\Delta G = -7.5\,\%$ to $\Delta G = +10\,\%$ are shown in Fig. 3.13-a for the tunable rotator scheme with extinction ratios better than $40\,\mathrm{dB}$. The temperatures increments in the polarization phase shifters required for compensation (ΔT_1, ΔT_2 in table 3.1) can be found through iteration or using an optimization algorithm. For $\Delta G = -10\,\%$ (point A) the rotator waveguide parameters are $\theta = 15.5°$ and $\phi = 74°$, and thus lay outside the region that can be fully compensated (Fig. 3.11-b). However the extinction ratio is still improved compared to the conventional design.

The proposed scheme furthermore allows for re-tuning of the device to an arbitrary wavelength, as long as eq. (3.12) holds for this particular wavelength. Figure 3.13-b shows extinction ratio as a function of the wavelength when a device with an error of $\Delta G = +5\,\%$ is tunned to be centered at $\lambda = 1520\,\mathrm{nm}$, $\lambda = 1530\,\mathrm{nm}$, $\lambda = 1550\,\mathrm{nm}$ and $\lambda = 1570\,\mathrm{nm}$. Required temperature changes are described in Table 3.1. In every case extinction ratios in excess of $40\,\mathrm{dB}$ are achieved.

Polarization phase-shifts ρ_1 and ρ_2 vary with wavelength as

$$\rho = L_P \frac{2\pi}{\lambda}\left(n_{\text{eff}}^{TE} - n_{\text{eff}}^{TM}\right) + L_P \frac{2\pi}{\lambda}\left(\frac{\mathrm{d}n_{\text{eff}}^{TE}}{\mathrm{d}\lambda} - \frac{\mathrm{d}n_{\text{eff}}^{TM}}{\mathrm{d}\lambda}\right)\Delta\lambda, \tag{3.17}$$

limiting scheme bandwidth. Then, considering eq. (3.16) and (3.17) it can be concluded that the design of tunable polarization phase-shifter length faces a bandwidth-power trade-off. This is, longer phase-shifters can provide 360° tunability for reduced temperature variations (and thus reduced power consumption) at the price of a narrow bandwidth.

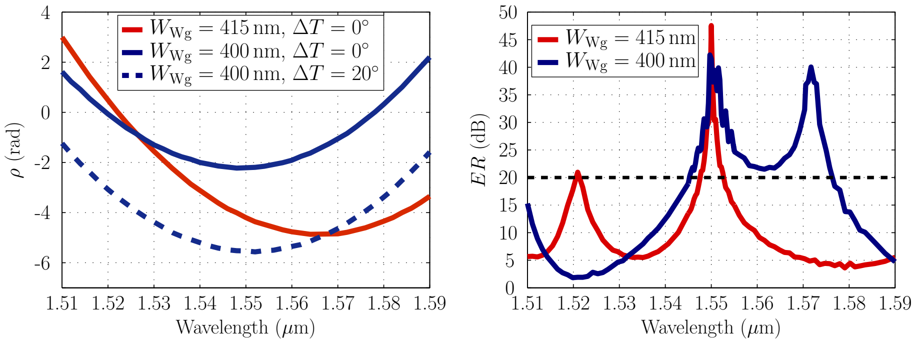

a)

b)

Figure 3.14.: a) Calculated polarization phase-shift (ρ) as a function of wavelength for various waveguide widths and temperature changes for $L_P = 700\,\mu\mathrm{m}$. **b)** ER as a function of wavelength for polarization phase-shifters of widths $W_{\mathrm{Wg}} = 415\,\mathrm{nm}$ and $400\,\mathrm{nm}$.

Nevertheless, polarization phase-shift variation with wavelength is strongly dependent on waveguide width. Figure 3.14-a shows calculated ρ for various waveguide widths and temperature increments. It can be seen that ρ has a parabolic-like shape. ρ variation is minimized around the parabola vertex, whose position is mainly determined by the waveguide width. Although a further research is still required, this effect could in principle be used to increase the rotator bandwidth keeping the same polarization phase-shifter length (and power consumption). As an example, Fig. 3.14-b compares ER for the proposed tunable rotator when polarization phase-shifters with length of $L_P = 700\,\mu\mathrm{m}$ and waveguide widths of $W_{\mathrm{Wg}} = 415\,\mathrm{nm}$ (the same as in Fig. 3.13), and $W_{\mathrm{Wg}} = 400\,\mathrm{nm}$ are used. The device with optimized waveguide width provides an ER better than $20\,\mathrm{dB}$ in a $\sim 30\,\mathrm{nm}$ bandwidth.

Conclusions

A novel tunable rotator scheme is proposed that enables dynamic central wavelength selection and substantially improves device tolerance compared to conventional integrated polarization rotators. This scheme uses two polarization phase-shifters, that can be realized with simple waveguide heaters, to efficiently compensate errors arising from fabrication imperfections, overcoming the practical limitations of existing integrated polarization rotators. Proposed scheme opens the path for the monolithic integration of high performance and high yield rotators in polarization diversity and polarization multiplexing optical circuits.

3.3. PBS-Less Dual-Polarization Coherent Receiver

Conventional architectures for dual-polarization coherent receivers can be divided in three functional networks: polarization diversity, phase diversity and power detection [131]. Phase diversity and power detection networks, duplicate the single polarization downconverter architecture, i.e a 90° hybrid followed by four high speed photodiodes, to handle separately incoming orthogonal polarizations. Polarization diversity network uses one or two polarization beam splitters (PBS) to feed each downconverter with a different polarization. Opto-electronically converted outputs are analyzed in the digital signal processing (DSP) module to retrieve the original (phase and amplitude) information carried by each polarization component.

Integrated PBS exhibit stringent fabrication tolerances [135, 136], that compromise performance and yield, requiring of power consuming tunning techniques to enable monolithic integration in dual-polarization receivers [132, 133]. For that reason, off-chip implementation of the polarization diversity network is preferred in commercial devices [60]. A further confirmation of this trend, is the fact that the Internetworking Forum (OIF) established as non-mandatory the monolithic integration of the polarization diversity network [131].

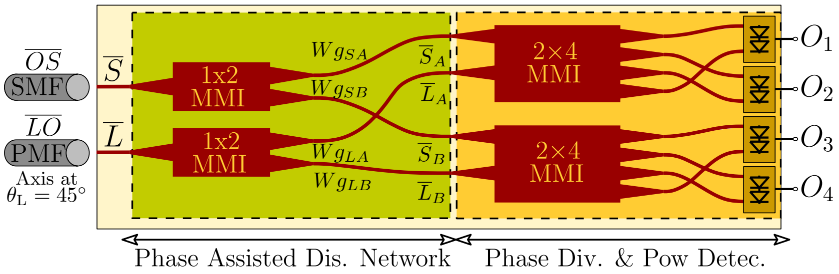

Figure 3.15.: Schematic representation of proposed PBS-less dual-polarization coherent receiver.

Proposed Receiver: Architecture and Design

To avoid the need of PBS (and their tolerance limitations) in monolithically integrated dual-polarization coherent receivers, an alternative architecture is proposed that substitutes the polarization diversity network by a phase-assisted distribution network, keeping conventional phase diversity and power detection networks, and DSP algorithms unchanged.

Proposed receiver implementation is schematically depicted in Fig. 3.15. The phase-assisted distribution network is composed of two 1×2 multimode interference couplers

(MMI), that act as polarization insensitive power splitters (PS), and four birefringent waveguides, Wg_{S_A}, Wg_{S_B}, Wg_{L_A}, Wg_{L_B}, with identical cross-section. Waveguide lengths are designed to introduce four specific phase-shifts between orthogonal polarization components of signal and local oscillator. The phase diversity and power detection networks are composed of two 2×4 MMI (designed to be almost polarization independent), and four pairs of balanced photodetectors.

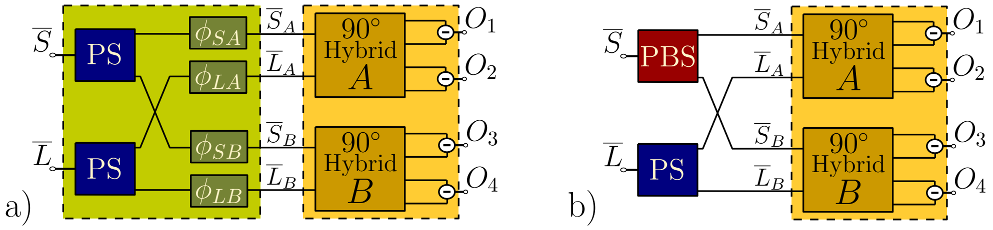

Figure 3.16.: Block diagram describing dual-polarization coherent receiver based on **a)** proposed PBS-less approach, and **b)** conventional PBS-based approach.

To illustrate the working principle of the proposed PBS-less architecture, the behavior of the ideal scheme shown in Fig. 3.16-a is analyzed. This phase-assisted distribution network is composed of two 3 dB power splitters (PS), and four polarization phase-shifters that introduce a ϕ phase difference between both polarization components. The phase-diversity and power detection networks are similar to those of the conventional PBS-based approach depicted in Fig. 3.16-a, i.e. comprise two 90° hybrids and four pairs of balanced photodetectors. As an example, in the following discussion phase-shifts of the first three paths are set to zero (i.e. $\phi_{SA} = \phi_{LA} = \phi_{SB} = 0°$), and the last one is set to $\phi_{LB} = 180°$. The received symbols ($\overline{S}$) and local oscillator ($\overline{L}$) in this ideal scheme are defined as

$$\overline{S} = \begin{bmatrix} I^{TE} + jQ^{TE} \\ I^{TM} + jQ^{TM} \end{bmatrix} \tag{3.18}$$

$$\overline{L} = \begin{bmatrix} L^{TE} \\ L^{TM} \end{bmatrix} = \begin{bmatrix} LO\ \cos(\theta_L) \\ LO\ \sin(\theta_L) \end{bmatrix}, \tag{3.19}$$

where I^{TE}, Q^{TE}, I^{TM}, Q^{TM} are the received symbols, L^{TE}, L^{TM} are the two polarization components of the local oscillator and θ_L is the LO injection angle of the polarization maintaining fiber axis (see Fig. 3.15). As in conventional PBS-based receivers, θ_L is adjusted to 45° in order to excite both LO polarization components in the same amount ($L^{TE} = L^{TM}$). This way, the phase-assisted distribution network generate the following four outputs, that are injected into the phase assisted distribution network:

$$\begin{aligned}\overline{S}_A &= 1/\sqrt{2}\cdot\begin{bmatrix} I^{TE}+jQ^{TE} \\ I^{TM}+jQ^{TM}\end{bmatrix} \\ \overline{S}_B &= 1/\sqrt{2}\cdot\begin{bmatrix} I^{TE}+jQ^{TE} \\ I^{TM}+jQ^{TM}\end{bmatrix} \\ \overline{L}_A &= 1/\sqrt{2}\cdot\begin{bmatrix} L^{TE} \\ L^{TM}\end{bmatrix} \\ \overline{L}_B &= 1/\sqrt{2}\cdot\begin{bmatrix} L^{TE} \\ -L^{TM}\end{bmatrix}.\end{aligned} \tag{3.20}$$

Note that, the $\phi_{LB} = 180°$ phase-shift yields a minus sign in the L^{TM} component in $\overline{L}_B$. Then, the four output photocurrents generated by this ideal model, O_{1-4} in Fig. 3.16-a, are found to be

$$\begin{bmatrix} O_1 \\ O_2 \\ O_3 \\ O_4 \end{bmatrix} = K\cdot\begin{bmatrix} 1 & 0 & 1 & 0 \\ 0 & 1 & 0 & 1 \\ 1 & 0 & \text{-}1 & 0 \\ 0 & 1 & 0 & \text{-}1 \end{bmatrix}\cdot\begin{bmatrix} I^{TE} \\ Q^{TE} \\ I^{TM} \\ Q^{TM} \end{bmatrix} = \overline{\overline{M}}\cdot\begin{bmatrix} I^{TE} \\ Q^{TE} \\ I^{TM} \\ Q^{TM} \end{bmatrix}, \tag{3.21}$$

where K is a constant that takes into account the responsivity of the photodiodes, the insertion losses of the 90° hybrids and power splitters, etc.

The matrix $\overline{\overline{M}}$, that relates received symbols and output photocurrents, is orthogonal. Hence, received I^{TE}, Q^{TE}, I^{TM}, Q^{TM} can be retrieved in the DSP using the same constant modulus algorithm (CMA) [143] used to solve the polarization rotation introduced by the fiber in conventional receivers. This result shows that dual-polarization demodulation can be performed obviating the need of polarization beam splitters or rotators.

Dual-polarization demodulation provided by this particular configuration ($\phi_{SA} = \phi_{LA} = \phi_{SB} = 0°$ and $\phi_{LB} = 180°$) can be performed using a wide variety of polarization phase-shift configurations. Defining the differential phase-shift, ϕ_{Dist}, as

$$\phi_{Dist} = (\phi_{SA} - \phi_{LA}) - (\phi_{SB} - \phi_{LB}), \tag{3.22}$$

it can be found that any polarization phase-shift combination in the phase-assisted distribution network fulfilling the following condition

$$\phi_{Dist} = (2p+1)\cdot 180°, \;\; p = 0, 1, ... \tag{3.23}$$

yields an orthogonal matrix similar to (3.21), providing the desired receiver behavior.

To assess the validity and robustness of condition (3.23), PBS-less architecture performance is compared with that of a conventional PBS-based receiver, considering a realistic scenario.

The author wants to acknowledge **Diego Pérez-Galacho** and **Pedro J. Reyes-Iglesias**, our colleges in the Photonics & RF group at the Universidad de Málaga, for performing the electromagnetic modeling and design of the MMIs and the system-level simulations discussed below.

Different elements of this realistic simulation scenario are modeled as:

- Input: The fiber is modeled as an additive Gaussian noise (AWGN) channel degraded by amplified spontaneous emission (ASE) noise. Random fiber birefringence changes are modeled scrambling state of polarization of the signal at the receiver input. 112 Gb/s dual-polarization QPSK signals, with a received signal power of -20 dBm and LO power of 5 dBm, are considered.

- Phase diversity network: The ideal 90° hybrids are substituted by the same high performance InP/InGaAsP 2x4 MMI couplers used in previous works to characterize the sensitivity of a single-polarization coherent receivers to fabrication errors [144] and to implement a PBS-based dual-polarization coherent receiver with active tuning [133]. Two different MMI designs are considered: i) nominal design, that exhibits a Maximum Amplitude Imbalance $\mathrm{MAI} = 0.6$ dB and a Maximum Phase Imbalance $\mathrm{MPI} = 0.4^\circ$ within the C-band (1530 nm-1570 nm), and ii) detuned design, where moderate fabrication errors are considered, that exhibits a $\mathrm{MAI} = 2.7$ dB and a $\mathrm{MPI} = 2^\circ$.

- Power detection network: photodiodes are modeled as an square-law detector with additive shot noise, and TIA's are modeled with an input referred noise current density of $20\,\mathrm{pA}/\sqrt{\mathrm{Hz}}$.

- DSP: ADCs and DSP blocks are assumed ideal. Only standard Gram-Schmidt orthogonalization procedure (GSOP) [145] and constant modulus algorithm (CMA) [143] are used (please refer to [144] for details).

Both, conventional and PBS-less architectures are modeled using these blocks. The polarization diversity network of the PBS-based receiver is modeled using an ideal PBS and an ideal PS. Phase-assisted distribution network in the PBS-less receiver is modeled using two ideal PS. In order to analyze the effect of deviations from the ideal phase condition, a differential phase error, ε_ϕ, is defined as

$$\varepsilon_\phi = \phi_{Dist} - 180^\circ. \tag{3.24}$$

Receiver penalty, $P\,(\mathrm{dB})$, is defined as

$$P\,(\mathrm{dB}) = OSNR_{\mathrm{PBSless}} - OSNR_{\mathrm{Conv}}, \tag{3.25}$$

where $OSNR_{\mathrm{PBSless}}$ and $OSNR_{\mathrm{Conv}}$ are the Optical Signal-to-Noise Ratio required for a BER=10^{-3} for the PBS-less and conventional receivers, respectively.

Receiver penalty, $P\,(\mathrm{dB})$, is calculated for the nominal and detuned MMIs at the end of the C-band (1570 nm wavelength), as a function of the differential phase-shift error ε_ϕ, as shown in Fig. 3.17. Extensive simulations are performed, where polarization state at the receiver input is randomly scrambled for each ε_ϕ point. Solid lines show worst case, and dashed lines show smoothed curves, that eliminate the ripple associated to a finite number of realizations. It is shown that both architectures are equivalent when condition (3.23) is met ($\varepsilon_\phi = 0$). PBS-less receiver can handle variations of $|\varepsilon_\phi| < 40^\circ$ with a penalty below $0.4\,\mathrm{dB}$ for both, nominal and detuned, MMI designs.

To evaluate tolerance of the proposed scheme to fabrication errors, differential phase-shift errors (ε_ϕ) are analyzed for a phase-assisted distribution network implemented with

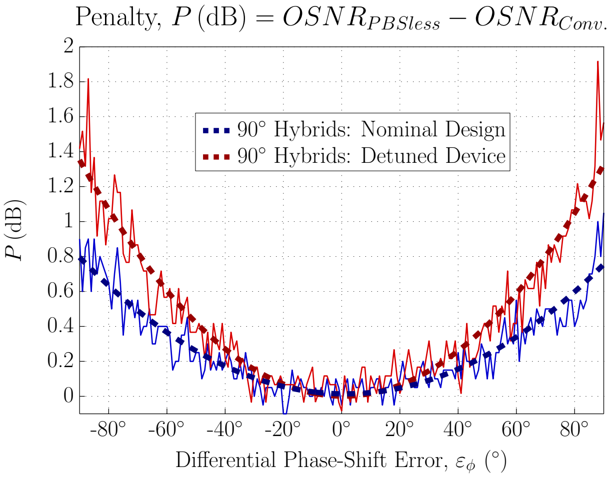

Figure 3.17.: Penalty of the PBS-less approach, defined in eq. (3.25), as a function of the differential phase-shift error, ε_ϕ, defined in eq. (3.24).

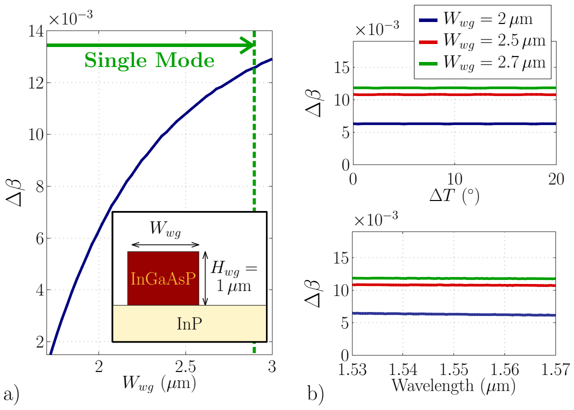

Figure 3.18.: Birefringence $\Delta\beta$ of a fully etched InP/InGaAsP waveguide (see inset) as a function of **a)** the width, **b)** the temperature increment (ΔT), and **c)** the wavelength.

the same conventional strip InP/InGaAsP waveguides (see inset in Fig. 3.18-a) previously used to implement a monolithically integrated PBS-based dual-polarization coherent receiver with active tuning [133].

As a first step of the tolerance analysis, waveguide birefringence, defined as

$$\Delta\beta = \beta^{TE} - \beta^{TM}, \tag{3.26}$$

is calculated as a function of the waveguide width using the commercial 3-D full-vectorial mode solver Fimmwave. As it is observed in Fig. 3.18-a, wider waveguides are preferred, since they provide higher birefringence and lower sensitivity to width errors. Figures 3.18-b and 3.18-c, show that birefringence sensitivity to temperature and wavelength is negligible compared to waveguide width. Epitaxial growth of InP/InGaAsP layers is very accurate [136], and InP substrate acts as stop layer obviating etching deviations in waveguide definition. Hence the most critical parameter affecting birefringence is waveguide width. Nominal waveguide width is set to $W_{wg}^{Nom} = 2.7\,\mu\text{m}$, in order to optimize device performance ensuring single-mode behavior ($W_{wg} < 2.8\,\mu\mathrm{m}$).

Given that all waveguides have the same nominal width, polarization phase-shift introduced by each path in the phase-assisted distribution network is optimized adjusting waveguide length (l) as

$$\phi = \Delta\beta \cdot l. \tag{3.27}$$

Waveguide lengths are set to $l_{SA} = l_{SB} = 800\,\mu\mathrm{m}$, $l_{LA} = 932.5\,\mu\mathrm{m}$ and $l_{LB} = 667.5\,\mu\mathrm{m}$, in order to minimize the size of the phase-assisted distribution network, meeting a minimum bending radii of $600\,\mu\mathrm{m}$.

To evaluate the tolerance of the proposed design, waveguide width in presence of fabrication errors is defined as

$$W_{wg} = W_{wg}^{Nom} + \varepsilon_W, \tag{3.28}$$

where W_{wg}^{Nom} is the nominal waveguide width and ε_W accounts for waveguide width variations. Two kind of width variations are considered:

- Common width error, i.e. all waveguides deviate in the same amount.
- Differential width error, i.e. deviation differs in each waveguide.

Note that typical with errors in this technology are below $\pm 200\,\mathrm{nm}$ and $\pm 40\,\mathrm{nm}$ for the common and differential cases, respectively [136, 146].

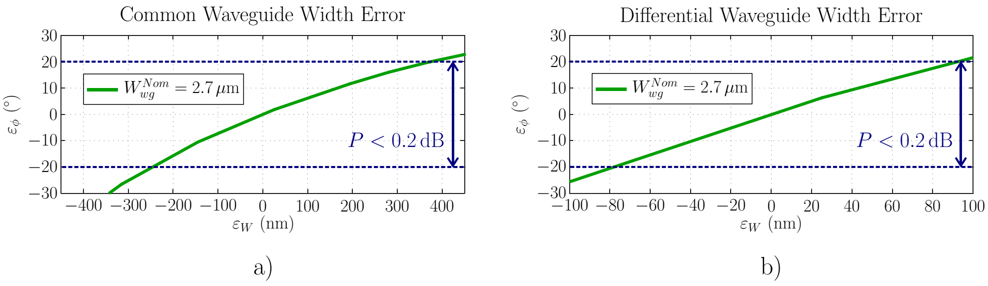

Figure 3.19.: Differential phase-shift error ε_ϕ as a function of the waveguide width deviation ε_W, considering **a)** common width errors, and **b)** differential width errors.

Figure 3.19 shows calculated differential phase-shift error, ε_ϕ, as a function of common and differential (only the width of the longest waveguide, Wg_{L_A}, changes) waveguide width deviations, produced in proposed phase-assisted distribution network. Differential phase-shift errors below $|\varepsilon_\phi| < 20°$ can be ensured for waveguide width variations as large as $\pm 250\,\mathrm{nm}$ and $\pm 80\,\mathrm{nm}$ for the common and differential cases, respectively. Using Fig. 3.17 as a look-up table, ε_ϕ can easily be translated to receiver penalty, $P\,(\mathrm{dB})$, observing that proposed PBS-less receiver exhibits negligible degradation ($P < 0.2\,\mathrm{dB}$) for typical waveguide width errors. This is a substantial tolerance improvement, compared to passive PBS-based receivers in this technology that exhibit a waveguide width tolerance of around $\pm 10\,\mathrm{nm}$ [133].

Conclusions

In summary, a novel PBS-less dual-polarization integrated coherent receiver has been proposed, that can be easily implemented using conventional InP/InGaAsP waveguides. PBS-less receiver substitutes polarization diversity network by a phase-assisted distribution network that substantially improves device tolerance to fabrication errors. These results are of particular importance for next generation commercial monolithic dual-polarization transceivers, which require robust and cost-effective architectures that obviate the need of active tunning.

4

Conclusions and Prospects

A wide variety of devices have been discussed in the previous chapters, that include grating couplers, polarization rotators and dual-polarization coherent receivers. In this chapter, these designs are reviewed pointing out which problem is faced and what solutions have been proposed in each case. Besides, other contributions developed during the thesis, that have not been included in this manuscript, are briefly summarized. Finally, research activities planned to conclude or extend the work presented in this thesis are discussed.

4.1. Conclusions

A. Grating Couplers for Micrometric SOI Rib Waveguides

Grating couplers are considered as an essential building-block of next generation large scale silicon photonic platform as they are able to provide wafer-scale testing functionality with relaxed alignment tolerances and competitive insertion loss [11]. In fact, they are already the preferred solution for the implementation of chip interconnects (chip-to-fiber, chip-to-chip) in many Si-wire applications [11,24,25,147,148]. On the other hand, low loss bending radii of only $10\,\mu\mathrm{m}$ have recently been demonstrated for $4\,\mu\mathrm{m}$ thick SOI waveguides [43], overcoming the traditional integration density limitation of micrometric SOI waveguides. In this scenario, developing high-efficiency grating couplers for the micrometric SOI platform becomes highly attractive as it may add wafer-scale testing capability to this low-loss and low-birefringence technology.

Grating Coupler for Chip-to-Fiber Interconnects

The problem There are two main differences between Si-wire and micrometric gratings that hinder the implementation of grating couplers in the micron-scale platform:

- Si-wire gratings are vertically monomode. On the contrary, due to their larger thickness, grating couplers in micrometric waveguides are vertically multimode. Excitation of these multiple modes may produce several radiation beams (propagating with different angles) substantially reducing coupling efficiency.

- Si-wire gratings work with pitches short enough to be within the single ($k = -1$) harmonic region. Minimum manufacturable pitch with standard micrometric platform fabrication process (i-line stepper) falls outside this region. Working in the higher order harmonic range is conventionally associated to multi-beam radiation and low coupling efficiency.

Proposed solution Two are the solutions that have been proposed, for the first time to our knowledge, to overcome the aforementioned limitations:

- The use of an inverse taper between the interconnection waveguide and the grating, that maximizes matching between excitation field and fundamental mode of the grating. This way, single-mode excitation is ensured and back-reflections are minimized.
- Development of design conditions to provide single-beam radiation within the higher order harmonic region. This way, high efficiency grating couplers can be designed with larger dimensions compatible with i-line stepper fabrication.

Coupling to a standard single-mode fiber SMF-28 with $-2.2\,\mathrm{dB}$ efficiency has been experimentally demonstrated using an inverse taper and an uniform grating pitch working with the $k = -2$ harmonic order [63]. Devices have been fabricated using i-line stepper lithography and reactive ion etching, with a single etch step for the interconnection waveguides, inverse taper and grating region. Grating teeth optimization (etch depth, duty cycle and pitch) provided a remarkably large directionality of $\eta_{\mathrm{Up}} \sim 0.9$, without the need of any overlay or bottom reflectors [61].

Polarization Independent Grating Coupler

The problem In applications where non polarization maintaining fibers are used as an input, polarization state arriving to the coupler is most of the times unknown. Thus, in order to avoid unwanted power loss, it would be desirable to have polarization independent grating couplers. Unfortunately, radiation angle, and directionality of grating couplers is largely determined by the effective index of the mode propagating through them, and thus strongly polarization dependent. Due to the lower birefringence of micrometric waveguides, radiation angle difference between TE an TM polarizations is reduced to about 5° in micron-scale gratings. However, directionality is still strongly polarization dependent, hindering the implementation of polarization independent grating couplers.

Proposed solution To achieve a large directionality for both polarizations simultaneously, a thin metal layer has been used to implement a bottom mirror. While in most bottom-mirror-based gratings, mirror position is adjusted to provide constructive interference with the power radiated up by an optimized (and fixed) grating design, in this case, mirror position is fixed, and grating design is adjusted to provide required constructive interference with the power reflected up by the mirror. In doing so, the metal layer can be deposited just underneath BOX layer, using SiO_2 as etch stop layer for selective Si substrate removal. This solution simplifies the fabrication process and alleviates stringent mirror position tolerances. Optimized grating coupler with a thin gold layer mirror under a $1\,\mu\mathrm{m}$ BOX exhibits a calculated coupling efficiency of $CE = -3\,\mathrm{dB}$ for both polarizations [69].

Grating Coupler for Spectrometer

The problem Performance of integrated spectrometers is closely related to their light collection capacity. This way, multi-aperture Fourier Transform spectrometer (FTS) benefits form the increased throughput, compared to single-aperture solutions, provided by the use of variety of input apertures [122]. However, when conventional edge couplers are used as input apertures, light collection area is restricted to a line along the chip facet, limiting the ability to cover arbitrarily shaped input beams. The National Research Council in Canada, the company ComDev and the Canadian Space Agency had developed an integrated FTS, based on micrometric SOI waveguides, to monitor water vapor absorption in the atmosphere from an Earth satellite [71, 72]. Input beam generated by the optic system has a circular shape, limiting light collection efficiency of edge-coupler-based solutions.

Proposed solution Grating couplers can be placed anywhere in the chip surface, obviating edge couplers limitation, and potentially allowing to implement a much larger (and arbitrarily shaped) light collection area. Inverse taper and higher order harmonic radiation have been used to design high efficiency grating couplers compatible with the micrometric waveguides used to implement the FTS. The design has been optimized for $1354\,\mathrm{nm}$ wavelength, as it corresponds to the peak water absorption. A $90\,\mu\mathrm{m}$ x $90\,\mu\mathrm{m}$ light collection area was implemented with a grating coupler array, composed by six $15\,\mu\mathrm{m}$ x $90\,\mu\mathrm{m}$ couplers, that exhibits a measured coupling efficiency of $-4.5\,\mathrm{dB}$ at $1354\,\mathrm{nm}$ wavelength [72].

B. Integrated Polarization Rotators

Development of robust and easy-to-fabricate integrated polarization rotators is pursued by many research groups, as it holds the promise of improved performance, reliability, cost and yield in monolithically integrated dual-polarization transceivers. Besides, any device relaying in a polarization diversity approach would also benefit from such devices.

Polarization Rotator for InP Waveguides

The problem The preferred solution for the implementation of integrated polarization rotators in the InP platform is the slanted waveguide [51–53]. Transversal geometry of this rotator waveguide has a deeply etched straight wall, and a slanted wall. On the other hand, conventional interconnection rib waveguides have two shallowly etched straight walls. Therefore, the integration of slanted rotators and interconnection waveguides requires three etch steps: one dry (shallow) etch step for the interconnection waveguides, one dry (deep) etch step for the straight rotator wall, and one wet etch step for the slanted rotator wall. Each extra processing step increases device fabrication complexity, adding new error sources, and negatively affecting device yield and cost.

Proposed solution In order to minimize the number or processing steps, an alternative rotator waveguide geometry has been proposed that avoids the need of the wet etch step. In the proposed rotator, the slanted wall is substituted by a two steps profile. This geometry can be understood as a first order approximation of the slanted wall, that can support (when properly designed) the hybrid modes required to provide polarization rotation. The integration of the rotator with rib interconnection waveguides requires only two dry etch steps: one shallow for interconnection waveguides and first rotator step, and one deep for second rotator step. A two-steps rotator waveguide has been designed to be fully compatible with a previously developed monolithically integrated single-polarization downconverter, i.e. rotator uses the same waveguide thickness and the same shallow etch depth used in the receiver. Optimized rotator exhibits a calculated extinction ratio of $40\,\mathrm{dB}$ [75].

Tunable Polarization Rotator Scheme

The problem Besides the sometimes complex fabrication process, the main drawback of conventional polarization rotators is related to their stringent fabrication tolerances that seriously compromise their performance and yield. Rotator waveguides relay on a very precise waveguide transversal geometry to provide hybrid mode tilt angle and polarization phase-shift required to provide polarization rotation. These two parameters are strongly affected by slight deviations in waveguide dimensions, with extinction ratios falling below $5\,\mathrm{dB}$ for deviations of only $5\,\%$ in waveguide transversal dimensions.

Proposed solution A novel polarization rotator scheme has been proposed, that substantially improves tolerances to fabrication errors. The scheme is composed by three rotator waveguide sections interconnected by two tunable polarization phase-shifters. By controlling the phase-shifters, that can be implemented with simple waveguide heaters, deviations in the dimensions of rotator waveguide sections can be compensated, providing perfect rotation in presence of fabrication errors [77]. Furthermore, the proposed scheme allows to dynamically select rotator central wavelength. Conditions for perfect rotation (i.e. polarization conversion efficiency of $PCE = 1$) are analytically derived, showing that it can be achieved for deviations as large as $\pm 60\,\%$ in the hybrid mode tilt angle and polarization phase-shift.

C. PBS-Less Dual-Polarization Coherent Receiver

The problem Commercial dual-polarization coherent receivers duplicate the already existing monolithically integrated single polarization downconverter, and use a bulk polarization beam splitter (PBS) to feed each downconverter with a different polarization component. Although integration of the PBS together with the downconverters would improve device reliability, compactness, and ultimately cost, due to the stringent fabrication tolerances of integrated PBS, this functionality is still implemented off-chip. Receivers that monolithically integrate the PBS, require the implementation of (power consuming) active tunning techniques to compensate fabrication errors.

Proposed solution An innovative dual-polarization coherent receiver architecture has been proposed that avoids the need of polarization beam splitters or rotators, thus avoiding intrinsic tolerance limitations of these polarization handling elements. Polarization management is instead achieved by adequately engineering the birefringence of the interconnecting waveguides. The resultant receiver is highly tolerant to fabrication deviations. Electromagnetic and system level simulations show a negligible performance degradation for waveguide width errors of $\pm 200\,\mathrm{nm}$. This PBS-less approach opens a completely new route for monolithic integration of dual-polarization receivers without any type of active tuning.

4.2. Other Contributions

Together with the Politecnico di Milano higher order dual-mode filters have been developed. The contradirectional coupling produced by a partial reflector introduced in the last ring of a coupled resonator structure is used to double effective filter order, resulting in a structure with reduced sensitivity to fabrication tolerances [149, 150].

During his thesis, the PhD student has also collaborated in:

- Analysis of Si-wire polarization rotator based on a double sub-wavelength trench [56, 151].
- Design of integrated polarization beam splitters for InP dual-polarization coherent receivers [133, 136].
- Experimental characterization of an MMI that uses a sub-wavelength trench to halve device length without affecting its performance [152, 153].

4.3. Prospects

Results derived from this thesis encourage the Photonics & RF group at the Universidad de Málaga to continue research in these fields. Some of the development prospects regarding grating couplers, polarization rotators and dual-polarization coherent receivers are detailed below

Grating Couplers

First step planned in this field is applying the experience and design techniques developed for micron-scale grating couplers to the implementation of high-efficiency chip-to-fiber grating couplers for the SOI platform with sub-micrometer Si thickness (typically 220nm - 300 nm). Demonstrated single-beam radiation in higher order grating harmonics enables the use of larger dimensions, and thus may improve device tolerance to fabrication errors. On the other hand, the use of various customized etch depths in the grating region has been proposed to substantially increase grating directionality in the upwards direction, avoiding the need of bottom mirrors [34, 39]. Preliminary results show that this same effect can be achieved with minimum feature size and etch depths typically used in silicon photonic foundries, easing fabrication complexity. In the mid term, the possibility to implement chip-to-chip grating couplers for the next-generation photonic interconnects technology will also be analyzed.

Polarization Rotators

Most exciting prospect in this field is the experimental demonstration of the tunable rotator scheme. First prototypes, that have been fabricated in the facilities of Université Paris Sud, are being now characterized in the Universidad de Málaga. Besides, the extension of the proposed scheme to provide polarization transformations covering the complete Poincaré sphere, is expected to yield very interesting results. In a longer term, tunable phase-shifters are planned to be further optimized to provide larger operation bandwidth and/or reduced power consuming. Special attention will be dedicated to analyze the possibility to use the sub-wavelength dispersion engineering techniques previously developed in the group [154, 155].

Dual-Polarization Coherent Receivers

In the short term, the analysis of different waveguide geometries that might further improve device tolerances to fabrication errors, is planned. In the mid term, it is expected to develop a proof-of-concept prototype that can experimentally validate the proposed scheme.

Appendices

A

Appendices

A.1. Tunable Polarization Rotator Scheme: Perfect Rotation Condition

In this section, conditions for perfect TE to TM polarization rotation are derived for the proposed tunable polarization rotator scheme (described in 3.2.2), based on the analysis of the Jones matrices of the different elements composing the rotator. Derived conditions are also valid for TM to TE polarization rotation.

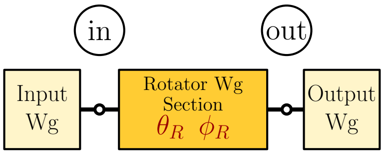

Figure A.1.: Block diagram of a single-section rotator waveguide.

Let us consider the single-section rotator waveguide schematically depicted in Fig. A.1. Polarization states at the input (A_{in}) and output (A_{out}) of the rotator are related as

$$\begin{bmatrix} A_{out}^{TE} \\ A_{out}^{TM} \end{bmatrix} = \left[J_R \left(\theta_R, \phi_R \right) \right] \cdot \begin{bmatrix} A_{in}^{TE} \\ A_{in}^{TM} \end{bmatrix}, \tag{A.1}$$

being $A_{in,out}^{TE}$ and $A_{in,out}^{TM}$ the complex amplitudes in the TE and TM components, and $J_R \left(\theta_R, \phi_R \right)$ the Jones matrix of a rotator waveguide defined in eq. (3.7), repeated here for the sake of clarity

$$J_R \left(\theta_R, \, \phi_R \right) = \begin{bmatrix} e^{(j\phi_R)} cos^2(\theta_R) + sin^2(\theta_R) & \frac{e^{(j\phi_R)}-1}{2} sin(2\theta_R) \\ \frac{e^{(j\phi_R)}-1}{2} sin(2\theta_R) & cos^2(\theta_R) + e^{(j\phi_R)} sin^2(\theta_R) \end{bmatrix}. \tag{A.2}$$

An arbitrary input polarization state is considered, defined as

$$A_{in} = \begin{bmatrix} A_{in}^{TE} \\ A_{in}^{TM} \end{bmatrix} = \begin{bmatrix} a e^{j\rho} \\ \sqrt{1-a^2} \end{bmatrix}, \tag{A.3}$$

with a the modulus of the TE amplitude and ρ the phase difference between the TE and TM components. Then, power in the TM component at the output of the rotator (P_{out}^{TM}) can be calculated as

$$\begin{aligned} P_{out}^{TM} &= \left|A_{out}^{TM}\right|^2 \qquad (A.4) \\ &= \left|ae^{j\rho}\left(e^{j\phi_R}-1\right)sin(2\theta_R)/2+\sqrt{1-a^2}\left(cos^2(\theta_R)+e^{j\phi_R}sin^2(\theta_R)\right)\right|^2. \end{aligned}$$

P_{out}^{TM} can be rewritten as

$$P_{out}^{TM} = \left[a\cdot\alpha_R+\sqrt{1-a^2}\cdot\gamma_R\cdot\sin\left(\rho+\phi_R/2\right)\right]^2, \qquad (A.5)$$

being the parameters α_R and γ_R dependent on the characteristic parameters of the rotator waveguide (θ_R, ϕ_R) as defined in eq. (3.13) repeated here for clarity

$$\begin{aligned} \alpha_R &= \sin(2\theta_R)\cdot\sin(\phi_R/2) \qquad (A.6) \\ \gamma_R &= \sqrt{\cos^4(\theta_R)+\sin^4(\theta_R)+2\cdot\cos^2(\theta_R)\cdot\sin^2(\theta_R)\cdot\cos(\phi_R)} \end{aligned}$$

Then, for a given rotator waveguide section (fixed θ_R and ϕ_R), P_{out}^{TM} varies as a function of ρ, being its maximum and minimum values, when $\sin\left(\rho+\phi_R/2\right)=\pm1$, given by

$$\begin{aligned} P_{out_{Max}}^{TM} &= \left[a\cdot\alpha+\sqrt{1-a^2}\cdot\gamma\right]^2 \qquad (A.7) \\ P_{out_{min}}^{TM} &= \left[a\cdot\alpha-\sqrt{1-a^2}\cdot\gamma\right]^2 \end{aligned}$$

Note that maximum and minimum achievable P_{out}^{TM} depend on θ_R, ϕ_R and a, but not on ρ, i.e. range of possible output powers in TM (and thus on TE) polarization is determined by the rotator waveguide section and the ratio between the amplitudes in the input TE and TM components (but not on their relative phase). The actual P_{out}^{TM} inside that feasible range is determined by the relative phase between the input TE and TM components, ρ, that determines the value of $\sin\left(\rho+\phi_R/2\right)=\pm1$.

If TM polarized output light ($P_{out}^{TE}=0$ and $P_{out}^{TM}=1$) is aimed, then maximum power in TM should be $P_{out_{Max}}^{TM}=1$ that can be achieved if

$$a=\alpha_R \Leftrightarrow \sqrt{1-a^2}=\gamma_R \qquad (A.8)$$

If we define ρ^{opt} as the phase that makes $P_{out}^{TM}=P_{out_{Max}}^{TM}$, then it can be concluded that, for any rotator waveguide, there is an input polarization state (A_{in}^{opt}) that ensures output TM polarized light, i.e.

$$A_{in}=A_{in}^{opt}=\begin{bmatrix}\alpha_R e^{j\rho^{opt}}\\ \gamma_R\end{bmatrix} \Leftrightarrow P_{out}^{TM}=1 \qquad (A.9)$$

Let us consider now the tunable rotator scheme proposed in section 3.2.2 and schematically described in Fig. A.2. And let us analyze the TE to TM polarization rotation.

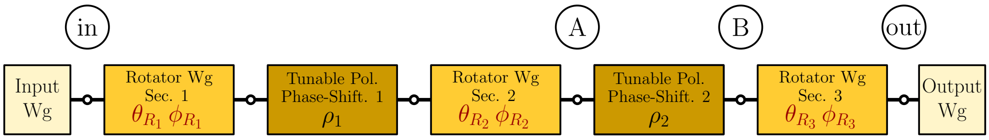

Figure A.2.: Proposed tunable rotator scheme, composed by three rotator waveguide sections, two tunable polarization phase-shifters, and input and output waveguides.

In this case light at the input is TE polarized ($P_{in}^{TE} = 1$ and $P_{in}^{TM} = 0$) and the aim is getting TM polarized light ($P_{out}^{TE} = 0$ and $P_{out}^{TM} = 1$) at the output. From the latter discussion it is clear that, in order to provide the desired rotation, polarization state at the input of the RWS$_3$ (point B in Fig. A.2) should be

$$A_B = A_{in_3}^{opt} = \begin{bmatrix} \alpha_{R_3} e^{j\rho^{opt}} \\ \gamma_{R_3} \end{bmatrix} \tag{A.10}$$

where α_{R_3} and γ_{R_3} are calculated particularizing eq. (A.6) for the RWS$_3$ characteristic parameters (θ_{R_3}, ϕ_{R_3}). Required differential phase shift (ρ^{opt}) can be provided by appropriately tuning the phase shift, ρ_2, introduced by the second polarization phase shifter (PPS$_2$). Thus, as polarization phase shifters do not change the TE-TM power ratio, a necessary condition for perfect rotation can be defined for the power of the polarization state (P_A) at the input of PPS$_2$ (point A in Fig. A.2) as

$$P_A = \begin{bmatrix} P_A^{TE} \\ P_A^{TM} \end{bmatrix} = \left| A_{in_3}^{opt} \right|^2 = \begin{bmatrix} \left|\alpha_{R_3}\right|^2 \\ \left|\gamma_{R_3}\right|^2 \end{bmatrix} \tag{A.11}$$

Following the same approach used to derive eq. (A.5), power in TM component in point A (P_A^{TM}) for input TE polarized light ($P_{in}^{TE} = 1$ and $P_{in}^{TM} = 0$) can be expressed as a sinusoidal function of ρ_1 (differential polarization phase shift introduced by PPS$_1$) with maximum and minimum values of

$$\begin{aligned} P_{A_{Max}}^{TM} &= \left[\alpha_{R_2}\gamma_{R_1} + \alpha_{R_1}\gamma_{R_2}\right]^2 \qquad \text{(A.12)} \\ P_{A_{min}}^{TM} &= \left[\alpha_{R_2}\gamma_{R_1} - \alpha_{R_1}\gamma_{R_2}\right]^2 \end{aligned}$$

where α_{R_i} and γ_{R_i} are calculated particularizing eq. (A.6) for the characteristic parameters (θ_{R_i}, ϕ_{R_i}) of the corresponding RWS$_i$. Always that the range $\left[P_{A_{Max}}^{TM}, P_{A_{min}}^{TM}\right]$ contains the value $\left|\gamma_{R_3}\right|^2$, there is a ρ_1 that ensures that condition in eq. (A.11) is met. Thus it can be concluded that, for the proposed polarization rotator scheme, perfect TE to TM polarization rotation can be achieved, tuning the differential phase shifts (ρ_1, ρ_2) induced by PPS$_1$ and PPS$_2$, always that RWS$_i$ meet the condition

$$\left[\alpha_{R_2} \cdot \gamma_{R_1} - \alpha_{R_1} \cdot \gamma_{R_2}\right]^2 < \left|\gamma_{R_3}\right|^2 < \left[\alpha_{R_2} \cdot \gamma_{R_1} + \alpha_{R_1} \cdot \gamma_{R_2}\right]^2 \tag{A.13}$$

This condition determines feasibility of the proposed polarization rotator scheme to provide perfect rotation polarization for different deviations from the optimal parameters in the waveguide rotators.

B

Curriculum Vitae

Carlos A. Alonso Ramos earned his MSc in Telecommunications engineering from Universidad de Málaga in 2008. In the period from June 2008 to June 2010 he worked in integrated optics at Universidad de Málaga, under the European CELTIC project 100GET [74]. Since 2010, funded by a national scholarship, he has been working towards his Ph.D. on the design of integrated photonic circuits under the supervision of **Prof. Alejandro Ortega-Moñux** and **Prof. Iñigo Molina Fernández**, and the tutorship of **Prof. Pavel Cheben**. Together with the Photonics & RF group at the Universidad de Málaga [1], he has been collaborating with the National Research Council Canada developing grating couplers for the micron-scale SOI platform, the Fraunhofer Heinrich-Hertz-Institut designing integrated polarization management devices for InP coherent receivers, the Université Paris Sud improving tolerances of integrated polarization rotators, and the Politecnico di Milano implementing advanced integrated photonic filters.

Stays foreign Centers

July–September 2014 Massachusetts Institute of Technology, Cambridge, United States. Oxygen sensitization of PbTe for enhanced mid-IR detection under supervision of Prof. Lionel C. Kimerling.

August–October 2013 National Research Council, Ottawa, Canada. Design of grating coupler for Si-wires under supervision of Prof. Pavel Cheben.

October–December 2012 Politecnico di Milano, Milano, Italy. Design of integrated filters based on ring resonators under supervision of Prof. Andrea Melloni.

October 2011–January 2012 Université Paris-Sud, Paris, France. Design of integrated polarization rotators for Si-wires under supervision of Prof. Laurent Vivien.

April–July 2010 National Research Council, Ottawa, Canada. Design of light collection system for Multi Aperture Transform Chip Heterodyne (MATCH) spectrometer under supervision of Prof. Pavel Cheben.

Awards

January 2013 Award for the best poster presentations in 5^{th} International Conference on Si Photonics and Satellite Schooling on Si Photonics at Univ. of Tokyo.

June 2012 Spanish Official National Telecommunications Engineer Association (COIT) finalist for best Postgraduate courses thesis.

April 2012 Award for the best oral presentation in SPIE Photonics Europe 2012, Brussels (see international conference [8] below).

March 2012 Universidad de of Málaga Juan López de Peñalver 5^{th} Edition Award for the best publication in technologies area in 2011.

May 2011 International Commission for Optics (ICO) Award for the best oral presentation in Information Photonics 2011, Ottawa (see international conference [11] below).

Patents

1. **C. Alonso-Ramos**, P. J. Reyes-Iglesias, A. Ortega-Moñux, I. Molina-Fernández, R. Halir, “Downconverter integrado con diversidad de polarización para receptor óptico coherente con multiplexación por polarización,” **ES2014/201300742**.
2. **C. Alonso-Ramos**, L. Vivien, P. Cheben, R. Halir, D. Marris-Morini, A. Ortega-Moñux, I. Molina-Fernández, J. Schmid, S. Janz, D.-X. Xu, “Highly tolerant and tuneable integrated optical polarization rotator,” **PCT/FR2012/051001**.

International Journal Papers

1. **C. Alonso-Ramos**, P.J. Reyes-Iglesias, A. Ortega-Moñux, D. Pérez-Galacho, R. Halir, I. Molina-Fernández, “PBS-less integrated dual-polarization coherent receiver,” *Opt. Lett.*, *under review*.
2. **C. Alonso-Ramos**, F. Morichetti, A. Ortega-Moñux, I. Molina-Fernández, M. J. Strain, A. Melloni, “Dual-mode coupled-resonator integrated optical filters,” *IEEE Photon. Technol. Lett.*, Vol. 26, pp. 929-932, 2014. (View online)
3. R. Halir, A. Ortega-Moñux, J.H. Schmid, **C. Alonso-Ramos**, J. Lapointe, D.-X. Xu, Wangüemert-Pérez, Molina-Fernández, S. Janz, “Recent Advances in Silicon Waveguide Devices Using Sub-Wavelength Gratings,” *IEEE J. Select. Topics Quantum Electron.*, Vol. 20, pp. 1-14, 2014. (View online)
4. D. Pérez-Galacho, R. Zhang, A. Ortega-Moñux, R. Halir, **C. Alonso-Ramos**, P. Runge, K. Janiak, G, Zhou, H.-G. Bach, A. G. Steffan, I. Molina-Fernández, “Integrated Polarization Beam Splitter for 100/400 GE Polarization Multiplexed Coherent Optical Communications,” *J. Lightwave Technol.*, Vol. 32, pp. 361-368, 2014. (View online)

5. A. Ortega-Moñux, **C. Alonso-Ramos**, A. Maese-Novo, R. Halir, L. Zavargo-Peche, D. Pérez-Galacho, I. Molina-Fernández, J. G. Wangüemert-Pérez, P. Cheben, J. Schmid, J. Lapointe, D.-X. Xu, S. Janz, "An ultra-compact multimode interference coupler with a subwavelength grating slot," *Laser & Photon. Rev.*, Vol. 7, pp. L12-L15, 2013. (View online)

6. D. Pérez-Galacho, R. Halir, A. Ortega-Moñux, **C. Alonso-Ramos**, R. Zhang, P. Runge, K. Janiak, H.-G. Bach, A.G. Steffan, I. Molina-Fernández, "Integrated polarization beam splitter with relaxed fabrication tolerances," *Opt. Express*, Vol. 21, pp. 14146-14151, 2013. (View online)

7. **C. Alonso-Ramos**, L. Zavargo-Peche, A. Ortega-Moñux, R. Halir, I. Molina-Fernández, P. Cheben, "Polarization-independent grating coupler for micrometric silicon rib waveguides," *Opt. Lett.*, Vol. 37, pp. 3663-3665, 2012. (View online)

8. **C. Alonso-Ramos**, R. Halir, A. Ortega-Moñux, P. Cheben, L. Vivien, I. Molina-Fernández, D. Marris-Morini, S. Janz, D.-X. Xu, J. Schmid, "Highly tolerant tunable waveguide polarization rotator scheme," *Opt. Lett.*, Vol. 37, pp. 3534-3536, 2012. (View online)

9. A. V. Velasco, M. L. Calvo, P. Cheben, A. Ortega-Moñux, J. Schmid, **C. Alonso-Ramos**, I. Molina-Fernández, J. Lapointe, M,.Vachon, S. Janz, D.-X. Xu, "Ultracompact polarization converter with a dual subwavelength trench built in a silicon-on-insulator waveguide," *Opt. Lett.*, Vol. 37, pp. 356-367, 2012. (View online)

10. **C. Alonso-Ramos**, S. Romero-García, A. Ortega-Moñux, I. Molina-Fernández, R. Zhang, H. G. Bach, M. Schell, "Polarization rotator for InP rib waveguide," *Opt. Lett.*, Vol. 37, pp. 335-337, 2012. (View online)

11. **C. Alonso-Ramos**, A. Ortega-Moñux, I. Molina-Fernández, P. Cheben, L. Zavargo-Peche, R. Halir, S. Janz, D.-X. Xu, N. Kim, B. Lamontagne, "Grating couplers for thick SOI rib waveguides," *Opt. Quantum Electron.* Vol. 44, pp. 535-540, 2012. (View online)

12. M. Florjańczyk, **C. Alonso-Ramos**, P. Bock, A. Bogdanov, P. Cheben, I. Molina-Fernández, S. Janz, B. Lamontagne, A. Ortega-Moñux, A. Scott, K. Sinclair, B. Solheim, D.-X. Xu, "Development of a Fourier-transform waveguide spectrometer for space applications," *Opt. Quantum Electron.* Vol. 44, pp. 549-556, 2012. (View online)

13. **C. Alonso-Ramos**, A. Ortega-Moñux, L. Zavargo-Peche, R. Halir, J. de Oliva-Rubio, I. Molina-Fernández, P. Cheben, D.-X. Xu, S. Janz, N. Kim, B. Lamontagne, "Single-etch grating coupler for micrometric silicon rib waveguides," *Opt. Lett.*, Vol. 36, pp. 2647-2649, 2011. (View online)

14. **C. Alonso-Ramos**, A. Ortega-Moñux, I. Molina-Fernández, P. Cheben, L. Zavargo-Peche, R. Halir, "Efficient fiber-to-chip grating coupler for micrometric SOI rib waveguides," *Opt. Express*, Vol. 18, pp. 15189-15200, 2010. (View online)

International Conferences

1. A. Ortega-Moñux, R. Halir, A. Maese-novo, **C. Alonso-Ramos**, L. Zavargo-Peche, D. Pérez-Galacho, I. Molina-Fernández, J. G. Wangüemert-Pérez, P. Cheben, J. Schmid, J. Lapointe, D.-X. Xu, S. Janz, “Re-inventing Multimode Interference Couplers Using Subwavelength Gratings,” *Conference on Laser and Optoelectronics Europe*, May 12-16 2013, Munich, Germany.

2. A. Ortega-Moñux, D. Pérez-Galacho, R. Halir, **C. Alonso-Ramos**, P. J. Reyes-Iglesias, S. Romero-García, R. Godoy-Rubio, J. G. Wangüemert-Pérez, Molina-Fernández, “Design of Photonic Integrated Circuits for Coherent Optical Networks (100GbE and Beyond),” *Information Photonics*, Sep. 16-19 2013, Warsaw, Poland.

3. **C. Alonso-Ramos**, F. Morichetti, S. Grillanda, A. Ortega-Moñux, I. Molina Fernández, A. Melloni, “Photonic integrated dual-mode filters realized with ring resonators loaded by Bragg gratings,” *Integrated Photonics Research, Silicon and Nano-Photonics (IPR)*, July 14-17 2013, Rio Grande, PuertoRico.

4. **C. Alonso-Ramos**, R. Halir, A. Ortega-Moñux, P. Cheben, L. Vivien, I. Molina-Fernández, D. Marris-Morini, S. Janz, D.-X. Xu, J. Schmid, “A general approach for robust integrated polarization rotators,” *SPIE Optics Optoelectronics*, April 15-18 2013, Prague, Czech Republic.

5. A. Ortega-Moñux, R. Halir, A. Maese-Novo, **C. Alonso-Ramos**, L. Zavargo-Peche, D. Pérez-Galacho, I. Molina-Fernández, J. G. Wangüemert-Pérez, P. Cheben, J. Schmid, J. Lapointe, D.-X. Xu, S. Janz, “Re-inventing Multimode Interference Couplers Using Subwavelength Gratings,” *Conference on Laser and Electro-Optics Europe and International Quantum Electronics Conference (CLEO)*, May 12-16 2013, Munich, Germany.

6. P. Cheben, J. Schmid, **C. Alonso-Ramos**, R. Halir, L. Zavargo-Peche, J. Lapointe, P. Bock, D.-X. Xu, S. Janz, A. Ortega-Moñux, I. Molina-Fernández, R. Ma, M. Vachon, A. Delage, J. M. Fedeli, “Diffractive and subwavelength grating couplers for microphotonic waveguides,” *14th International Conference on Transparent Optical Networks (ICTON)*, July 2-5 2012, Coventry, England.

7. A. V. Velasco, M. L. Calvo, P. Cheben, A. Ortega-Moñux, J. H Schmid, **C. Alonso-Ramos**, I. Molina-Fernández, J. Lapointe, M. Vachon, S. Janz, D.-X. Xu, “Ultra-Compact Polarization Mode Converter Implemented in a Dual-Trench Silicon-On-Insulator Waveguide,” *Conference on Laser and Electro-Optics: Lasers ans innovations (CLEO)*, May 6-11 2012, San Jose California, United States.

8. **C. Alonso-Ramos**, A. Ortega-Moñux, R. Halir, L. Zavargo-Peche, I. Molina-Fernández, P. Cheben, D.-X. Xu, S. Janz, “Grating couplers in thick rib SOI waveguides for TE and TM polarizations,” *SPIE Photonics Europe*, April 16-19 2012, Brussels, Belgium.

9. **C. Alonso-Ramos**, A. Ortega-Moñux, L. Zavargo-Peche, R. Halir, J. de-Oliva-Rubio, I. Molina-Fernández, P. Cheben, D.-X. Xu, S. Janz, N. Kim, “Efficient fibre-chip grating coupler for thick SOI rib waveguides,” *European Conference and Exposition on Optical Communications (ECOC)*, September 18-22 2011, Geneva, Switzerland.

10. P. Cheben, M. Florjańczyk, P. Bock, **C. Alonso-Ramos**, B. Lamontagne, A. Bogdanov, S. Janz, D.-X. Xu, M. Vachon, A. Scott, A. Ortega-Moñux, I. Molina-Fernández, B. Solheim, K. Sinclair, “Recent advances in Fourier-transform waveguide spectrometers,” *13th International Conference on Transparent Optical Networks (ICTON)*, June 26-30 2011, Stockholm, Sweden.

11. **C. Alonso-Ramos**, A. Ortega-Moñux, I. Molina-Fernández, P. Cheben, L. Zavargo-Peche, R. Halir, N. Kim, S. Janz, D.-X. Xu, “Design of an optimized grating coupler for thick SOI rib waveguides,” *ICO International Conference on Information Photonics (IP)*, May 18-20 2011, Ottawa, Canada.

12. A. Scott, P. Bock, **C. Alonso-Ramos**, B. Lamontagne, P. Cheben, M. Florjańczyk, I. Molina-Fernández, S. Janz, A. Ortega-Moñux, B. Solheim, D.-X. Xu “Improved coupling to integrated spatial heterodyne spectrometers with applications to space,” *SPIE Reliability, Packaging, Testing, and Characterization of MEMS/ MOEMS and Nanodevices*, January 22-25 2011, San Francisco California, United States.

C

Resumen en Español

C.1. Introducción

En 1969 Stewart E. Miller propuso por primera vez la implementación de un chip fotónico integrado. En su artículo, publicado en la Bell System Technical Journal [2], Miller proponía el uso de guías de onda dieléctricas de tipo *strip*, moduladores de fase en guía, anillos resonadores, o reflectores de Bragg como filtros ópticos o cavidad resonante para láseres, sentando las bases de la fotónica actual. El láser había sido inventado nueve años antes [3], y sólo dos años después varios grupos ya habían demostrado su implementación utilizando semiconductores [4–7]. Por aquel entonces se auguraba un futuro brillante para la fotónica integrada, con un crecimiento exponencial similar a aquel vivido por la microelectrónica. Pero, en palabras de Miller *"economy should ultimately result"* [2], y no lo hizo, al menos no de la manera esperada. Las posibles razones de este desarrollo tan lento de la fotónica (comparado con la microelectrónica) han sido revisadas recientemente por Ivan P. Kaminow, compañero de Miller en Bell Labs en aquella época, e incluye entre otras el hecho de que pocas aplicaciones han sido identificadas que requieran al mismo tiempo de un alto nivel de integración y un gran volumen de producción [8].

Hoy en día, aplicaciones como el vídeo-bajo-demanda (*youtube*), las redes sociales (*facebook*), o los motores de búsqueda (*google*), utilizan una gran red de *data centers*, interconectados mediante enlaces ópticos para compartir enormes cantidades de información [9]. El continuo crecimiento de la cantidad y velocidad de los datos intercambiados y el consumo de potencia dentro de estos *data centers* está llevando a los enlaces eléctricos cerca de su límite fundamental. Se espera que los enlaces ópticos puedan solventar estas limitaciones, reemplazando a los enlaces tradicionales en todo el rango de comunicaciones que abarca desde 1 metro a 10 km [10]. Un ejemplo de esto son los cables opto-electrónicos que la compañía Luxtera comercializa de forma exitosa desde 2006 [11]. Otro ejemplo que ilustra esta nueva tendencia es el hecho de que en 2013 el *Optical Internetworking Forum* (OIF) sacara una recomendación para los sistemas de interconexión de nueva generación [12]. Además, la distancia entre la capacidad computacional, y el ancho de banda de los enlaces eléctricos en los sistemas de computación de alto rendimiento (*super computers*) aumenta cada día. Esto hace que se estén desarrollando enlaces ópticos entre distintos *racks* del sistema, e incluso entre distintos chips dentro de un mismo *rack* [13]. La fotónica del silicio, debido a su compatibilidad con la plataforma CMOS, ha sido la solución elegida por compañías como IBM [17], Intel [18] y Oracle [19] para el desarrollo de la nueva generación de enlaces fotónicos. Además, aplicaciones como el *mid-infrared* [20], el biosensado [21] o el *microwave photonics* [22], necesitan de dispositivos fotónicos de altas prestaciones y bajo coste. Este enorme mercado potencial, con millones de dispositivos por año, abre una segunda ventana para el crecimiento exponencial de la fotónica, pero de nuevo *"economy should ultimately result"*.

En esta deseada y esperada plataforma fotónica de producción masiva, los dispositivos son fabricados por miles en cada paso de procesado (*wafer-scale processing*). Por tanto, si se quiere obtener una rentabilidad adecuada, los dispositivos tienen que ser probados por miles en cada paso de chequeo (*wafer-scale testing*). Por otra parte, los enlaces ópticos de próxima generación han de ser capaces de proporcionar conectividad para cables compuestos de decenas e incluso cientos de fibras ópticas [12]. Además, las pérdidas de inserción del interfaz chip-fibra determinan el alcance, la sensibilidad y las prestaciones del enlace óptico [24]. Las redes de difracción (*grating couplers*) ofrecen *wafer-scale testing*, pérdidas de inserción bajas y buenas tolerancias de alineamiento. Esto hace que sean consideradas como un elemento básico de la librería de elementos fotónicos de próxima generación [11, 24, 25]. Por otro lado, la implementación de curvas de Euler sobre guías de silicio micrométricas, que permite radios de curvatura de $10\,\mu\mathrm{m}$ [43], abre un nuevo camino hacia niveles de integración nunca antes vistos en esta plataforma. De esta manera, se pueden desarrollar dispositivos con un área similar a la de aquellos basados en *nano-wires*, que se benefician de la menor dependencia de la polarización, y mejores pérdidas de propagación de las guías micrométricas [44]. La sección C.2 de esta tesis está dedicada al diseño e implementación de redes de difracción para la plataforma nanométrica. En C.2.1, se propone una novedosa geometría que permite la implementación de redes de difracción eficientes para la plataforma *silicon-on-insulator* (SOI) micrométrica. Dicha geometría es verificada experimentalmente. Este enfoque de diseño se extiende en C.2.2 para proporcionar un acoplo eficiente independiente de la polarización. La implementación de un interfaz de entrada basado en redes de difracción SOI micrométricas para un espectrómetro integrado para aplicaciones espaciales, se discute en C.2.3.

Los enlaces ópticos son una tecnología madura y bien establecida en el mercado de las comunicaciones de largo alcance. En este campo, compañías como Infinera [45] o $\mathrm{U}^2\mathrm{t}$ [46] comercializan circuitos fotónicos integrados a gran escala basados en fosfuro de indio (InP), que ofrecen tasas de datos que superan los 100Gb/s utilizando multiplexación por longitud de onda. Se espera que los sistemas de próxima generación, basados en multiplexación por polarización, incrementen dicha capacidad alcanzando tasas de 100-400Gb/s por canal [47]. A medida que el número de elementos por circuito aumenta, la integración monolítica de los mismos se hace más y más interesante. Dicha integración proporciona una amplia gama de ventajas, entre las que destacan la reducción del peso, tamaño y consumo de potencia, o la mejora de la fiabilidad y prestaciones [59]. A pesar de las numerosas ventajas de la integración monolítica, los transceptores comerciales para sistemas basados en multiplexación por polarización, implementan el manejo de la polarización (esto es rotadores y separadores de polarización) fuera del chip. Las principales razones para esto son el incremento de la complejidad de la fabricación (requiriendo de pasos de procesamiento adicional) y las tolerancias de fabricación limitadas de los rotadores y separadores de polarización integrados. En la sección C.3, se presentan varias soluciones para facilitar el manejo de la polarización en los transceptores coherentes de doble polarización monolíticamente integrados de futura generación. En C.3.1, se analiza el diseño de un rotador de polarización integrado perfectamente compatible con los receptores de una sola polarización previamente desarrollados. In C.3.2, se propone un novedoso esquema que permite mejorar substancialmente las tolerancias de fabricación de los rotadores de polarización integrados. Por último, en C.4 se discute la viabilidad de una nueva arquitectura que permite la implementación de receptores coherentes para sistemas basados en multiplexación por polarización, sin necesidad de utilizar rotadores ni separadores de polarización.

C.2. Redes de difracción

La interconexión eficiente entre el chip fotónico integrado y otros dispositivos externos, especialmente la fibra óptica monomodo, supone una funcionalidad clave que ha de incluir cualquier plataforma que pretenda liderar la implementación de los dispositivos de altas prestaciones de la próxima generación. Este tema es un reto, especialmente para las guías SOI, ya que sufren de una gran disparidad en términos de tamaño e índice de refracción con la fibra óptica. El acoplo directo entre una fibra óptica y una guía SOI (micro o nanométrica), produce unas pérdidas de inserción mayores a $12\,\mathrm{dB}$ [87]. Se ha propuesto una gran variedad de alternativas para mejorar esta eficiencia de acoplo, basadas en el acoplo a través del borde del chip. Una opción es enfocar la luz que viene de la fibra utilizando una lente and la fibra o el chip [88]. Otra opción es expandir el el área modo fundamental de la guía, para ajustarla al tamaño del modo de la fibra. Esto puede hacerse:

- Incrementando el tamaño del núcleo de la guía con i) un *taper* 3D (ver C.1-a) donde el ancho y el alto de la guía son incrementados adiabáticamente [89, 90], o ii) un *taper* multi-etapa (ver Fig. C.1-b), donde guías de distinto grosor son interconectadas mediante *tapers* adiabáticos en los que solo se varía el ancho [87]. Esta estrategia requiere de un proceso de fabricación complejo y de una cubierta anti-reflectante.

- Reduciendo el tamaño del núcleo de la guía (al reducir el factor de confinamiento se expande el tamaño efectivo del modo de la guía), con i) un *taper* inverso (ver Fig. C.1-c), en el que se reduce el ancho de la guía adiabáticamente [91–93], o ii) *taper sub-wavelength* (ver Fig. C.1-d) donde se reduce el índice de refracción sintetizado de manera adiabática [94].

- Implementando un conversor de tamaño de modo usando una estructura multicapa en el substrato.

Las soluciones que utilizan el borde del chip proporcionan eficiencias de acoplo mejores que $-1\,\mathrm{dB}$ simultáneamente para ambas polarizaciones en un amplio ancho de banda [93, 94]. De cualquier modo, el hecho de que todas las entradas y salidas tengan que ser enrutadas hacia el borde del chip puede suponer una limitación fundamental en

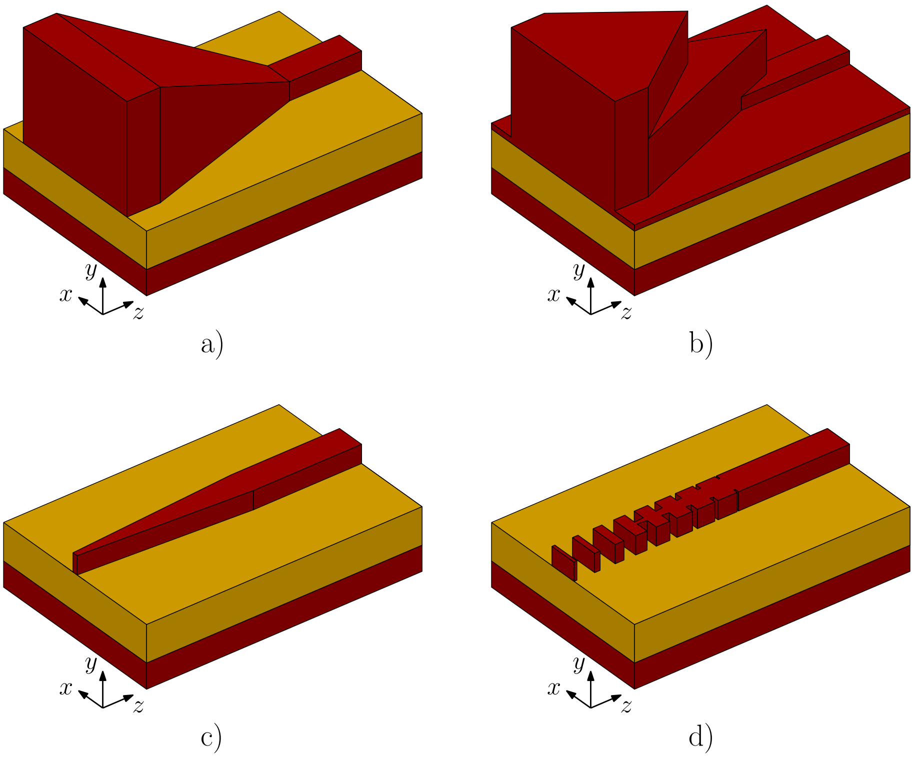

Figure C.1.: Representación esquemática de soluciones de acoplo por el borde del chip basadas en: **a)** *taper* 3-D **b)** *taper* multi-etapa **c)** *taper* inverso **d)** *taper sub-wavelength*.

circuitos de próxima generación en los que la complejidad (y número de elementos) no para de incrementar.

Una estrategia alternativa es acoplar la luz a través de la superficie del chip, utilizando redes de difracción. Las redes de difracción pueden ser situadas en cualquier parte del chip, maximizando la escalabilidad, con muy buenas tolerancias de alineamiento. Además, permiten *wafer-scale testing*, evitando la necesidad de cortar y pulir cada circuito antes de testear su correcto funcionamiento. Esto, permite reducir los costes de producción [11]. En principio, las redes de difracción tienen una eficiencia menor que la de las soluciones basadas en acoplo a través del borde del chip, debido a las pérdidas en el substrato y a las diferencias entre los perfiles del campo radiado por la red y el modo fundamental de la fibra. La naturaleza resonante de estas redes, hace que sean muy sensibles a la longitud de onda y la polarización. Se ha dedicado un enorme esfuerzo a aliviar estos inconvenientes. Se han demostrado redes de difracción de acoplo con eficiencias ($\sim -1\,\mathrm{dB}$) comparables a las soluciones basadas en acoplo por borde [28,40]. También se han propuesto soluciones que mejoran el ancho de banda ($BW_{1\,\mathrm{dB}} \sim 280\,\mathrm{nm}$) [42] y la dependencia con la polarización [35].

Las redes de difracción de acoplo chip-fibra se han convertido en un elemento esencial de las librerías de componentes de Luxtera [25] y EpixFab [97]. Las redes de difracción de acoplo se utilizan como interfaz de entrada salida en comunicaciones [98] y aplicaciones de biosensado [99]. Además, las redes de difracción son vistas como una solución prometedora para la implementación de enlaces fotónicos para aplicaciones de conexión

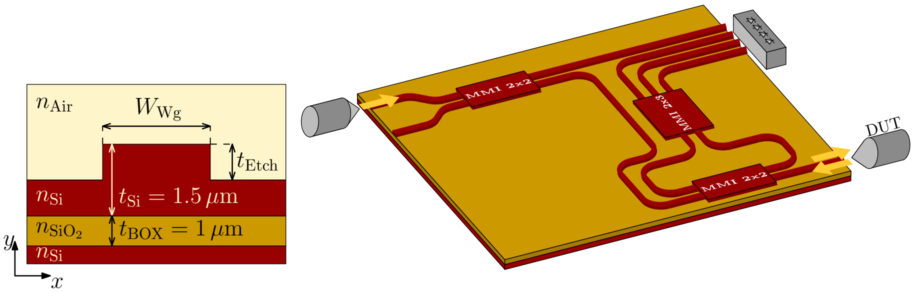

a) b)

Figure C.2.: a) Geometría transversal de guía SOI *Rib*. **b)** Representación esquemática de reflectómetro de seis puertos con acoplo de entrada salida por borde del chip.

chip a chip [100], o la integración híbrida de foto detectores [101] o láseres [102] en III-V.

En esta sección, se discute la implementación de redes de difracción en guías SOI *rib* micrométricas, como la que se presenta en la Fig. C.2-a. El alto nivel de madurez de esta tecnología, junto con las bajas pérdidas de propagación o birrefringencia, y la compatibilidad con litografía estándar *i-line stepper* hace que la plataforma micrométrica SOI sea muy atractiva para la implementación de circuitos de altas prestaciones, que incluyen dispositivos de interferencia multimodal [120], demultiplexores [121], espectrómetros basados en transformada de Fourier [122], o demoduladores *differential phase-shift keying* [123]. Además, se ha demostrado experimentalmente que se pueden obtener pérdidas por debajo de $0.02\,\text{dB}$, con radios de curvatura de sólo $10\,\mu\text{m}$ en guías de $4\,\mu\text{m}$ de espesor. Esto abre la puerta a densidades de integración para la plataforma micrométrica, comparables con aquellas de la plataforma nanométrica, con el beneficio añadido de las ventajas mencionadas anteriormente.

Aunque las redes de difracción se han venido usando de manera exitosa en la plataforma SOI nanométrica, su implementación en la plataforma micrométrica no es directa. Dos, son los retos principales de las redes de difracción en guías SOI micrométricas:

- Mientras que las redes de difracción nanométricas son monomodo verticalmente, las redes de difracción micrométricas son multi-modo. Esto se debe al mayor tamaño de las mismas.

- Debido a que las tamaños mínimos fabricables en la plataforma micrométrica son mucho mayores que en la nanométrica ($\sim 100\,\text{nm}$ para redes de difracción nanométricas y $\sim 350\,\text{nm}$ para redes de difracción micrométricas), los periodos y ciclos de trabajo elegibles están muy limitados.

En esta sección se proponen algunas soluciones innovadoras, que permiten solventar las limitaciones intrínsecas de las redes de difracción micrométricas. Dichas soluciones que permiten la implementación del dispositivo utilizando un único paso de grabado, son presentadas junto con un proceso sistemático de diseño. Esta estrategia de diseño, ha abierto un prometedor camino que ha sido seguido por compañías tales como Intel [67] u Oracle [68].

Esta sección se organiza de la siguiente manera. En C.2.1 se describe en destalle el diseño y caracterización experimental de una red de difracción SOI micrométrica para acoplo de chip a fibra. En C.2.2, el diseño de la red se extiende para proporcionar un comportamiento independiente de la polarización. Finalmente, en C.2.3, se presenta el diseño de un interfaz de entrada para un espectrómetro integrado.

C.2.1. Redes de difracción para interconexión chip-fibra

En esta sección se presenta el diseño de una red de difracción para guías micrométricas SOI, que asegura la generación de un único haz de radiación, cumpliendo con las restricciones de diseño. También se discute cómo maximizar la eficiencia de acoplo y cómo minimizar las reflexiones. La motivación inicial para la realización de este diseño fue implementar un interfaz de entrada salida para reflectómetros de seis puertos [124] desarrollados con anterioridad por el grupo de fotónica en la Universidad de Málaga [1]. Dichos espectrómetros, basados en guías SOI micrométricas como la que se presenta en la Fig. C.2-a, están compuestos por varios dispositivos de interferencia multimodal y guías de interconexión, como se muestra esquemáticamente en le Fig. C.2-b. Estos dispositivos tienen un puerto de entrada y un puerto bidireccional conectados a fibras ópticas monomodo estándar (SMF-28), y cuatro puertos de salida que pueden ser conectados a fibras ópticas o fotodetectores. Debido a la naturaleza de estos dispositivos, se desea tener bajas reflexiones en los puertos de entrada y salida. El uso de redes de difracción como interfaces de entrada salida, tiene como objetivo obtener una alta eficiencia de acoplo con bajas reflexiones sin tener que añadir ningún paso extra al proceso de fabricación, evitando además la necesidad de cortar, pulir y recubrir con una capa antireflectante el dispositivo.

Debido a las limitaciones anteriormente mencionadas, dos retos han de ser afrontados, que complican la implementación de redes de difracción micrométricas con un único haz de radiación

- La región de la red de difracción es multimodo para el grosor de guía de interés, $t_{Si} = 1.5\,\mu\mathrm{m}$.
- El periodo mínimo para que la red sea compatible con la fabricación estándar *i-line stepper* es de $\Lambda_{min} = 700\,\mathrm{nm}$ (tamaño mínimo de $350\,\mathrm{nm}$ para el hueco y para el diente de silico).

El ancho ($W_{\mathrm{Wg}} = 1.3\,\mu\mathrm{m}$) y la profundidad de grabado ($t_{\mathrm{Etch}} \leq 750\,\mathrm{nm}$) de las guías de interconexión han sido elegidos para cumplir la condición monomodo de Soref [125]. En la región de la red de difracción, la guía es substancialmente más ancha ($W_{\mathrm{Wg}} \sim 15\,\mu\mathrm{m}$), y por tanto no se cumple la condición de Soref. Esto hace que la guía sea multimodo verticalmente, además de lateralmente. De forma similar, la red de difracción soporta varios modos Bloch-Floquet. Incluso si se implementa un *taper* adiabático entre la guía de interconexión y la red de difracción que asegure que sólo se excita el modo fundamental de la guía de acceso, los modos Bloch-Floquet superiores se excitarán en la discontinuidad producida entre la guía y la red. De este modo, el campo en la red de difracción es una superposición de los modos Bloch-Floquet soportados por la estructura.

$$E(y,z) = \sum_i c_i \vartheta_i(y,z), \tag{C.1}$$

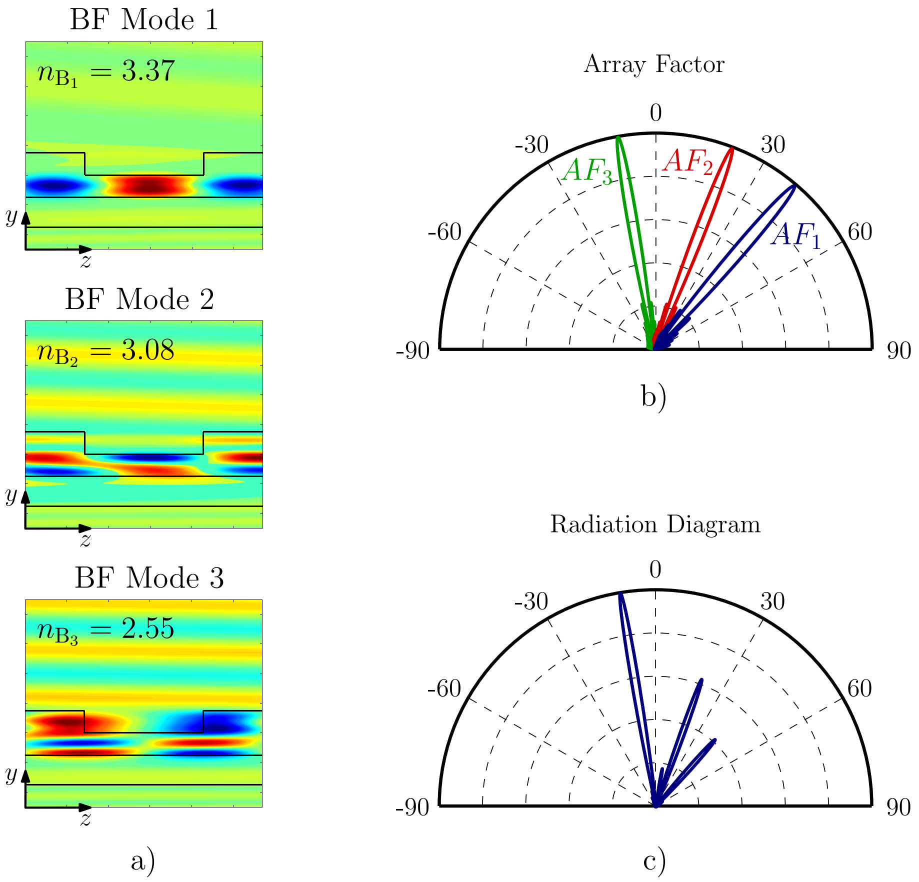

Figure C.3.: Para una red de difracción con $t_{\mathrm{Etch}} = 750\,\mathrm{nm}$, $DC = 0.5$, y periodo $\Lambda = 570\,\mathrm{nm}$: **a)** distribución de campo de los tres primeros modos Bloch-Floquet, **b)** factor de *array* normalizado, **c)** patrón de radiación cuando el modo fundamental de una guía de acceso con $t_{\mathrm{AcWg}} = 1.5\,\mu\mathrm{m}$ es inyectado en la red de difracción propuesta.

donde c_i es la amplitud compleja del i-ésimo modo Bloch-Floquet, que depende del campo inyectado en la red. El campo radiado por la red es la suma ponderada de la contribución de cada uno de estos modos. Por tanto, el factor de *array*, en este caso, se puede expresar como

$$\begin{aligned} AF\left(\theta\right) &= |c_1| \cdot AF_1\left(\theta\right) + |c_2| \cdot AF_2\left(\theta\right) + |c_3| \cdot AF_3\left(\theta\right) \\ AF_1\left(\theta\right) &= \sum_{n=0}^{NP-1} e^{j\frac{2\pi}{\lambda}\Lambda n\left[n_c \sin(\theta) - n_{\mathrm{B}_1}\right]} \\ AF_2\left(\theta\right) &= \sum_{n=0}^{NP-1} e^{j\frac{2\pi}{\lambda}\Lambda n\left[n_c \sin(\theta) - n_{\mathrm{B}_2}\right]} \\ AF_3\left(\theta\right) &= \sum_{n=0}^{NP-1} e^{j\frac{2\pi}{\lambda}\Lambda n\left[n_c \sin(\theta) - n_{\mathrm{B}_3}\right]}, \end{aligned} \tag{C.2}$$

donde $AF_i\left(\theta\right)$ es el factor de *array* del i-ésimo modo Bloch-Floquet (con índice efectivo

n_{B_i}), NP es el número de periodos y n_{c} el índice de refracción de la cubierta. Está claro que, incluso si se cumple la condición de único haz de radiación, puede haber varios haces de radiación, correspondientes con el armónico $k = -1$ de cada modo Bloch-Floquet.

Para ilustrar este problema, se analizan a continuación las características de una red con $t_{\mathrm{Etch}} = 750\,\mathrm{nm}$, $DC = 0.5$, y un periodo de $\Lambda = 570\,\mathrm{nm}$. La distribución de campo, $\vartheta_i(y, z)$, de los tres primeros modos Bloch-Floquet de la red, con índices efectivos de $n_{\mathrm{B}_1} = 3.37$, $n_{\mathrm{B}_2} = 3.08$, y $n_{\mathrm{B}_3} = 2.55$, se presenta en la Fig. C.3-a. El factor de *array* de la red, extraído de la eq. (C.2) asumiendo $|c_i|^2 = 1$, se presenta en la Fig. C.3-b. Puede verse que aparecen tres haces de radiación (con ángulos de $\sim 41°, 20°, -10°$) que se corresponden con el armónico $k = -1$ del primer, segundo y tercer modo Bloch-Floquet. El diagrama de radiación, cuando se inyecta en la red el modo fundamental de una guía de acceso con $t_{\mathrm{AcWg}} = 1.5\,\mu\mathrm{m}$, se presenta en la Fig. C.3-c. La excitación producida por esta guía de acceso, produce tres haces de radiación cuyos ángulos están determinados por el factor de *array*, y cuyas amplitudes relativas están relacionadas con la potencia acoplada a cada modo Bloch-Floquet. Puesto que la potencia radiada por los haces indeseados se pierde (se propaga con un ángulo diferente y no puede ser recogida adecuadamente por la fibra), cualquier estructura que excite modos de orden superior puede resultar en una baja eficiencia de acoplo.

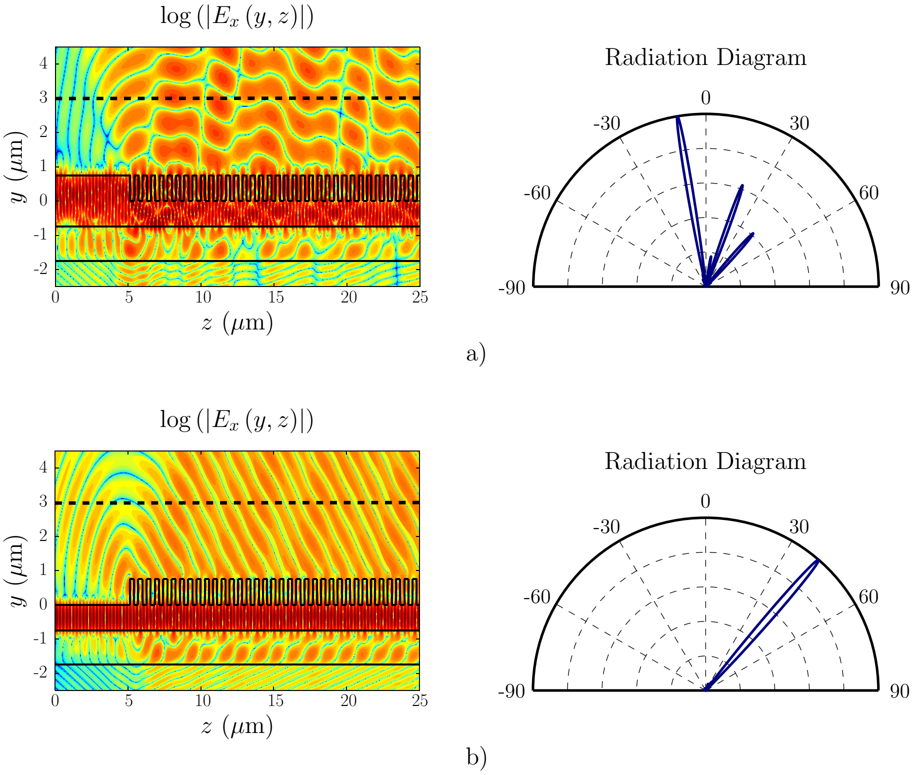

a)

b)

Figure C.4.: Geometría del dispositivo, campo radiado, y diagrama de radiación calculado para red de difracción con $t_{\mathrm{Etch}} = 750\,\mathrm{nm}$, $DC = 0.5$, $\Lambda = 570\,\mathrm{nm}$ y 40 periodos con **a)** guía de acceso gruesa ($t_{\mathrm{AcWg}} = 1.5\,\mu\mathrm{m}$), y **b)** guía de acceso fina ($t_{\mathrm{AcWg}} = 750\,\mathrm{nm}$).

La excitación de los modos Bloch-Floquet (y por tanto las características de radiación de la red) depende del campo inyectado en la red. En el modelo 2D utilizado para el diseño de la red, el campo de excitación queda definido por el grosor de la guía de acceso. La Fig. C.4 muestra la geometría del dispositivo, el campo radiado y el diagrama de radiación para la misma red de difracción utilizada en la Fig. C.3. Se han utilizado dos guías de acceso, una más gruesa, y otra más fina. La red de difracción con guía de acceso más gruesa (Fig. C.4-a) presenta, como ya antes se había mencionado, tres haces de radiación que interfieren produciendo una distribución de campo borrosa sobre la región de la red. En la región de *slab* más fina, se puede observar un patrón de interferencia, típico de la excitación de modos superiores, confirmando el comportamiento multimodo de la estructura. La red de difracción con una guía de acceso más fina (Fig. C.4-b) tiene un único haz de radiación, que se corresponde con el orden $k = -1$ del modo Bloch-Floquet fundamental. Se puede observar cómo la estructura genera un frente de ondas plano dentro y sobre red de difracción.

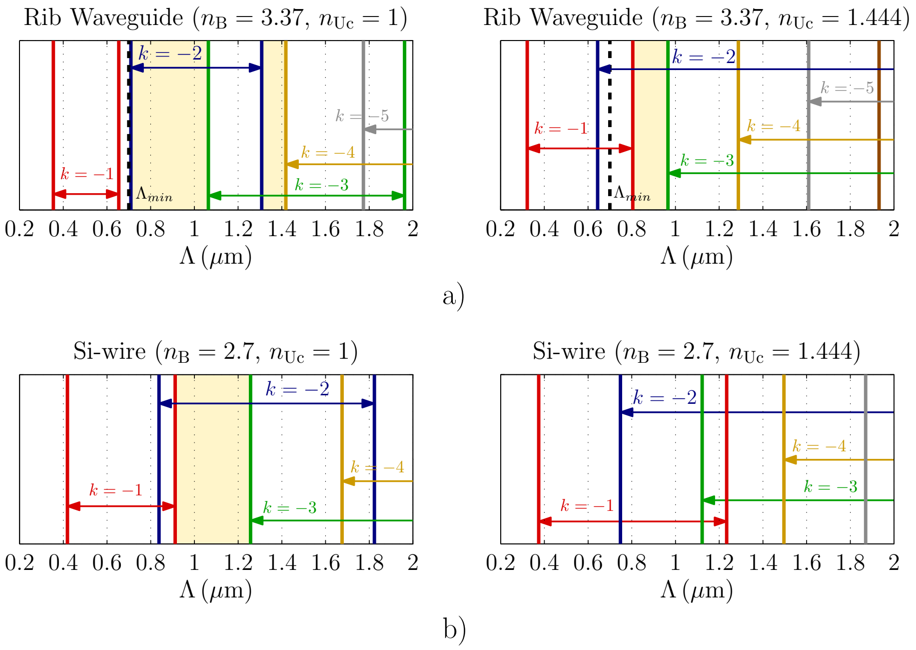

Figure C.5.: Condición de radiación evaluada para distintos armónicos considerando cubierta de aire y dióxido de silicio para: **a)** Modo Bloch-Floquet con índice efectivo de $n_{\mathrm{B}} = 3.37$, que se corresponde con el modo fundamental de una red de difracción micrométrica **b)** Modo Bloch-Floquet con índice efectivo de $n_{\mathrm{B}} = 2.7$, que corresponde con modo fundamental de una red de difracción nanométrica con $t_{\mathrm{AcWg}} = t\mathrm{Si} = 220\,\mathrm{nm}$, $t_{\mathrm{Etch}} = 70\,\mathrm{nm}$ y $n_{\mathrm{Uc}} = 1.444$. Las regiones que dan lugar a un único haz de radiación para armónicos de orden superior se muestran en beige.

Debido a las limitaciones de tamaño, incluso si se consigue excitación monomodo de la red de difracción, no se puede asegurar un único haz de radiación con la estrategia convencional que se basa en radiar utilizando solo el primer armónico $k = -1$. Asumiendo que el modo Bloch-Floquet fundamental tiene un índice efectivo que se encuentra comprendido entre aquellos de las guías de acceso más gruesa ($t_{\mathrm{Etch}} = 0$, $t_{\mathrm{AcWg}} = 1.5\,\mu\mathrm{m}$,

$n_{\text{eff}} = 3.44$) y más fina ($t_{\text{Etch}} = 750\,\text{nm}$, $t_{\text{AcWg}} = 750\,\text{nm}$, $n_{\text{eff}} = 3.37$) posibles, y teniendo en cuenta que $n_{\text{B}_1} > n_{\text{B}_2} > n_{\text{B}_3}$, puede deducirse que el periodo más largo que asegura que solo el armónico $k = -1$ puede radiar, es de $\Lambda = 650\,\text{nm}$. Este periodo es más corto que el más corto fabricable $\Lambda_{min} = 700\,\text{nm}$ con *i-line stepper*. Por tanto no se pueden elegir redes trabajen sólo con el armónico $k = -1$. Para solventar esta limitación, se utilizan periodos más largos, que permiten la radiación de armónicos de orden superior ($k = -2, -3, ...$). El periodo de la estructura se selecciona de manera que se obtiene un único haz de radiación para un armónico de orden superior.

Para tener un único haz de radiación para el armónico de orden $k = -2$, ha de encontrarse una ventana dentro de la región de radiación de dicho orden, donde los armónicos de órdenes contiguos ($k = -1$, -3) no puedan radiar. Esta región de haz de radiación único, solo puede darse si el periodo máximo que permite la radiación del armónico $k = -1$ as más corto que el mínimo que permite la radiación del orden $k = -3$, esto es

$$\begin{aligned} \Lambda_{\text{Max}_{-1}} &< \Lambda_{\text{Min}_{-3}} \\ \frac{\lambda}{n_{\text{c}} - n_{\text{B}}} &< \frac{3\lambda}{n_{\text{c}} + n_{\text{B}}}. \end{aligned} \tag{C.3}$$

Esto se traduce en la siguiente condición

$$n_{\text{B}} > 2 \cdot n_{\text{c}} \tag{C.4}$$

para el índice efectivo del modo bloch-Floquet, n_{B}, y el índice de refracción de la cubierta. Dicha condición se cumple de sobra para las redes de difracción micrométricas estudiadas aquí, que presentan $n_{\text{B}} = 3.44 - 3.37$ y $n_{\text{Uc}} = 1$. Las redes de difracción implementadas en guías nanométricas, tienen típicamente un índice efectivo Bloch-Floquet menor ($n_{\text{B}} \sim 2.7$), que complica la aparición de ventanas de un único haz de radiación para armónicos de orden superior. En la Fig. C.5, la condición de radiación se evalúa para distintos armónicos, considerando cubiertas de aire y dióxido de silicio para: i) modo Bloch-Floquet con índice efectivo de $n_{\text{B}} = 3.37$, que se corresponde con el modo fundamental de una red de difracción micrométrica, ii) modo Bloch-Floquet con índice efectivo de $n_{\text{B}} = 2.7$, que se corresponde con modo fundamental de una red de difracción nanométrica con $t_{\text{AcWg}} = t\text{Si} = 220\,\text{nm}$, $t_{\text{Etch}} = 70\,\text{nm}$ y $n_{\text{Uc}} = 1.444$. Puede verse que aparecen ventanas de un único haz de radiación para periodos fabricables con litografía *i-line stepper*. En el caso de redes nanométricas esta ventana solo puede aparecer si se utiliza cubierta de aire.

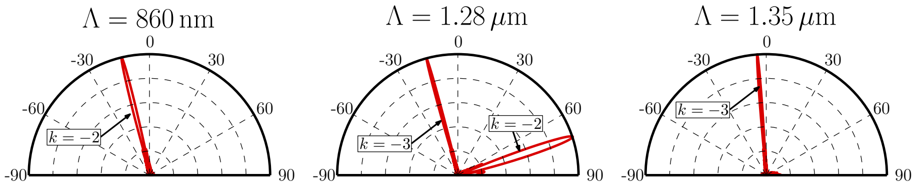

a) b) c)

Figure C.6.: Factor de *array* normalizado para red con $n_{\text{B}} = 3.37$, $n_{\text{Uc}} = 1$, 40 periodos y periodos de **a)** $\Lambda = 860\,\text{nm}$, **b)** $1.28\,\mu\text{m}$, **c)** $1.35\,\mu\text{m}$

Como ejemplo, los factores de *array* para redes con $n_{\text{B}} = 3.37$, $n_{\text{Uc}} = 1$ y periodos de $\Lambda = 860\,\text{nm}$, $1.28\,\mu\text{m}$, $1.35\,\mu\text{m}$ se presentan en las Figs. C.6-a, C.6-b y C.6-c.

Como era de esperar, las redes de difracción con periodos de $\Lambda = 860\,\mathrm{nm}$ y $\Lambda = 1.35\,\mu\mathrm{m}$ (dentro de la región de un único haz de radiación para $k = -2$ y $k = -3$ respectivamente), presentan un único haz de radiación, mientras que la red con $\Lambda = 1.28\,\mu\mathrm{m}$ (fuera de la región de único haz de radiación) presenta dos haces de radiación.

A continuación se discute la caracterización experimental de la red de difracción propuesta

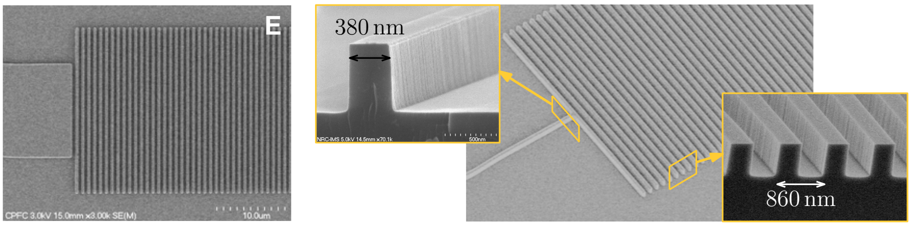

a) b)

Figure C.7.: Imagen de *scanning electron microscope* de la red de acoplo chip fibra fabricada con etapa de excitación basada en: **a)** *taper* directo convencional **b)** *taper* inverso propuesto.

Para verificar experimentalmente el efecto de la etapa de excitación, se caracterizan redes de difracción con etapa de excitación basada en *taper* convencional (Fig. C.7-a) y *taper* inverso (Fig. C.7-b). Se han incluido variaciones en el periodo y el hueco de la red de difracción con el objetivo de compensar los errores de fabricación típicos. Los dispositivos han sido fabricados utilizando *i-line stepper* y *reactive ion etching* en el *Canadian Photonic Fabrication Center* (CPFC).

Los parámetros geométricos de las etapas de excitación fabricadas son:

- *Taper* convencional: ancho inicial de $W_{ini} = 1.3\,\mu\mathrm{m}$, ancho final de $W_{end} = 15\,\mu\mathrm{m}$ y longitud del *taper* de $L_{ConvTaper} = 500\,\mu\mathrm{m}$. Pérdidas de inserción simuladas < $0.1\,\mathrm{dB}$.
- *Taper* inverso: ancho inicial de $W_{ini} = 1.3\,\mu\mathrm{m}$, ancho final de $W_{end} = 380\,\mathrm{nm}$ y longitud del *taper* de $L_{InvTaper} = 1500\,\mu\mathrm{m}$. Pérdidas de inserción simuladas < $0.1\,\mathrm{dB}$.

Dos redes de difracción nominalmente iguales, se sitúan en configuración *back-to-back*, siendo la luz inyectada por una de las redes y extraída por la otra (ver Fig. C.8-a y C.8-b). La luz proveniente de un láser ajustable se acopla al chip usando una fibra monomodo (SMF28) pulida. Se utiliza un controlador de polarización para fijar polarización TE. La luz difractada por la red de salida es recogida por otra fibra monomodo pulida e inyectada a un fotodiodo de InGaAs. La eficiencia de acoplo de una red se obtiene a partir de la potencia medida en el fotodiodo, restando las pérdidas del *setup*, y las pérdidas de propagación de la guía de interconexión, y dividiendo entre dos. Se han estimado unas pérdidas del *setup* de $P_{\mathrm{setup}} = -3.7\,\mathrm{dB}$ a $1550\,\mathrm{nm}$, a partir de la potencia en el fotodiodo de InGaAs, cuando las fibras de entrada salida se conectan directamente (sin el chip). Las pérdidas de la guía de interconexión, de $2.5\,\mathrm{dB/cm}$, han sido determinadas en una medida independiente utilizando la técnica de fase mínima [127].

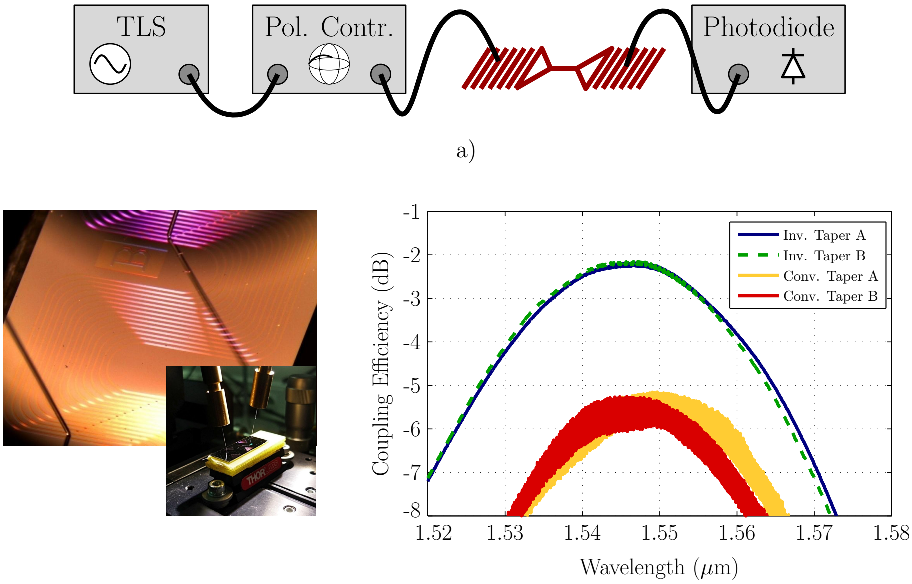

a)

b)

c)

Figure C.8.: a) y **b)** *Setup* de medida para caracterización de redes de difracción en configuración *back-to-back*. **c)** Eficiencia de acoplo experimental para dos realizaciones distintas de redes de difracción con etapas de excitación basadas en *tapers* directo e inverso.

La eficiencia de acoplo medida, se representa en la Fig. C.8-c para dos parejas distintas de redes de difracción con *tapers* convencional e inverso. Las redes de difracción con *taper* inverso optimizado presentan una eficiencia de acoplo medida máxima de $-2.2\,\mathrm{dB}$ con un ancho de banda a $3\,\mathrm{dB}$ de $40\,\mathrm{nm}$, que supera al estado del arte de redes de difracción no apodizadas de un solo paso de grabado en guías SOI nanométricas sin reflectores inferiores. Esta eficiencia, además, supone una mejora de $3.3\,\mathrm{dB}$ respecto a las redes con *taper* convencional que presentan una eficiencia de acoplo medida de $-5.5\,\mathrm{dB}$. El efecto de reducción de las reflexiones producido por el uso de un *taper* inverso puede apreciarse claramente en la amplitud del rizado de Fabry-Perot. Utilizando la técnica de la fase mínima, se estiman unas reflexiones de un 8% para el caso del *taper* convencional, lo que supone una penalización de diez veces, comparada con el caso del *taper* inverso. Se puede apreciar un ligero desplazamiento de la eficiencia de acoplo máxima ($\sim 5\,\mathrm{nm}$) que puede ser atribuido a una reducción del índice efectivo del modo Bloch-Floquet, producido por un sobre-grabado.

Estos resultados demuestran por primera vez, que se pueden implementar redes de difracción en guías micrométricas con eficiencias de acoplo comparables e incluso superiores a aquellas implementadas sobre guías SOI nanométricas.

C.2.2. Red de difracción independiente de la polarización

Como dispositivos interferométricos que son, las redes de difracción son muy sensibles a variaciones en el índice efectivo del modo que se propaga a través de ellas. En concreto, el ángulo de radiación y la direccionalidad, dependen directamente de este índice efectivo. Por tanto, la gran birrefringencia de las redes de difracción implementadas sobre guías nanométricas en silicio, hace que dichas redes sean diseñadas habitualmente para trabajar con una única polarización. En aplicaciones donde no se usan fibras mantenedoras de la polarización, el estado de polarización a la entrada es desconocido. Por esto, y con el objetivo de evitar pérdidas de inserción no deseadas, sería deseable tener redes de difracción que presentaran una eficiencia de acoplo independiente de la polarización.

Las guías micrométricas presentan una birrefringencia mucho menor que la de las guías nanométricas. De esta manera se puede conseguir reducir la diferencia entre los ángulos de radiación para las polarizaciones TE y TM a tan solo $5°$, mientras que para el caso de las redes de difracción nanométricas dicha diferencia es del orden de $30°$. De cualquier modo, la direccionalidad de la red es todavía muy dependiente de la polarización utilizada. Para superar esta limitación, se ha propuesto el uso de un espejo o reflector debajo de la zona donde se encuentra la red de difracción. Mientras que en los diseños convencionales la posición del reflector se optimiza para obtener una interferencia constructiva para una red de difracción dada, en el diseño propuesto, la posición del reflector está fija y se varía la red de difracción para obtener la interferencia constructiva. Haciendo esto, el reflector puede situarse justo debajo de la capa de BOX, usando el dióxido de silicio como capa de parada para el proceso de eliminación selectiva del substrato. Esta solución simplifica el proceso de fabricación, y alivia las tolerancias a errores en la posición del reflector, producidas por desviaciones en el proceso de fabricación. El diseño optimizado con una capa fina de oro actuando como reflector presenta una eficiencia de acoplo de $CE = -3\,\mathrm{dB}$ para las dos polarizaciones [69].

C.2.3. Red de difracción para espectrómetro integrado

Las prestaciones de los espectrómetros integrados están estrechamente ligadas a su capacidad de colección de luz. De esta manera, el microespectrómetro de transformada de Fourier multiapertura se beneficia de la mayor capacidad de colección de luz que le otorga el hecho de tener múltiples aperturas de entrada [122]. De cualquier modo, en aperturas basadas en acoplo por el borde del chip, el área de colección de luz está limitada a una línea a lo largo de dicho borde. El objetivo de esta parte del trabajo es desarrollar un interfaz de entrada mejorado para dicho microespectrómetro de transformada de Fourier multiapertura para monitorización de absorción de vapor de agua en la atmósfera [71,72]. Este trabajo se ha realizado en colaboración con el *National Research Council* en Canadá, la empresa Comdev, y la *Canadian Space Agency* (CSA).

Las redes de difracción pueden situarse en cualquier lugar dentro de la superficie del chip, superando las limitaciones de las soluciones basadas en acoplo por el borde del chip. Para mejorar la capacidad de colección de luz del sistema, se utiliza un *array* de redes de difracción (compuesto por seis redes de difracción de $15\,\mu\mathrm{m}$ x $90\,\mu\mathrm{m}$) para implementar una superficie de colección de luz de $90\,\mu\mathrm{m}$ x $90\,\mu\mathrm{m}$. El interfaz de entrada optimizado presenta una eficiencia de acoplo medida de $-4.5\,\mathrm{dB}$ a una longitud de onda de $1354\,\mathrm{nm}$, que se corresponde con el pico de absorción del vapor de agua [72].

C.3. Rotadores de polarización integrados

Muchos grupos de investigación desarrollan trabajos y proyectos que tienen como objetivo el desarrollo de rotadores de polarización que sean robustos a errores de fabricación y a la vez fáciles de fabricar. Con esto, se espera mejorar las prestaciones, la fiabilidad, el coste y el rendimiento de fabricación en receptores para sistemas de comunicaciones basados en multiplexación por polarización monolíticamente integrados. Además, los dispositivos que implementan sistemas basados en diversidad de polarización, también pueden verse beneficiados por el desarrollo de dichos rotadores de polarización.

C.3.1. Rotador de polarización para guías en InP

La solución preferida para la implementación de rotadores de polarización integrados en la plataforma de fosfuro de indio son las guías rotadoras inclinadas [51–53]. Estas guías rotadoras tienen una pared recta grabada hasta el fondo, y una pared inclinada. La integración de estas guías rotadoras inclinadas junto con las guías de interconexión *rib* utilizadas normalmente, requeriría de tres pasos de grabado: uno seco (poco profundo) para definir las guías de interconexión, uno seco (profundo) para definir la pared recta de la guía rotadora, y uno húmedo para definir la pared inclinada de la guía rotadora. Estos pasos de grabado extra afectan negativamente a los costes de fabricación del dispositivo.

Para evitar la necesidad de utilizar un paso de grabado húmedo, se propone el uso de una guía rotadora con una geometría alternativa. En la guía rotadora propuesta, la pared inclinada es sustituida por dos escalones. Esto puede verse como una aproximación de primer orden de la pared inclinada. Haciendo esto, la integración de la guía rotadora con el resto del circuito requeriría de sólo dos pasos de grabado secos: uno poco profundo para definir las guías de interconexión y el primer escalón de la guía rotadora, y otro profundo para definir el segundo escalón de la guía rotadora.

Se ha diseñado una guía rotadora basada en la geometría de dos escalones propuesta. El diseño es perfectamente compatible con un receptor de una polarización desarrollado previamente por el grupo. El dispositivo presenta un ratio de extinción de $40\,\mathrm{dB}$ [75].

C.3.2. Rotador de polarización ajustable

Además del, a veces, complicado proceso de fabricación de los rodatores integrados, uno de sus principales problemas viene de las bajas tolerancias a errores de fabricación que presentan. Estas, limitan seriamente sus prestaciones y su rendimiento de fabricación. Las guías rotadoras se basan en el uso de una geometría transversal concreta para proporcionar modos híbridos con un ángulo y un desfase concretos, que permiten realizar la rotación. Estos dos parámetros (ángulo y desfase) se ven muy afectados por pequeñas variaciones de las dimensiones de la guía. De hecho el ratio de extinción puede llegar a caer por debajo de $5\,\mathrm{dB}$ para variaciones en la geometría del orden de un $5\,\%$.

Otro de los resultados más relevantes de este trabajo es el desarrollo de un nuevo esquema de rotación que permite mejorar las tolerancias de fabricación de manera substancial. El esquema se compone de tres secciones de guía rotadora interconectadas mediante desfasadores ajustables. Controlando el desfase introducido por estos desfasadores ajustables, que pueden ser implementados con calentadores sobre las guías, se pueden corregir las desviaciones producidas por los errores de fabricación. De este modo se puede conseguir una rotación perfecta aun en presencia de errores [77]. Además, el sistema propuesto permite elegir de manera dinámica la longitud de onda central de trabajo. Se han desarrollado analíticamente las condiciones necesarias para poder asegurar una rotación perfecta, demostrando que esta se puede obtener utilizando rotadores con desviaciones de hasta un $\pm 60\,\%$ en el ángulo y el desfase de los modos híbridos.

C.4. Receptor coherente de doble-polarización sin separador de polarización

Los receptores comerciales para sistemas basados en multiplexación por polarización, duplican los receptores de una polarización ya existentes, y utilizan un separador de polarización implementado fuera del chip para inyectar una polarización distinta a cada uno de ellos. Aunque la integración monolítica del separador de polarización junto con el resto de elementos del receptor podría, en principio, mejorar la fiabilidad, el tamaño y en último término el precio de los receptores, debido a las reducidas tolerancias de los separadores de polarización integrados, estos se implementan fuera del chip.

Se ha propuesto una arquitectura de receptor alternativa, que permite demodular señales multiplexadas en polarización sin necesidad de utilizar rotadores ni separadores de polarización. El manejo de polarización se consigue diseñando adecuadamente la birrefringencia de las guías de interconexión. El receptor resultante, presenta unas tolerancias de fabricación elevadas. Las simulaciones electromagnéticas y de sistema realizadas muestran que la degradación de las prestaciones del receptor para variaciones en el ancho de las guías de $\pm 200\,\mathrm{nm}$ es negligible. Esta estrategia de diseño, abre las puertas hacia un camino completamente novedoso que permite la integración de receptores para sistemas basados en multiplexación por polarización sin necesidad de utilizar ningún tipo de ajuste activo.

Bibliography

[1] Photonics & RF Group in Universidad de Málaga. [Online]. Available: www.photonics-rf.uma.es/

[2] S. E. Miller, “Integrated optics: an introduction,” *Bell Sys. Tech. J.*, vol. 48, no. 7, pp. 2059–2069, 1969.

[3] T. H. Maiman, “Stimulated optical radiation in ruby,” *Nature*, vol. 187, no. 4736, pp. 493–494, 1960.

[4] R. Hall, G. Fenner, J. Kingsley, T. Soltys, and R. Carlson, “Coherent light emission from Ga-As junctions,” *Phys. Rev. Lett*, vol. 9, no. 9, pp. 366–369, 1962.

[5] M. I. Nathan, W. P. Dumke, G. Burns, F. H. Dill, and G. Lasher, “Stimulated emission of radiation from GaAs p-n junctions,” *Appl. Phys. Lett.*, vol. 1, no. 3, pp. 62–64, 1962.

[6] N. Holonyak Jr. and S. Bevacqua, “Coherent (visible) light emission from Ga (As1- xPx) junctions,” *Appl. Phys. Lett.*, vol. 1, no. 4, pp. 82–83, 1962.

[7] T. Quist, R. Rediker, R. Keyes, W. Krag, B. Lax, A. L. McWhorter, and H. Zeigler, “Semiconductor maser of GaAs,” *Appl. Phys. Lett.*, vol. 1, no. 4, pp. 91–92, 1962.

[8] I. P. Kaminow, “Optical integrated circuits: a personal perspective,” *J. Lightwave Technol.*, vol. 26, no. 9, pp. 994–1004, 2008.

[9] H. Liu, C. F. Lam, and C. Johnson, “Scaling optical interconnects in datacenter networks,” in *18th Symposium of High Perforfamnce Interconnects*. IEEE, 2010, pp. 113–116.

[10] Y. A. Vlasov, “Silicon CMOS-integrated nano-photonics for computer and data communications beyond 100G,” *IEEE Commun. Mag.*, vol. 50, no. 2, pp. s67–s72, 2012.

[11] C. Gunn, “CMOS photonics for high-speed interconnects,” *IEEE Micro*, vol. 26, no. 2, pp. 58–66, 2006.

[12] Optical Internetworking Forum (OIF) implementation agreement for next generation interconnect framework. [Online]. Available: http://www.oiforum.com/public/documents/OIF-FD-Client-400G-1T-01.0.pdf

[13] L. Wosinski and Z. Wang, “Integrated silicon nanophotonics: a solution for computer interconnects,” in *International Conference on Transparent Optical Networks (ICTON)*. IEEE, 2011, pp. 1–4.

[14] L. Pavesi and D. J. Lockwood, *Silicon photonics*. Springer, 2004, vol. 1.

[15] D. J. Lockwood and L. Pavesi, *Silicon Photonics II*. Springer, 2011.

[16] L. Vivien and L. Pavesi, *Handbook of Silicon Photonics*. CRC Press, 2013.

[17] S. Assefa, W. M. Green, A. Rylyakov, C. Schow, F. Horst, and Y. Vlasov, "CMOS integrated nanophotonics: enabling technology for exascale computing systems," in *Optical Fiber Communications Conference (OFC)*. OSA, 2011, pp. 1–4.

[18] M. Salib, M. Morse, and M. Paniccia, "Opportunities and integration challenges for CMOS-compatible silicon photonic and optoelectronic devices," in *International Conference on Group IV Photonics (GFP)*. IEEE, 2004, pp. 1–6.

[19] X. Zheng, F. Y. Liu, J. Lexau, D. Patil, G. Li, Y. Luo, H. D. Thacker, I. Shubin, J. Yao, K. Raj, R. Ho, J. Cunningham, and A. V. Krishnamoorthy, "Ultralow power 80 Gb/s arrayed CMOS silicon photonic transceivers for WDM optical links," *J. Lightwave Technol.*, vol. 30, no. 4, pp. 641–650, 2012.

[20] R. Soref, "Mid-infrared photonics in silicon and germanium," *Nat. Photonics*, vol. 4, no. 8, pp. 495–497, 2010.

[21] M.-C. Estévez, M. Álvarez, and L. M. Lechuga, "Integrated optical devices for lab-on-a-chip biosensing applications," *Laser & Photon. Rev.*, vol. 6, no. 4, pp. 463–487, 2012.

[22] D. Marpaung, C. Roeloffzen, R. Heideman, A. Leinse, S. Sales, and J. Capmany, "Integrated microwave photonics," *Laser & Photon. Rev.*, vol. 7, no. 4, pp. 506–538, 2013.

[23] J. Fandiño, J. Doménech, P. Muñoz, and J. Capmany, "Integrated inp frequency discriminator for phase-modulated microwave photonic links," *Opt. Express*, vol. 21, no. 3, pp. 3726–3736, 2013.

[24] C. Kopp, S. Bernabe, B. B. Bakir, J.-M. Fédéli, R. Orobtchouk, F. Schrank, H. Porte, L. Zimmermann, and T. Tekin, "Silicon photonic circuits: on-CMOS integration, fiber optical coupling, and packaging," *IEEE J. Select. Topics Quantum Electron.*, vol. 17, no. 3, pp. 498–509, 2011.

[25] A. Mekis, S. Gloeckner, G. Masini, A. Narasimha, T. Pinguet, S. Sahni, and P. De Dobbelaere, "A grating-coupler-enabled CMOS photonics platform," *IEEE J. Sel. Top. Quantum Electron.*, vol. 17, no. 3, pp. 597–608, 2011.

[26] D. Taillaert, W. Bogaerts, P. Bienstman, T. F. Krauss, P. Van Daele, I. Moerman, S. Verstuyft, K. De Mesel, and R. Baets, "An out-of-plane grating coupler for efficient butt-coupling between compact planar waveguides and single-mode fibers," *IEEE J. Quantum Electron.*, vol. 38, no. 7, pp. 949–955, 2002.

[27] L. Vivien, D. Pascal, S. Lardenois, D. Marris-Morini, E. Cassan, F. Grillot, S. Laval, J.-M. Fédéli, and L. El Melhaoui, "Light injection in SOI microwaveguides using high-efficiency grating couplers," *J. Lightwave Technol.*, vol. 24, no. 10, pp. 3810–3815, 2006.

[28] W. S. Zaoui, A. Kunze, W. Vogel, M. Berroth, J. Butschke, F. Letzkus, and J. Burghartz, “Bridging the gap between optical fibers and silicon photonic integrated circuits,” *Opt. Express*, vol. 22, no. 2, pp. 1277–1286, 2014.

[29] R. Halir, P. Cheben, S. Janz, D.-X. Xu, I. Molina-Fernández, and J. G. Wangüemert-Pérez, “Waveguide grating coupler with subwavelength microstructures,” *Opt. Lett.*, vol. 34, no. 9, pp. 1408–1410, 2009.

[30] R. Halir, P. Cheben, J. Schmid, R. Ma, D. Bedard, S. Janz, D.-X. Xu, A. Densmore, J. Lapointe, and I. Molina-Fernández, “Continuously apodized fiber-to-chip surface grating coupler with refractive index engineered subwavelength structure,” *Opt. Lett.*, vol. 35, no. 19, pp. 3243–3245, 2010.

[31] Y. Li, L. Li, B. Tian, G. Roelkens, and R. Baets, “Reflectionless tilted grating couplers with improved coupling efficiency based on a silicon overlay,” *Opt. Express*, vol. 25, no. 13, pp. 1195–1198, 2013.

[32] B. Wang, J. Jiang, and G. P. Nordin, “Embedded slanted grating for vertical coupling between fibers and silicon-on-insulator planar waveguides,” *IEEE Photonics Technol. Lett.*, vol. 17, no. 9, pp. 1884–1886, 2005.

[33] G. Roelkens, D. V. Thourhout, and R. Baets, “High efficiency grating coupler between silicon-on-insulator waveguides and perfectly vertical optical fibers,” *Opt. Lett.*, vol. 32, no. 11, pp. 1495–1497, 2007.

[34] C. Li, H. Zhang, M. Yu, and G. Lo, “CMOS-compatible high efficiency double-etched apodized waveguide grating coupler,” *Opt. Express*, vol. 21, no. 7, pp. 7868–7874, 2013.

[35] X. Chen and H. K. Tsang, “Polarization-independent grating couplers for silicon-on-insulator nanophotonic waveguides,” *Opt. Lett.*, vol. 36, no. 6, pp. 796–798, 2011.

[36] W. S. Zaoui, A. Kunze, W. Vogel, and M. Berroth, “CMOS-compatible polarization splitting grating couplers with a backside metal mirror,” *IEEE Photonics Technol. Lett.*, vol. 25, no. 14, pp. 1395–1397, 2013.

[37] Z. Cheng, X. Chen, C. Yan Wong, K. Xu, and H. Ki Tsang, “Broadband focusing grating couplers for suspended-membrane waveguides,” *Opt. Lett.*, vol. 37, no. 24, pp. 5181–5183, 2012.

[38] Y. Ding, H. Ou, and C. Peucheret, “Ultrahigh-efficiency apodized grating coupler using fully etched photonic crystals,” *Opt. Lett.*, vol. 38, no. 15, pp. 2732–2734, 2013.

[39] M. Fan, M. Popović, and F. X. Kärtner, “High directivity, vertical fiber-to-chip coupler with anisotropically radiating grating teeth,” in *Conference on Lasers and Electro-Optics (CLEO)*. OSA, 2007, pp. CTuDD3–1–CTuDD3–2.

[40] Z. Can, S. Jing-Hua, X. Xi, S. Wei-Min, Z. Xiao-Jun, C. Tao, Y. Jin-Zhong, and Y. Yu-De, “High efficiency grating coupler for coupling between single-mode fiber and SOI waveguides,” *Chin. Phys. Lett*, vol. 30, no. 1, p. 014207, 2013.

[41] D. Taillaert, H. Chong, P. I. Borel, L. H. Frandsen, R. De La Rue, and R. Baets, “A compact two-dimensional grating coupler used as a polarization splitter,” *IEEE Photonics Technol. Lett.*, vol. 15, no. 9, pp. 1249–1251, 2003.

[42] K. Qin, D. Gao, C. Bao, Z. Zhao, X. Zhou, T. Lu, and L. Chen, “High efficiency and broadband two-dimensional blazed grating coupler with fully etched triangular holes,” *J. Lightwave Technol.*, vol. 30, no. 14, pp. 2363–2366, 2012.

[43] M. Cherchi, S. Ylinen, M. Harjanne, M. Kapulainen, and T. Aalto, “Dramatic size reduction of waveguide bends on a micron-scale silicon photonic platform,” *Opt. Express*, vol. 21, no. 15, pp. 17 814–17 823, 2013.

[44] N.-N. Feng, D. Feng, S. Liao, X. Wang, P. Dong, H. Liang, C.-C. Kung, W. Qian, J. Fong, R. Shafiiha, Y. Luo, J. Cunningham, A. V. Krishnamoorthy, and M. Asghari, “30GHz Ge electro-absorption modulator integrated with 3μm silicon-on-insulator waveguide,” *Opt. Express*, vol. 19, no. 8, pp. 7062–7067, 2011.

[45] R. Nagarajan, M. Kato, J. Pleumeekers, P. Evans, S. Corzine, S. Hurtt, A. Dentai, S. Murthy, M. Missey, S. Muthiah, Ranjani Randal A., J. C., R. Schneider, M. Zarai, F. A. Kish, and D. Welch, “InP photonic integrated circuits,” *IEEE J. Select. Topics Quantum Electron.*, vol. 16, no. 5, pp. 1113–1125, 2010.

[46] P. Runge, S. Schubert, A. Seeger, K. Janiak, J. Stephan, D. Trommer, P. Domburg, and M. L. Nielsen, “Monolithic InP receiver chip with a 90° hybrid and 56 GHz balanced photodiodes,” *Opt. Express*, vol. 20, no. 26, pp. B250–B255, 2012.

[47] Mirthe project: Monolithic InP-based dual polarization QPSK integrated receiver and transmitter for coherent 100-400Gb Ethernet. [Online]. Available: http://www.ist-mirthe.eu/

[48] T. Barwicz, M. R. Watts, M. A. Popović, P. T. Rakich, L. Socci, F. X. Kärtner, E. P. Ippen, and H. I. Smith, “Polarization-transparent microphotonic devices in the strong confinement limit,” *Nat. Photonics*, vol. 1, no. 1, pp. 57–60, 2007.

[49] D. Dai and J. E. Bowers, “Novel concept for ultracompact polarization splitter-rotator based on silicon nanowires,” *Opt. Express*, vol. 19, no. 11, pp. 10 940–10 949, 2011.

[50] L. Liu, Y. Ding, K. Yvind, and J. M. Hvam, “Silicon-on-insulator polarization splitting and rotating device for polarization diversity circuits,” *Opt. Express*, vol. 19, no. 13, pp. 12 646–12 651, 2011.

[51] H. Deng, D. O. Yevick, C. Brooks, and P. E. Jessop, “Design rules for slanted-angle polarization rotators,” *J. Lightwave Technol.*, vol. 23, no. 1, pp. 432–445, 2005.

[52] H. El-Refaei, D. Yevick, and T. Jones, “Slanted-rib waveguide InGaAsP-InP polarization converters,” *J. Lightwave Technol.*, vol. 22, no. 5, pp. 1352–1357, 2004.

[53] L. Augustin, J. van der Tol, E. J. Geluk, and M. Smit, “Short polarization converter optimized for active-passive integration in InGaAsP-InP,” *IEEE Photonics Technol. Lett.*, vol. 19, no. 20, pp. 1673–1675, 2007.

[54] D. M. Beggs, M. Midrio, and T. F. Krauss, “Compact polarization rotators for integrated polarization diversity in InP-based waveguides,” *Opt. Lett.*, vol. 32, no. 15, pp. 2176–2178, 2007.

[55] S.-H. Kim, R. Takei, Y. Shoji, and T. Mizumoto, “Single-trench waveguide TE-TM mode converter,” *Opt. Express*, vol. 17, no. 14, pp. 11 267–11 273, 2009.

[56] A. V. Velasco, M. L. Calvo, P. Cheben, A. Ortega-Moñux, J. H. Schmid, **C. Alonso-Ramos**, I. Molina Fernández, J. Lapointe, M. Vachon, S. Janz, and D.-X. Xu, “Ultracompact polarization converter with a dual subwavelength trench built in a silicon-on-insulator waveguide,” *Opt. Lett.*, vol. 37, no. 3, pp. 365–367, 2012.

[57] M. Kotlyar, L. Bolla, M. Midrio, L. O’Faolain, and T. Krauss, “Compact polarization converter in InP-based material,” *Opt. Express*, vol. 13, no. 13, pp. 5040–5045, 2005.

[58] Z. Wang and D. Dai, “Ultrasmall si-nanowire-based polarization rotator,” *J. Opt. Soc. Am. B*, vol. 25, no. 5, pp. 747–753, 2008.

[59] L. Coldren, M. Lu, L. Johansson, M. Rodwell, and J. Parker, “Single-chip integrated transmitters and receivers,” *Opt. Express*, vol. 20, no. 26, pp. B377–B385, 2012.

[60] F. A. Kish, D. Welch, R. Nagarajan, J. L. Pleumeekers, V. Lal, M. Ziari, A. Nilsson, M. Kato, S. Murthy, P. Evans *et al.*, “Current status of large-scale InP photonic integrated circuits,” *IEEE J. Select. Topics Quantum Electron.*, vol. 17, no. 6, pp. 1470–1489, 2011.

[61] **C. Alonso-Ramos**, A. Ortega-Moñux, I. Molina-Fernández, P. Cheben, L. Zavargo-Peche, and R. Halir, “Efficient fiber-to-chip grating coupler for micrometric SOI rib waveguides,” *Opt. Express*, vol. 18, no. 14, pp. 15 189–15 200, 2010.

[62] **C. Alonso-Ramos**, A. Ortega-Moñux, I. Molina-Fernández, P. Cheben, L. Zavargo-Peche, R. Halir, N. Kim, S. Janz, and D. Xu, “Design of an optimized grating coupler for thick SOI rib waveguides,” in *International Conference on Information Photonics (IP)*. IEEE, 2011, pp. 1–3.

[63] **C. Alonso-Ramos**, A. Ortega-Moñux, L. Zavargo-Peche, R. Halir, J. de Oliva-Rubio, I. Molina-Fernández, P. Cheben, D.-X. Xu, and S. Janz, “Single-etch grating coupler for micrometric silicon rib waveguides,” *Opt. Lett.*, vol. 36, no. 14, pp. 2647–2649, 2011.

[64] **C. Alonso-Ramos**, A. Ortega-Moñux, L. Zavargo-Peche, R. Halir, J. de Oliva-Rubio, I. Molina-Fernández, P. Cheben, D.-X. Xu, S. Janz, and N. Kim, "Efficient fibre-chip grating coupler for thick SOI rib waveguides," in *European Conference and Exposition on Optical Communications (ECOC)*. OSA, 2011, pp. 1–3.

[65] **C. Alonso-Ramos**, A. Ortega-Moñux, I. Molina-Fernández, P. Cheben, L. Zavargo-Peche, R. Halir, S. Janz, D.-X. Xu, N. Kim, and B. Lamontagne, "Grating couplers for thick SOI rib waveguides," *Opt. Quantum. Electron.*, vol. 44, no. 12-13, pp. 535–540, 2012.

[66] P. Cheben, J. Schmid, **C. Alonso-Ramos**, R. Halir, L. Zavargo-Peche, J. Lapointe, P. Bock, D.-X. Xu, S. Janz, A. Ortega-Moñux, I. Molina-Fernández, R. Ma, A. Delâge, and J.-M. Fédéli, "Diffractive and subwavelength grating couplers for microphotonic waveguides," in *International Conference on Transparent Optical Networks (ICTON)*. IEEE, 2012, pp. 1–4.

[67] N. Na, H. Frish, I.-W. Hsieh, O. Harel, R. George, A. Barkai, and H. Rong, "Efficient broadband silicon-on-insulator grating coupler with low backreflection," *Opt. Lett.*, vol. 36, no. 11, pp. 2101–2103, 2011.

[68] J. S. Levy, D. Feng, W. Qian, H. Liang, R. Shafiiha, A. V. Krishnamoorthy, and M. Asghari, "High efficiency grating coupler for 3 μm SOI waveguides," in *International Conference on Group IV Photonics (GFP)*. IEEE, 2012, pp. 183–185.

[69] **C. Alonso-Ramos**, L. Zavargo-Peche, A. Ortega-Moñux, R. Halir, I. Molina-Fernández, and P. Cheben, "Polarization-independent grating coupler for micrometric silicon rib waveguides," *Opt. Lett.*, vol. 37, no. 17, pp. 3663–3665, 2012.

[70] **C. Alonso-Ramos**, A. Ortega-Moñux, R. Halir, L. Zavargo-Peche, I. Molina-Fernández, P. Cheben, D.-X. Xu, and S. Janz, "Grating couplers in thick rib SOI waveguides for TE and TM polarizations," in *Photonics Europe*. SPIE, 2012, pp. 84 310E–84 310E–7.

[71] A. Scott, P. Bock, **C. Alonso-Ramos**, B. Lamontagne, P. Cheben, M. Florjańczyk, I. Molina-Fernández, S. Janz, A. Ortega-Moñux, B. Solheim, and D.-X. Xu, "Improved coupling to integrated spatial heterodyne spectrometers with applications to space," in *Reliability, Packaging, Testing, and Characterization of MEMS/MOEMS and Nanodevices*. SPIE, 2011, pp. 79 280K–79 280K.

[72] P. Cheben, M. Florjańczyk, P. Bock, **C. Alonso-Ramos**, B. Lamontagne, A. Bogdanov, S. Janz, D.-X. Xu, M. Vachon, A. Scott, A. Ortega-Moñux, I. Molina-Fernández, B. Solheim, and K. Sinclair, "Recent advances in Fourier-transform waveguide spectrometers," in *International Conference on Transparent Optical Networks (ICTON)*. IEEE, 2011, pp. 1–4.

[73] M. Florjańczyk, **C. Alonso-Ramos**, P. Bock, A. Bogdanov, P. Cheben, I. Molina-Fernández, S. Janz, B. Lamontagne, A. Ortega-Moñux, A. Scott, K. Sinclair, B. Solheim, and D.-X. Xu, "Development of a Fourier-transform waveguide spectrometer for space applications," *Opt. Quantum. Electron.*, vol. 44, no. 12-13, pp. 549–556, 2012.

[74] 100GET: 100 Gbit/s carrier-grade ethernet transport technologies. [Online]. Available: http://www.celtic-initiative.org/Projects/Celtic-projects/Call4/100GET/Project-default.asp

[75] **C. Alonso-Ramos**, S. Romero-García, A. Ortega-Moñux, I. Molina-Fernández, R. Zhang, H. Bach, and M. Schell, "Polarization rotator for InP rib waveguide," *Opt. Lett.*, vol. 37, no. 3, pp. 335–337, 2012.

[76] **C. Alonso-Ramos**, L. Vivien, P. Cheben, R. Halir, D. Marris-Morini, A. Ortega-Moñux, I. Molina-Fernández, J. Schmid, S. Janz, and D.-X. Xu, "Highly tolerant and tuneable integrated optical polarization rotator," France Patent PCT/FR2012/051 001, 2012.

[77] **C. Alonso-Ramos**, R. Halir, A. Ortega-Moñux, P. Cheben, L. Vivien, I. Molina-Fernández, D. Marris-Morini, S. Janz, D.-X. Xu, and J. Schmid, "Highly tolerant tunable waveguide polarization rotator scheme," *Opt. Lett.*, vol. 37, no. 17, pp. 3534–3536, 2012.

[78] ——, "A general approach for robust integrated polarization rotators," in *Integrated Optics: Physics and Simulations*. SPIE, 2013, pp. 878 109–878 109–8.

[79] **C. Alonso-Ramos**, P. Reyes-Iglesias, A. Ortega-Moñux, I. Molina-Fernández, and R. Halir, "Downconverter integrado con diversidad de polarización para receptor óptico coherente con multiplexación por polarización," Spanish Patent ES2014/201 300 742, 2014.

[80] **C. Alonso-Ramos**, P. Reyes-Iglesias, A. Ortega-Moñux, D. Pérez-Galacho, R. Halir, and I. Molina-Fernández, "PBS-less integrated dual-polarization coherent receiver," *Opt. Lett.*, *Under review*.

[81] S. Romero-García, F. Merget, F. Zhong, H. Finkelstein, and J. Witzens, "Silicon nitride cmos-compatible platform for integrated photonics applications at visible wavelengths," *Opt. Express*, vol. 21, no. 12, pp. 14 036–14 046, 2013.

[82] R. Halir, A. Ortega-Moñux, I. Molina-Fernández, J. G. Wangüemert-Pérez, P. Cheben, D.-X. Xu, B. Lamontagne, and S. Janz, "Compact high-performance multimode interference couplers in silicon-on-insulator," *IEEE Photon. Technol. Lett.*, vol. 21, no. 21, pp. 1600–1602, 2009.

[83] W. N. Ye, D.-X. Xu, S. Janz, P. Cheben, M.-J. Picard, B. Lamontagne, and N. G. Tarr, "Birefringence control using stress engineering in silicon-on-insulator (soi) waveguides," *J. Lightwave Technol.*, vol. 23, no. 3, p. 1308, 2005.

[84] A. Densmore, S. Janz, R. Ma, J. H. Schmid, D.-X. Xu, A. Delâge, J. Lapointe, M. Vachon, and P. Cheben, "Compact and low power thermo-optic switch using folded silicon waveguides," *Opt. Express*, vol. 17, no. 13, pp. 10 457–10 465, 2009.

[85] P. J. Bock, P. Cheben, J. H. Schmid, J. Lapointe, A. Delâge, D.-X. Xu, S. Janz, A. Densmore, and T. J. Hall, "Subwavelength grating crossings for silicon wire waveguides," *Opt. Express*, vol. 18, no. 15, pp. 16 146–16 155, 2010.

[86] D.-X. Xu, J. H. Schmid, G. T. Reed, G. Z. Mashanovich, D. J. Thomson, M. Nedeljkovic, X. Chen, D. Van Thourhout, S. Keyvaninia, and S. K. Selvaraja, “Silicon photonic integration platform, have we found the sweet spot,” *IEEE J. Select. Topics Quantum Electron.*, vol. 20, no. 4, p. 8100217, 2014.

[87] A. Barkai, A. Liu, D. Kim, R. Cohen, N. Elek, H.-H. Chang, B. H. Malik, R. Gabay, R. Jones, M. Paniccia, and N. Izhaky, “Double-stage taper for coupling between SOI waveguides and single-mode fiber,” *J. Lightwave Technol.*, vol. 26, no. 24, pp. 3860–3865, 2008.

[88] A. Delâge, S. Janz, B. Lamontagne, A. Bogdanov, D. Dalacu, D.-X. Xu, and K. Yap, “Monolithically integrated asymmetric graded and step-index couplers for microphotonic waveguides,” *Opt. Express*, vol. 14, no. 1, pp. 148–161, 2006.

[89] N. Fang, Z. Yang, A. Wu, J. Chen, M. Zhang, S. Zou, and X. Wang, “Three-dimensional tapered spot-size converter based on (111) silicon-on-insulator,” *IEEE Photonics Technol. Lett.*, vol. 21, no. 12, pp. 820–822, 2009.

[90] L. Vivien, S. Laval, E. Cassan, X. L. Roux, and D. Pascal, “2-D taper for low-loss coupling between polarization-insensitive microwaveguides and single-mode optical fibers,” *J. Lightwave Technol.*, vol. 21, no. 10, pp. 2429–2434, 2003.

[91] V. R. Almeida, R. R. Panepucci, and M. Lipson, “Nanotaper for compact mode conversion,” *Opt. Lett.*, vol. 28, no. 15, pp. 1302–1304, 2003.

[92] K. K. Lee, D. R. Lim, D. Pan, C. Hoepfner, W.-Y. Oh, K. Wada, L. C. Kimerling, K. P. Yap, and M. Doan, “Mode transformer for miniaturized optical circuits,” *Opt. Lett.*, vol. 30, no. 5, pp. 498–500, 2005.

[93] R. Takei, M. Suzuki, E. Omoda, S. Manako, T. Kamei, M. Mori, and Y. Sakakibara, “Silicon knife-edge taper waveguide for ultralow-loss spot-size converter fabricated by photolithography,” *Appl. Phys. Lett*, vol. 102, no. 10, pp. 101 108–101 108, 2013.

[94] P. Cheben, D.-X. Xu, S. Janz, and A. Densmore, “Subwavelength waveguide grating for mode conversion and light coupling in integrated optics,” *Opt. Express*, vol. 14, no. 11, pp. 4695–4702, 2006.

[95] J. Ctyrokỳ, P. Kwiecien, I. Richter, and P. Cheben, “Analysis of couplers between photonic nanowires and subwavelength grating waveguides,” in *Integrated Optics: Physics and Simulations*. SPIE, 2013, pp. 87 810B–87 810B.

[96] C. M. Weinert and H. Heidrich, “Integrated optical beam spread transformer,” May 29 2001, US Patent 6,240,233.

[97] P. Dumon, W. Bogaerts, R. Baets, J.-M. Fédéli, and L. Fulbert, “Towards foundry approach for silicon photonics: silicon photonics platform ePIXfab,” *Electron. Lett.*, vol. 45, no. 12, pp. 581–582, 2009.

[98] W. Bogaerts, D. Taillaert, P. Dumon, D. Van Thourhout, and R. Baets, “A polarization-diversity wavelength duplexer circuit in silicon-on-insulator photonic wires,” *Opt. Express*, vol. 15, no. 4, pp. 1567–1578, 2007.

[99] S. Janz, D.-X. Xu, M. Vachon, N. Sabourin, P. Cheben, H. McIntosh, H. Ding, S. Wang, J. Schmid, A. Delâge, J. Lapointe, A. Densmore, R. Ma, W. Sinclair, S. Logan, R. MacKenxie, Q. Liu, D. Zhang, G. Lopinski, O. Mozenson, M. Gilmour, and H. Tabor, “Photonic wire biosensor microarray chip and instrumentation with application to serotyping of Escherichia coliisolates,” *Opt. Express*, vol. 21, no. 4, pp. 4623–4637, 2013.

[100] J. Yao, X. Zheng, G. Li, I. Shubin, H. Thacker, Y. Luo, K. Raj, J. E. Cunningham, and A. V. Krishnamoorthy, “Grating-coupler based low-loss optical interlayer coupling,” in *International Conference on Group IV Photonics (GFP)*. IEEE, 2011, pp. 383–385.

[101] G. Roelkens, J. Brouckaert, D. Taillaert, P. Dumon, W. Bogaerts, D. Van Thourhout, R. Baets, R. Notzel, and M. Smit, “Integration of InP / InGaAsP photodetectors onto silicon-on-insulator waveguide circuits,” *Opt. Express*, vol. 13, no. 25, pp. 10 102–10 108, 2005.

[102] X. Zheng, S. Lin, Y. Luo, J. Yao, G. Li, S. S. Djordjevic, J.-H. Lee, H. D. Thacker, I. Shubin, K. Raj, J. Cunningham, and A. V. Krishnamoorthy, “Efficient WDM laser sources towards Terabyte/s silicon photonic interconnects,” *J. Lightwave Technol.*, vol. 31, no. 24, pp. 4142–4154, 2013.

[103] D. Taillaert, P. Bienstman, and R. Baets, “Compact efficient broadband grating coupler for silicon-on-insulator waveguides,” *Opt. Lett.*, vol. 29, no. 23, pp. 2749–2751, 2004.

[104] T. Tamir and S. Peng, “Analysis and design of grating couplers,” *Appl. Phys. A-Mater*, vol. 14, pp. 235–254, 1977.

[105] S. F. Helfert and R. Pregla, “Efficient analysis of periodic structures,” *J. Lightwave Technol.*, vol. 16, no. 9, pp. 1694–1702, 1998.

[106] P. J. Bock, P. Cheben, J. H. Schmid, J. Lapointe, A. Delâge, S. Janz, G. C. Aers, D.-X. Xu, A. Densmore, and T. J. Hall, “Subwavelength grating periodic structures in silicon-on-insulator: a new type of microphotonic waveguide,” *Opt. Express*, vol. 18, no. 19, pp. 20 251–20 262, 2010.

[107] L. Stutzman Warren and A. Thiele Gary, *Antenna theory and design*, 1988, Ed. John Wiley & SonsInc., NY.

[108] C. A. Flory, “Analysis of directional grating-coupled radiation in waveguide structures,” *IEEE J. Quantum. Electron.*, vol. 40, no. 7, pp. 949–957, 2004.

[109] J. Yang, Z. Zhou, W. Zhou, X. Zhang, and H. Jia, “High efficient subwavelength binary blazed grating beam splitter via vertical coupling,” *IEEE Photonics Technol. Lett.*, vol. 23, no. 13, pp. 896–898, 2011.

[110] D. Vermeulen, P. Verheyen, G. Lepage, W. Bogaerts, P. Absil, D. Van Thourhout, and G. Roelkens, “High-efficiency fiber-to-chip grating couplers realized using an advanced CMOS-compatible silicon-on-insulator platform,” *Opt. Express*, vol. 18, no. 17, pp. 18 278–18 283, 2010.

[111] Y. Tang, Z. Wang, L. Wosinski, U. Westergren, and S. He, “Highly efficient nonuniform grating coupler for silicon-on-insulator nanophotonic circuits,” *Opt. Lett.*, vol. 35, no. 8, pp. 1290–1292, 2010.

[112] C. R. Doerr, L. Chen, Y.-K. Chen, and L. L. Buhl, “Wide bandwidth silicon nitride grating coupler,” *IEEE Photonics Technol. Lett.*, vol. 22, no. 19, pp. 1461–1463, 2010.

[113] P. J. Bock, P. Cheben, A. Delâge, J. H. Schmid, D.-X. Xu, S. Janz, and T. J. Hall, “Demultiplexer with blazed waveguide sidewall grating and sub-wavelength grating structure,” *Opt. Express*, vol. 16, no. 22, pp. 17 616–17 625, 2008.

[114] X. Chen, K. Xu, Z. Cheng, C. K. Fung, and H. K. Tsang, “Wideband subwavelength gratings for coupling between silicon-on-insulator waveguides and optical fibers,” *Opt. Lett*, vol. 37, no. 17, pp. 3483–3485, 2012.

[115] R. Waldhäusl, B. Schnabel, P. Dannberg, E.-B. Kley, A. Bräuer, and W. Karthe, “Efficient coupling into polymer waveguides by gratings,” *Appl. Opt.*, vol. 36, no. 36, pp. 9383–9390, 1997.

[116] S. Romero-García, F. Merget, F. Zhong, H. Finkelstein, and J. Witzens, “Visible wavelength silicon nitride focusing grating coupler with AlCu/TiN reflector,” *Opt. Lett.*, vol. 38, no. 14, pp. 2521–2523, 2013.

[117] Y. Li, D. Vermeulen, Y. De Koninck, G. Yurtsever, G. Roelkens, and R. Baets, “Compact grating couplers on silicon-on-insulator with reduced backreflection,” *Opt. Lett.*, vol. 37, no. 21, pp. 4356–4358, 2012.

[118] G. Roelkens, D. Van Thourhout, and R. Baets, “High efficiency silicon-on-insulator grating coupler based on a poly-silicon overlay,” *Opt. Express*, vol. 14, no. 24, pp. 11 622–11 630, 2006.

[119] P. Cheben, S. Janz, D.-X. Xu, B. Lamontagne, A. Delâge, and S. Tanev, “A broadband waveguide grating coupler with a subwavelength grating mirror,” *IEEE Photonics Technol. Lett.*, vol. 18, no. 1, pp. 13–15, 2006.

[120] R. Halir, I. Molina-Fernández, A. Ortega-Moñux, J. Wangüemert-Pérez, D.-X. Xu, P. Cheben, and S. Janz, “A design procedure for high-performance, rib-waveguide-based multimode interference couplers in silicon-on-insulator,” *J. Lightwave Technol.*, vol. 26, no. 16, pp. 2928–2936, 2008.

[121] P. Cheben, J. Schmid, A. Delâge, A. Densmore, S. Janz, B. Lamontagne, J. Lapointe, E. Post, P. Waldron, and D.-X. Xu, “A high-resolution silicon-on-insulator arrayed waveguide grating microspectrometer with sub-micrometer aperture waveguides,” *Opt. Express*, vol. 15, no. 5, pp. 2299–2306, 2007.

[122] M. Florjańczyk, P. Cheben, S. Janz, A. Scott, B. Solheim, and D.-X. Xu, "Multi-aperture planar waveguide spectrometer formed by arrayed Mach-Zehnder interferometers," *Opt. Express*, vol. 15, no. 26, pp. 18 176–18 189, 2007.

[123] K. Voigt, L. Zimmermann, G. Winzer, T. Mitze, J. Bruns, K. Petermann, B. Huttl, and C. Schubert, "Performance of 40-Gb/s DPSK demodulator in SOI-technology," *IEEE Photonics Technol. Lett.*, vol. 20, no. 8, pp. 614–616, 2008.

[124] R. Halir, A. Ortega-Moñux, I. Molina-Fernández, J. G. Wangüemert-Pérez, P. Cheben, D.-X. Xu, B. Lamontagne, and S. Janz, "Integrated optical six-port reflectometer in silicon-on-insulator," *J. Lightwave Technol.*, vol. 27, no. 23, pp. 5405–5409, 2009.

[125] R. A. Soref, J. Schmidtchen, and K. Petermann, "Large single-mode rib waveguides in GeSi-Si and Si-on-$\mathrm{SiO_2}$," *IEEE J. Sel. Top. Quantum Electron.*, vol. 27, no. 8, pp. 1971–1974, 1991.

[126] L. Zavargo-Peche, A. Ortega-Moñux, J. G. Wangüemert-Pérez, and I. Molina-Fernández, "Fourier based combined techniques to design novel sub-wavelength optical integrated devices," *Prog. Electromagn. Res.*, vol. 123, pp. 447–465, 2012.

[127] R. Halir, I. Molina-Fernández, J. G. Wangüemert-Pérez, A. Ortega-Moñux, J. de Oliva-Rubio, and P. Cheben, "Characterization of integrated photonic devices with minimum phase technique," *Opt. Express*, vol. 17, no. 10, pp. 8349–8361, 2009.

[128] S. M. Rytov, "The electromagnetic properties of finely layered medium," *Sov. Phys. JETP*, vol. 2, pp. 466–475, 1956.

[129] W. S. Zaoui, M. F. Rosa, W. Vogel, M. Berroth, J. Butschke, and F. Letzkus, "Cost-effective CMOS-compatible grating couplers with backside metal mirror and 69% coupling efficiency," *Opt. Express*, vol. 20, no. 26, pp. B238–B243, 2012.

[130] E. Ip, A. P. T. Lau, D. J. Barros, and J. M. Kahn, "Coherent detection in optical fiber systems," *Opt. Express*, vol. 16, no. 2, pp. 753–791, 2008.

[131] Optical Internetworking Forum (OIF) implementation agreement for integrated dual polarization intradyne coherent receivers. [Online]. Available: http://www.oiforum.com/public/documents/OIFDPCRX-01.0.pdf

[132] C. Doerr, L. Zhang, P. Winzer, N. Weimann, V. Houtsma, T. Hu, N. Sauer, L. Buhl, D. Neilson, S. Chandrasekhar, and Y. Chen, "Monolithic InP dual-polarization and dual-quadrature coherent receiver," *IEEE Photonics Technol. Lett..*, vol. 23, no. 11, pp. 694–696, 2011.

[133] D. Pérez-Galacho, R. Zhang, A. Ortega-Moñux, R. Halir, **C. Alonso-Ramos**, P. Runge, K. Janiak, G. Zhou, H.-G. Bach, A. G. Steffan, and I. Molina Fernández, "Integrated polarization beam splitter for 100/400 GE polarization multiplexed coherent optical communications," *J. Lightwave Technol.*, vol. 32, no. 3, pp. 361–368, 2014.

[134] C. R. Doerr, P. J. Winzer, Y.-K. Chen, S. Chandrasekhar, M. S. Rasras, L. Chen, T.-Y. Liow, K.-W. Ang, and G.-Q. Lo, “Monolithic polarization and phase diversity coherent receiver in silicon,” *J. Lightwave Technol.*, vol. 28, no. 4, pp. 520–525, 2010.

[135] D. Dai, Z. Wang, J. Peters, and J. E. Bowers, “Compact polarization beam splitter using an asymmetrical Mach–Zehnder interferometer based on silicon-on-insulator waveguides,” *IEEE Photonics Technol. Lett.*, vol. 24, no. 8, pp. 673–675, 2012.

[136] D. Pérez-Galacho, R. Halir, A. Ortega-Moñux, **C. Alonso-Ramos**, R. Zhang, P. Runge, K. Janiak, H.-G. Bach, A. Steffan, and I. Molina-Fernández, “Integrated polarization beam splitter with relaxed fabrication tolerances,” *Opt. Express*, vol. 21, no. 12, pp. 14 146–14 151, 2013.

[137] Y. Ding, L. Liu, C. Peucheret, and H. Ou, “Fabrication tolerant polarization splitter and rotator based on a tapered directional coupler,” *Opt. Express*, vol. 20, no. 18, pp. 20 021–20 027, 2012.

[138] J. J. van der Tol, M. Felicetti, and M. K. Smit, “Increasing tolerance in passive integrated optical polarization converters,” *J. Lightwave Technol.*, vol. 30, no. 17, pp. 2884–2889, 2012.

[139] J. Van der Tol, J. Pedersen, E. Metaal, F. Hakimzadeh, Y. Oei, F. Groen, and I. Moerman, “Realization of a short integrated optic passive polarization converter,” *IEEE Photonics Technol. Lett.*, vol. 7, no. 8, pp. 893–895, 1995.

[140] Y. Shani, R. Alferness, T. Koch, U. Koren, M. Oron, B. Miller, and M. Young, “Polarization rotation in asymmetric periodic loaded rib waveguides,” *Appl. Phys. Lett.*, vol. 59, no. 11, pp. 1278–1280, 1991.

[141] R. Kunkel, H.-G. Bach, D. Hoffmann, C. Weinert, I. Molina-Fernández, and R. Halir, “First monolithic InP-based 90-hybrid OEIC comprising balanced detectors for 100GE coherent frontends,” in *International Conference on Indium Phosphide & Related Materials (IPRM)*. IEEE, 2009, pp. 167–170.

[142] J. H. Schmid, M. Ibrahim, P. Cheben, J. Lapointe, S. Janz, P. Bock, A. Densmore, B. Lamontagne, R. Ma, W. Ye, and D.-X. Xu, “Temperature-independent silicon subwavelength grating waveguides,” *Opt. Lett.*, vol. 36, no. 11, pp. 2110–2112, 2011.

[143] S. J. Savory, “Digital filters for coherent optical receivers,” *Opt. Express*, vol. 16, no. 2, pp. 804–817, 2008.

[144] P. Reyes-Iglesias, A. Ortega-Moñux, and I. Molina-Fernández, “Enhanced monolithically integrated coherent 120 downconverter with high fabrication yield,” *Opt. Express*, vol. 20, no. 21, pp. 23 013–23 018, 2012.

[145] I. Fatadin, S. J. Savory, and D. Ives, “Compensation of quadrature imbalance in an optical QPSK coherent receiver,” *IEEE Photon. Technol. Lett.*, vol. 20, no. 20, pp. 1733–1735, 2008.

[146] J. Fandiño, P. Muñoz, and J. Capmany, “Manufacturing tolerance analysis of an inp, 4x4 mmi-based 90° optical hybrid for integrated coherent receivers,” in *Optical Fiber Communication Conference (OFC)*. OSA, 2013, pp. JW2A31–1–JW2A31–3.

[147] X. Zheng and A. V. Krishnamoorthy, “Si photonics technology for future optical interconnection,” in *Asia Communications and Photonics*. SPIE/OSA/IEEE, 2011, pp. 83 091V–83 091V.

[148] Y. Zhang, D. Kwong, X. Xu, A. Hosseini, S. Y. Yang, J. A. Rogers, and R. T. Chen, “On-chip intra-and inter-layer grating couplers for three-dimensional integration of silicon photonics,” *Appl. Phys. Lett.*, vol. 102, no. 21, pp. 211 109–1–211 109–4, 2013.

[149] **C. Alonso-Ramos**, F. Morichetti, S. Grillanda, A. Ortega-Moñux, I. Molina-Fernández, and A. Melloni, “Photonic integrated dual-mode filters realized with ring resonators loaded by Bragg gratings,” in *Integrated Photonics Research, Silicon and Nanophotonics (IPR)*. OSA, 2013, pp. IT5A.3–1–IT5A.3–3.

[150] **C. Alonso-Ramos**, F. Morichetti, A. Ortega-Moñux, I. Molina-Fernández, M. J. Strain, and A. Melloni, “Dual-mode coupled-resonator integrated optical filters,” *IEEE Photonics Technol. Lett.*, vol. 26, pp. 929–932, 2014.

[151] A. V. Velasco, M. Calvo, P. Cheben, A. Ortega-Moñux, J. H. Schmid, **C. Alonso-Ramos**, I. Molina-Fernández, J. Lapointe, M. Vachon, S. Janz, and D.-X. Xu, “Ultra-compact polarization mode converter implemented in a dual-trench silicon-on-insulator waveguide,” in *Conference on Lasers and Electro-Optics (CLEO)*. OSA, 2012, pp. CM4M5–1–CM4M5–3.

[152] A. Ortega-Moñux, **C. Alonso-Ramos**, A. Maese-Novo, R. Halir, L. Zavargo-Peche, D. Pérez-Galacho, I. Molina-Fernández, J. G. Wangüemert-Pérez, P. Cheben, J. H. Schmid, J. Lapointe, D.-X. Xu, and S. Janz, “An ultra-compact multimode interference coupler with a subwavelength grating slot,” *Laser & Photon. Rev.*, vol. 7, no. 2, pp. L12–L15, 2013.

[153] A. Ortega Moñux, R. Halir, A. Maese Novo, **C. Alonso-Ramos**, L. Zavargo Peche, D. Pérez Galacho, I. Molina Fernández, J. G. Wangüemert-Pérez, P. Cheben, J. H. Schmid, J. Lapointe, D.-X. Xu, and S. Janz, “Re-inventing multimode interference couplers using subwavelength gratings,” in *Conference on Laser and Electro-Optics Europe and International Quantum Electronics Conference (CLEO)*. OSA, 2013, pp. CK–9.3.

[154] R. Halir, A. Maese-Novo, A. Ortega-Moñux, I. Molina-Fernández, J. Wangüemert-Pérez, P. Cheben, D.-X. Xu, J. Schmid, and S. Janz, “Colorless directional coupler with dispersion engineered sub-wavelength structure,” *Opt. Express*, vol. 20, no. 12, pp. 13 470–13 477, 2012.

[155] A. Maese-Novo, R. Halir, S. Romero-García, D. Pérez-Galacho, L. Zavargo-Peche, A. Ortega-Monux, I. Molina-Fernández, J. Wangüemert-Pérez, and

P. Cheben, “Wavelength independent multimode interference coupler,” *Opt. Express*, vol. 21, no. 6, pp. 7033–7040, 2013.